Modeling Pore Structures and Airflow in Grain Beds using Discrete Element Method and Pore-Scale Models

by

Rong Yue

A Thesis submitted to the Faculty of Graduate Studies of

The University of Manitoba

in partial fulfillment of the requirements of the degree of

DOCTOR OF PHILOSOPHY

Department of Biosystems Engineering

University of Manitoba

Winnipeg

Abstract

The main objective of this research was to model the airflow paths through grain bulks and predict the resistance to airflow. The discrete element method (DEM) was used to simulate the pore structures of grain bulks. A commercial software package PFC^{3D} (Particle Flow Code in Three Dimension) was used to develop the DEM model. In the model, soybeans kernels were considered as spherical particles. Based on simulated positions (coordinates) and radii of individual particles, the characteristics of airflow paths (path width, tortuosity, turning angles, etc.) in the vertical and horizontal directions of the grain bed were calculated and compared. The discrete element method was also used to simulate particle packing in porous beds subjected to vertical vibration. Based on the simulated spatial arrangement of particles, the effect of vibration on critical pore structure parameters (porosity, tortuosity, pore throat width) was quantified. A pore-scale flow branching model was developed to predict the resistance to airflow through the grain bulks. Delaunay tessellation was also used to develop a pore network model to predict airflow resistance. Experiments were conducted to measure the resistance to airflow to validate the models. It was found that the discrete element models developed using PFC^{3D} was capable of predicting the pore structures of grain bulks, which provided a base for geometrically constructing airflow paths through the pore space between particles. The tortuosity for the widest and narrowest airflow paths predicted based on the discrete element model was in good agreement with the experimental data reported in the literature. Both pore-scale models (branched path and

network) proposed in this study for predicting airflow resistance (pressure drop) through grain bulks appeared promising. The predicted pressure drop by the branched path model was slightly (<12%) lower than the experimental value, but almost identical to that recommended by ASABE Standard. The predicted pressure drop by the network model was also lower than the measured value (2.20 vs. 2.44 Pa), but very close to that recommended by ASABE Standard (2.20 vs. 2.28Pa).

Acknowledgements

I would like to express my special appreciation and thanks to my advisor Dr Qiang. Zhang for his advice, continuous guidance and constant encouragement throughout my Ph.D program. I would also like to thank my committee members: Dr Douglas W. Ruth and Dr. Ramanathan Sri Ranjan for their valuable suggestions during committee meetings. I would like to thank Dr Ying. Chen for giving me access to the PFC^{3D} software.

I would like to express my special thanks to the technicians Dale Bourns, Matt McDonald, and Robert Lavallee in the Department of Biosysems Engineering for their help in my experimental design. I also wish to thank all my lab members: Dr. Chuanyun. Liu, Amy La-Guzman, Charles Chioma Nwaizu, Gajanand Saini, Zhu Gao, Desmond Essien, David Wildman, Erica Lam, Angelo De Luca, Kelvin Ngan, Kelsey Smyth and my friends Sadek Mohammad and Yixuan Chen for their technical assistance and friendship. Also the help of my roommates: Xuehua Zhang, Ru Li, and Li Ni for their encouragement and blessings in the journey.

I wish to express my deep gratitude to my parents, sister and brother and all relatives for their continuous encouragement and support. I also wish to express my special thanks to my beloved husband for his constant support, encouragement and accompany.

Finally, I want to express my gratitude to China Scholarship Council for providing this opportunity to me to study as a Ph.D. student at University of Manitoba and

financial support through my Ph.D program. Without their support, I could not have come here and finish my finish my study.

Also thanks are due to everyone not mentioned but most important not forgotten.

Table of contents

CHAPTER
Abstract I
Acknowledgements III
Table of contents V
List of Tables VII
List of Figures VIII
1. Introduction 1
2 Literature Review 4
2.1 Airflow resistance through grain bulks 4
2.1.1 Porosity 4
2.1.2 Bulk density 7
2.1.3 Moisture content 7
2.1.4 Method of filling 8
2.1.5 Airflow rate 10
2.1.6 Flow direction 10
2.1.7 Foreign materials 12
2.2 Flow through porous media 13
2.2.1 Porous media 13
2.2.2 Pore structure 14
2.2.3 Tortuosity 16
2.2.4 Discrete element modelling of porous materials 21
2.1 25
2.2 25
2.3 Modeling flow through porous media 25
2.3.1 Theoretical models for flow through porous media 26
2.3.2 Empirical models for flow resistance through grain bulks 30
2.3.3 Numerical models for flow resistance through porous media 32
2.3.4 Summary of model review 38
3 Materials and Methodology 40
3.1 DEM modelling of pore structures in grain bulks 40
3.2 Simulating grain beds subjected to vibration 44
3.3 Physical properties of grain and bin for DEM simulations 46
3.4 Simulation of airflow paths through grain bulks 48
3.4.1 Algorithm for calculating airflow paths 48
3.4.2 Predicting tortuosity of airflow paths 54
3.5 Pore-scale fluid flow models for predicting airflow resistance through grain bulks 57
3.5.1 Branched path model 57
3.5.2 Pore-scale network model 63
3.5.2.1 Simulation of grain bed 64

3.5.2.2 Delaunay tessellation 64
3.5.2.3 Pressure drop at pore level 67
3.6 Validation experiment 69
4 Results and Discussion.....72
4.1 Simulated pore structures of grain bed and airflow paths 72
4.1.1 Simulated grain beds 72
4.1.2 Simulated airflow paths.....74
4.1.3 Comparison of pore structures between the vertical and horizontal directions 82
4.1.4 Effects of vertical vibration on pore structure 84
4.1.4.1 Properties of simulated grain bed and comparison with experimental data. 84
4.1.4.2 Variation in porosity during vibration 85
4.1.4.3 Effects of vibration intensity on porosity 88
4.1.4.4 Effects of vibration on airflow path.....90
4.2 Airflow resistance 94
4.2.1 Experimental results.....94
4.2.2 Prediction by branched path model.....95
4.2.3 Prediction by network model 101
5 Conclusions.....102
5.1 Discrete element modeling of pore structure and airflow path 102
5.2. Airflow resistance modelling 103
5.3. Effect of vibration 103
6 Recommendations.....104
References.....106
Appendix A. PFC^{3D} Code for Simulating Rectangular Grain Bed.....125
Appendix B. PFC^{3D} Code for Simulating Cylindrical Grain Bed 128
Appendix C. PFC^{3D} Code for Simulating Vibration of Cylindrical Grain Bed.....133
Appendix D. Matlab Algorithm For Calculating the Widest Airflow Path and Tortuosities.....142
Appendix E. Matlab Algorithm for Calculating the Narrowest Airflow Path and Tortuosities.....152
Appendix F. Matlab Algorithm for Predicting Resistance to Airflow by Branched Model 162
Appendix G. Matlab Algorithm for Predicting Resistance To Airflow by Network Model.....166

List of Tables

Table 2.1 The ratio of resistance to airflow in the horizontal direction to vertical to vertical direction for different grains……..…….. 11

Table 3.1 PFC simulation parameters reported by Liu et al. (2008a)…….. 48

Table 4.1 Summary of calculated flow path parameters of three widest and three narrowest airflow paths…….. 75

Table 4.2. Simulated tortuosities for three widest and three narrowest airflow paths before and after smoothing…….. 82

Table 4.3 Summary of calculated flow path parameters for three widest airflow paths in the vertical direction and in the horizontal direction…… 83

Table 4.4a. Predicted pressure drops for the three widest airflow paths through the grain bed based on different LFPW as well as different multiplier functions…… 98

Table 4.4b. Predicted pressure drops for the three narrowest airflow paths through the grain bed based on different LFPW as well as different multiplier functions.……..... 99

Table 4.5. Comparison of simulation results of pressure drop for airflow through the grain bed with experimental results and the literature data……. 100

List of Figures

Figure 2.1. Illustration of a tortuous airflow path…… 17

Figure 2.2. Illustration of the Representative Unit Cell (RUC) model……. 35

Figure 3.1. Small-scale grain bins filled with soybeans (a) rectangular bin usedbyNwaizuand Zhang (2015), (b) cylindrical bin subjected to vibration, used by Liu et al. (2012)……... 41

Figure 3.2. A Schematic of simulated bin showing the locations (B1-B5) where local porosity was calculated……. 46

Figure 3.3. A tetrahedron unit representing grain mass at a point in the grain bed……. 49

Figure 3.4. Pore throat sizes for airflow paths in a tetrahedron unit…… 51

Figure 3.5. Illustration of the cross-sectional area for airflow through a triangle. 52

Figure 3.6. Illustration of the step-increment procedure to construct a global airflow path…….……. . 53

Figure 3.7. An example which requires reselecting the exit triangle……..….. 54

Figure 3.8. An example of pore space larger than a particle, resulting in an unstable tetrahedron…….. 54

Figure 3.9. Schematics of local airflow paths……..…….. 55

Figure 3.10. Schematic representation of smoothing the airflow path by replacing the sharp turning angle with an arc (Sobieski et al. 2012)……..... 56

Figure 3.11. The definition of branched flow model for airflow through each tetrahedron unit…….…..… 58

Figure 3.12. Illustration of the total pressure drop calculation……..... 59

Figure 3.13. Illustration of three cases of cross sectional area……. 63

Figure 3.14. A Delaunay tetrahedron representing grain mass in the bin.…… 65

Figure 3.15. Illustration of the pore and pore throat of a Delaunay tessellation…. 65

Figure 3.16. The process of Delaunay tessellation……..… 66

Figure 3.17. Four types of throat geometries on a triangle face…… 68

Figure 3.18. The experiment apparatus for measuring the pressure drops of airflow…….…… 71

Figure 3.19. Schematics of the test grain bin for airflow resistance measurement. 71

Figure 4.1. Simulated grain beds by PFC^{3D} DEM model. (a) rectangular bin, (b) cylindrical bin……..……. 73

Figure 4.2. The frequency distribution of particle size……. 73

Figure 4.3. Distribution of coordination number in the simulated grain bed for rectangular bed……. 74

Figure 4.4 Simulated airflow paths, as represented by the associated tetrahedron units. (a) three widest paths, and (b) three narrowest paths…….. 76

Figure 4.5. Simulated airflow paths in two-dimension. (a) three widest paths, and three narrowest paths……..... 77

Figure 4.6. The frequency distribution of local turning angles for (a) three widest paths and (b) three narrowest paths……. 79

Figure 4.7. The variation of the path width in the vertical direction for (a) three widest paths and (b) three narrowest paths…… ……..……... 80

Figure 4.8. Distribution of airflow path width for (a) three widest paths and (b) three narrowest paths…… 81

Figure 4.9. Three widest airflow paths in the vertical direction and three widest airflow……... 83

Figure 4.10. Distribution of airflow path width for three widest paths in the horizontal direction……...……. 84

Figure 4.11. Simulated local porosity during vibration at locations B1(0.06, 0) and B2(0.06, 0.119), and the average porosity of all five locations for vibration intensity of 1.8g (15 Hz frequency and 2 mm amplitude)……...……. 87

Figure 4.12. Relative change in area of triangle formed by three particles during vibration at 25 Hz frequency and 0.45 mm amplitude (based on data reported by Liu 2008)……. 87

Figure 4.13. Simulated average local porosity during vibration at intensities of 0.45g, 1.81g, and 3.62g…….……..... 90

Figure 4.14. Effect of vibration intensity on porosity…… 90

Figure 4.15. Typical simulated airflow paths (reduced to 2D) for different vibration intensities…..……. 91

Figure 4.16. Variation of simulated tortuosity with vibration intensities (each data point represents the average of three simulated paths and the error bar indicates the minimum and maximum values)……. 92

Figure 4.17. Pore throat width of local flow paths from the bin bottom (tetrahedron no. 1) to the top under different vibration condition……..…... 93

Figure 4.18. Distribution of pore throat width under different vibration intensities. …… 94

Figure 4.19. Pressure drop of airflow through the grain bed at different airflow rates (three replicates)……. …….. 95

1. Introduction

Drying and aeration are commonly used in grain storage to prevent spoilage of stored grains. To dry or aerate grain, air (heated for drying) is forced through the grain bed by fans to remove grain moisture or to lower grain temperature, thus preventing the growth of bacteria and fungi. The fans must provide enough pressure to overcome the resistance of the grain bed to airflow. Therefore, airflow resistance is an important consideration in the design of grain drying and aeration systems because it dictates the power requirement of the equipment, as well as the uniformity of drying and cooling.

Airflow resistance of agricultural products has been studied since early 1930s (Stirniman 1931), but most studies are experimental in nature, focusing on developing empirical equations to represent the airflow resistance characteristics of various agricultural products (Shedd 1953; Hukill and Ives 1955; Ergun 1952). Specifically, the pressure drop along a column of the agricultural product at different airflow velocities was measured and then the experimental data was fitted to some equations or models. The ASABE Standards D272.3 (ASABE 2011) gives a large collection of the data for estimating the resistance to airflow for various grains, seeds and other agricultural products in the form of curves relating the superficial air velocity ($m^3\ s^{-1}\ m^{-2}$) to the pressure drop per unit depth (Pa m^{-1}).

Airflow resistance through a grain bed is affected by many factors, including airflow rate, grain depth, shape of storage bin, shape and size of grain kernels, bulk density, grain moisture content, methods of filling, foreign materials, and direction of airflow (Calderwod 1973; Jayas et al. 1987a; Siebenmorgen and Jindal; 1987; Farmer et al. 1981; Haque et al. 1982; Kumar &

Muir, 1986; Gunasekaran and Jackson 1988; Sokhansanj et al 1988; Jayas & Sokhansanj 1989; Sokhansanj et al. 1993; Dairo and Ajibola 1994; Madamba et al. 1994; Rapusas et al. 1995; Al-yahya and Moghazi 1998; Pagano et al. 1998; Rajabipour et al. 2001; Chung et al. 2001; Nalladurai et al. 2002; Nimkar and Chattopadhyay 2002; Sacilik 2004; Agullo and Marenya 2005; Molenda et al. 2005; Sorour 2006; Kashaninejad and Tabil 2008; Shahbazi 2011; Amanlou and Zomorodian 2011). It is extremely difficult to include all these factors in empirical models for predicting airflow resistance of grain. On the other hand, the complexity and variability of pore structures make it very challenging to develop mechanistic models for airflow through grain bulks. Researchers have attempted to develop flow models at the pore scale for porous media. For predicting airflow resistance through a packed bed, Ergun's equation is most widely used, although it assumes a straight tube geometry of the pore space and does not take into account interconnectivity and tortuosity (Yu 2008). Du Plesis and Woudberg (2008) proposed a concept of representative unit cells (RUC) to simplify the pore structure of porous materials and studied the resistance to airflow through the RUC. The approach was based on the original idea of Du Plessis and Masliyah (1991) for flow through isotropic porous media. The RUC model was based on the mean geometrical properties of an idealized microstructure, and a set of momentum transport equations were then applied to a porous medium over the entire porosity ranging from zero through unity. Wu et al. (2008) developed a flow resistance model for granular media, in which resistance was expressed as a function of tortuosity, porosity, ratio of pore diameter to throat diameter, diameter of particles, and fluid properties. However, a critical assumption (simplification) made in this model was that pore and particles were uniformly distributed and the porous media was isotropic and

homogenous.

In studies of porous media flow, the attention has been mostly focused on the flow behavior (velocity, pressure, etc.), while pore structures are often idealized as flow channels of simple geometry. There is a lack of research effort in linking the characteristics of pore structures (sizes, shapes, locations, orientations, and connectivity) to airflow resistance. This research attempted to characterize the pore structures in porous materials by using the discrete element method (DEM) and integrate the knowledge of pore structures with fluid flow models to predict airflow resistance through (bulk) grains. The specific objectives of this thesis research were:

1. To develop a discrete element model to simulate pore structures of grain bulks
2. To develop a pore-scale fluid flow model and integrate it with the DEM pore-structure model to predict the resistance to airflow through grain bulks
    a) Quantify paths for airflow through the grain bulks based on DEM simulations
    b) Develop a pore-scale model to predict the airflow resistance along individual airflow paths
3. To develop a pore network model based on DEM simulated pore structures to predict the resistance to airflow through grain bulks
4. To conduct experiments to validate airflow resistance models

2 Literature Review

2.1 Airflow resistance through grain bulks

When air is forced to flow through grain bulks (porous media) there is pressure drop that occurs as a result of energy losses caused by friction and turbulence (Kaleta and Górnicki 2011). This pressure drop is termed as resistance to airflow, commonly defined as the pressure drop per unit bed depth (Gornicki and Kaleta 2015). The airflow resistance of agricultural products has been studied since 1930s. Most of studies involved the measurement of pressure drop along a column of the material being tested at different flow rates, and then experimental data was fitted to some empirical equations or models (Sokhansanj et al. 1990; Pagano et al. 1998; Rajabipour et al. 2001; Nalladurai et al. 2002; Ray et al. 2004; Sacilik 2004; Agullo and Marenya 2005; Jekayinfa 2006; Lukaszuk et al. 2008; Kashaninejad and Tabil 2009; Amanlou and Zomorodian 2011; Shahbazi 2011; Kenghe et al. 2012). Airflow resistance in grain bulks is affected by many factors, including porosity, airflow rate, bed depth, bulk density, moisture content, shape and size of grain kernels, foreign materials, filling methods, and direction of airflow (Sokhansanj et al. 1990; Pagano et al. 1998; Chung et al. 2001; Rajabipour et al. 2001; Nalladurai et al. 2002; Ray et al. 2004; Sacilik 2004; Agullo and Marenya 2005; Jekayinfa 2006; Lukaszuk et al. 2008; Kashaninejad and Tabil 2009; Amanlou and Zomorodian 2011; Shahbazi 2011; Kenghe et al. 2012).

2.1.1 Porosity

One of the most important characteristics of a porous medium is porosity, which has a

significant effect on flow resistance. Porosity is defined as the volume of voids over the total volume. The value is between 0 and 1 or as a percentage between 0 and 100%. The porosity of porous materials may be determined from bulk and particle densities using the following equation (Mohsenin 1986):

$$\emptyset = \frac{\rho_p - \rho_b}{\rho_p} \times 100\% \qquad (2.1)$$

where

$\emptyset$ = porosity

ρ_p = particle density (kg m^{-3})

ρ_b = bulk density (kg m^{-3})

The extreme values of the porosity for ideal porous materials consisting of monosized spheres range from 0.26 (regular hexagonal packing) to 0.48 (regular cubic packing). The porosity usually lies between 0.26 and 0.48 for materials consisting of irregular particles in random packing arrangements, which is higher when the particles are extremely irregular and small (Woodcock and Mason 1987). It is more difficult for gas or liquid to pass through materials with low porosity than with high porosity because of the smaller pores making the material less permeated (Anandh and Baskar 2015). When fluids flow through porous media, only the interconnected pores form flow paths (Koponen et al. 1997). The concept of effective porosity has been used by some researchers in studying flow through porous media, which is defined as the ratio of the interconnected (effective) pores to the total volume of the porous material. The non-conducting pore space of a porous media includes the occluded pores and the dead-end pores. The occluded pores are not connected to the main void space, while dead-end pores belong to the interconnected pores but contribute very little to the flow (Jacob 1988).

Porosity of grain bulks is affected by several factors, including moisture content, bulk density, amount of fine material, method of harvesting and drying. Thompson and Isaacs (1967) found that the porosity of shelled corn was affected by varietal differences as much as 8%. Specifically, the porosity decreased by over 8% with the reduction of moisture content from 30.8% to 9.0% when corn was dried with unheated air, and increased by approximately 23% by grinding the material. High temperature drying increased the void space of wet corn. Within the range from 450.5 to 836.7 kg m^{-3} (35 to 65 lb bu^{-1}), the bulk density and void space was found to follow a linear relationship. Chung and Converse (1971) also found that porosity decreased linearly with increasing bulk density for wheat and corn.

Molenda et al. (2005) determined porosity for white winter wheat, red winter wheat, corn and soybeans at three moisture levels using sprinkle and funnel filling methods. The variation in porosity due to moisture content was found not uniform and depended on the grain type (Molenda et al. 2005). Specifically, the porosity was higher at higher moisture content for white wheat, red wheat, and corn but lower at higher moisture content for soybeans. Coskun et al. (2006) compared the porosities of rewetted sweet corn at different moistures in the range from 11.54% to 19.74% and found that the porosity changed from 57.48% to 61.30%. Shahbazi (2011) found similar results showing that porosity of chickpea seeds increased with increase in the moisture content Marousis and Saravacos (2006) studied density and porosity in drying starch materials and found the changes in porosity could be related to variations of the effective moisture and thermal diffusivities of starch materials..

2.1.2 **Bulk density**

Considerable research has been done on the effect of bulk density on airflow resistance. Stirmiman et al. (1931) tested the resistance to airflow through rough rice in a deep bin and found that the airflow rate per unit cross-sectional area of bin decreases linearly with the depth of rough rice at given static pressures. Henderson (1943) noticed an increase in airflow resistance from 1.0 to1.5 kPa m^{-1} resulting from a bulk density increase from 773 to 830 kg m^{-3} when the grain was filled from different heights. Calderwod (1973) found that the change in resistance to airflow through rice mainly attributed to packing (density increase). Similar results were observed by Husain and Ojha (1969) and Agrawal and Chaud (1974), who reported that rice bed depth had an effect on airflow resistance. Siebenmorgen and Jindal (1987) measured the airflow resistance of long-grain rough rice at velocities in the range from 0.013 to 0.387 m s^{-1} for bulk densities in the range from 480 to 604 kg m^{-3} and found the airflow resistance increased with the increase in bulk density. Bern and Charity (1975) found that the measured pressure drop was greater for corn columns of greater bulk density. Kashaninejad and Tabil (2009) reported that the change in pressure drop was related to the change in bulk density of pistachio nuts when filled by different filling methods. The variation in bulk density was achieved by the difference in bed depth and filling method due to the difference in compaction from the grain load (Grundas et al. 1978; Bakker-Arkema et al. 1969).

2.1.3 **Moisture content**

During storage, handling, and processing (e.g., drying), grain moisture often changes, which in turn may lead to changes in airflow resistance. The airflow resistance of rice, canola,

sorghum, laird lentils, alfalfa pellets, barley, chickpea seeds, sorghum and rough rice, paddy and sunflower was reported to decrease with increasing moisture content by some researchers (Calderwod 1973; Jayas et al. 1987a; Siebenmorgen and Jindal 1987; Gunasekaran and Jackson 1988; Sokhansanj et al 1988; Sokhansanj et al. 1993; Al-yahya and Moghazi 1998; Shahbazi 2011; Chung et al. 2001; Nalladurai et al. 2002; Sorour 2006). The decrease in pressure drop might be due to the fact that at higher grain moisture contents, the grain bulk could not be densely packed, resulting in higher porosity. However, other researchers (Rapusas et al. 1995; Madamba et al. 1994; Rajabipour et al. 2001; Kashaninejad and Tabil 2008; Amanlou and Zomordian 2011) reported that the resistance to airflow through sliced onions, garlic slices, walnuts, pistachio nuts, and green figs increased with increasing moisture content. The inconsistency in observations of the resistance to airflow through grain bulks caused by moisture content could be explained by the different effects of moisture content on the bulk density of different grains. It was reported that the bulk density of some grains (rough rice, short rice) increased with increasing moisture content, whereas the opposite trend was observed for some other grains (canola, fababeans, flaxseed, gram, lentils, soybean) (Chakraverty et al. 2003).

2.1.4 **Method of filling**

Different methods of filling storage bins with grain were found to change orientation of grain kernels, and produce different densities and porosities of grain in storage bins, thus resulting in variable airflow resistances (Lukaszuk et al. 2008; Kumar and Muir 1986; Shahbazi 2011; Bern and Charity 1975; Dairo and Ajibola 1994; Farmer et al. 1981). Shedd's

(1943) proposed a method of creating loose-fill and dense-fill grain beds. Specifically, the grain was poured into a funnel which was held just above the seed surface by gradually raising the funnel as the filling progressed and then the bulk density was slowly increased to the desired level by tapping the column with a rubber hammer about 30 times and 60 times for medium and dense bulk densities. These methods of loose fill and dense fill were used by several other researchers to study the effect of filling methods on the resistance to flow through sesame, green gram, and poppy seeds, and they found lower resistance to airflow in loose fill than dense fill (Dairo and Ajibola 1994; Nimkar and Chattopadhyay 2002; Sacilik 2004). Shedd (1951) found that a bin of clean shelled corn had a 20% increase in airflow resistance for packed fill over loose fill. Pagano et al. (1998) measured the resistance to airflow through clean grain under loose fill from a falling height near zero and dense fill from a maximum height of 1.6 m. The resistance to airflow in dense fill was found to be 1.3 to 1.5 times that in loose fill. Agullo and Marenya (2005) used a loose fill method and dense fill method (samples were sprinkled into the chamber from a height of 300mm), as described by Jayas et al. (1987), to fill a test column with the parchment coffee. The pressure drop per unit depth at various levels of moisture content from 12.7 to 36.7% (w.b)) and at airflow rates between 0.126 to 0.720 $m^{-3}s^{-1}m^{-2}$ for loose and dense filling of the test column were measured and the pressure drop for dense fill was observed 15% to 70% higher than that for loose fill. Kashaninejad and Tabil (2009) studied the effect of filling methods on the pressure drop of bulk pistachio nuts. In their research, pistachio nuts were discharged into the test chamber with a zero drop height to form a loose fill and from a height of 50 cm to form a dense fill. The pressure drop increased 97% in the dense fill compared with loose fill. Changes in flow resistance when different filling

methods were used was attributed to porosity (bulk density) differences. In addition, the orientations of grain kernels when different filling methods were used might also contribute to change in flow resistance (Bern and Charity 1975; Dairo and Ajibola 1994; Farmer et al. 1981; Jayas et al. 1987).

2.1.5 **Airflow rate**

Increases in pressure drop with increasing airflow rate have been observed and reported by Farmer et al. (1981) for blue stem grass, Haque et al. (1982) for maize, Madamba et al. (1993) for garlic slices, Dairo and Ajibola (1994) for sesame seeds, Rajabipour et al. (2001) for pistachio nuts, Shahbazi (2011) for chickpea seeds, and Agullo and Marenya (2005) for parchment Arabica coffee. Higher pressure drop with increasing airflow rate can be attributed to the increased kinetic dissipation of flowing air as air velocity increases. It has been generally observed that airflow resistance increased more rapidly with the increase in airflow rate than with the increase in bed depth for Canola (Jayas et al. 1987a), sorghum (Gunasekaran and Jackson 1988), sesame seeds (Dairo and Ajibola 1994), flax seeds (Pagano et al. 1998), green gram (Nimkar and Chattopadhyay 2002), poppy seeds (Sacilik 2004), pistachio nuts (Rajabipour et al. 2001; Kashaninejad and Tabil 2008), and figs (Amanlou and Zomorodian 2011).

2.1.6 **Flow direction**

Lower resistance to airflow in the horizontal direction (than the vertical direction) has been reported for many grains (Kumar & Muir, 1986; Jayas et al. 1987b; Sokhansanj et al.1988;

Kay et al. 1989; Nalladurai et al. 2002). The ratio of resistance in the horizontal to vertical direction for the paddy, raw rice, parboiled rice, wheat, barley, canola, lentils at certain flow rate (range) is summarized in Table. 2.1 (Kumar & Muir, 1986; Jayas et al. 1987b; Sokhansanj et al.1988; Nalladurai et al 2002). From Table. 2.1, it can be seen that the ratio of airflow resistance in the horizontal to vertical direction varies for different grain bulks, which could be explained by the variation in grain kernels with different shapes and sizes. The airflow resistance in horizontal direction was found approximately half of that in the vertical direction for 10 types of seeds at the airflow velocity of 0.2 m s^{-1} (Hood and Thorp 1992). ASABE Standard D272.3 (ASABE, 2011) recommends use the airflow resistance in the horizontal direction to be 60% to 70% of that in the vertical direction for non-spherical shaped seeds (wheat, barley, flaxseeds, etc.). Shedd (1953) argued that the difference in flow resistance between the horizontal and vertical directions was nonexistent for spherical seeds (tara peas, canola).

Table 2.1 The ratio of resistance to airflow in the horizontal direction to vertical to vertical direction for different grains

Grains	Airflow rate (m^3 s^{-1} m^{-2})	The ratio of horizontal to vertical pressure drop
Paddy	0.01-0.1	0.31
Raw rice	0.01-0.1	0.19
Parboiled rice	0.01-0.1	0.23
Wheat	0.077	0.63
Barley	0.077	0.47
Canola	0.0158-0.1709	0.6
Laird lentil	0.0019-0.192	0.52

The lower resistance to airflow in the horizontal direction was considered to be attributed to the kernel orientation (Kumar & Muir, 1986). Filling grains into bins by gravity (free fall)

may cause most grain kernels lie with the major (long) axis in the horizontal direction (the most stable position for a gain kernel), resulting in more connected pores in the horizontal direction, thus lower airflow resistance. Neethirajan et al. (2006) used the X-ray computed tomography to reconstruct the internal structures of bulk grains and observed the number of air paths along the horizontal direction for wheat, barley and flax seed, were 92%, 145% and 187% more than along the vertical direction, while there was no significant difference in the distribution of air path areas between the horizontal and vertical directions. Air path areas and air path lengths along the horizontal direction were 100% higher than those along the vertical direction for nonspherical grain bulks (wheat, barley and flax seed) and only 30% for spherical kernels (pea and mustard), which explains the higher airflow resistance for oblong kernels in the vertical direction of the grain bulk.

2.1.7 **Foreign materials**

Bulk grains normally contain various foreign materials, such as fine materials (dust, broken kernels, etc.) and chaff. The level of fines in grain significantly influenced the pressure drop (Grama et al., 1984; Giner and Denisienia 1996). Pagano (1998) reported that the fine materials caused higher pressure drop, while chaff offered less resistance to airflow in flax. The pressure drop increased with an increase in the fraction of fines in paddy and its byproducts (Nalladurai et al. 2002). Similar results were observed in shelled maize (Haque et al., 1978), long-grain rough rice (Siebenmorgen and Jindal 1987), canola (Jayas & Sokhansanj, 1989), and lentils (Sokhansanj et al., 1988). The increase in airflow resistance due to addition of fine materials became greater as the size of the fines decreased (Grama et al. 1984). However,

Chung et al. (2001) found the static pressure drop for sorghum increased with increasing fine materials but decreased as fine materials increased for rough rice, which was explained by the large size of the fine material compared to grain sorghum. Shedd (1953) concluded that the static pressure drop had a positive relation with the fine material that was smaller than the grain but negative relation with the fine material that was larger than the grain. Because more fine materials that was smaller than the grain contributes to the reduction in porosity, resulting in the increase of static pressure drop.

2.2 Flow through porous media

Movement of fluid through a porous medium is affected by the characteristics (pore structure, tortuosity, etc.) of the porous media. In this section, the studies of characteristics of porous media are reviewed.

2.2.1 Porous media

A porous medium (material) is described as a material containing pores (or voids). The skeletal portion of the material is called the “matrix” or “frame”, which is usually a solid. The pores (voids) are typically filled with a fluid (gas or liquid). However, not all materials containing pores can be defined as porous media. Bear et al. (1968) defined some features that a porous medium should have: (1) a portion of a space occupied by a heterogeneous or multiphase matter, (2) the solid phase should be distributed throughout the porous medium within the domain occupied by a porous medium; solid must be present inside each

representative elementary volume; and (3) at least some of the pores comprising of the void space should be interconnected. Numerous porous media exist in our world, including nature substances like bulk solids, rocks, soil, biological tissues (e.g., bones and wool), and man-made materials like cements, ceramic and fibrous aggregates.

2.2.2 **Pore structure**

In general, porous media has randomly distributed pore sizes, shapes, and topology, which results in the complexity and irregularity of pore structure. The complexity and irregularity of pore structures make flow through porous media inherently complex and variable. As a practical example, it has been observed by many researchers that airflow resistance of grain bulks in the horizontal direction is lower than that in the vertical direction (Kay et al., 1989; Neethirajan 2006). The orientation of particles and the differential void space distribution in the two directions might have contributed to the difference in airflow resistance between the two directions (Neethirajan 2006).

Investigating the pore structure (pore size, pore shape pore surface area and pore volume) is very important to understand the interconnectivity of pores and resistance to airflow through porous media. A number of 2D and 3D models have been developed to describe the pore structure of porous media. Yu et al. (2004) and Yun et al. (2005) used a 2D rectangular representative unit cell to simplify the pore space and simulated the streamlines of airflow paths in porous media with cubic and spherical particles. Later, Yun et al. (2010) proposed a 3D geometry model to stand for the pore space and studied the tortuosity of streamlines in porous media with randomly placed cylindrical particles. Xiao et al. (2008) integrated the

microstructure of porous media into a 2D fractal pore network model to simulate the drying process of potato slices by the pore network approach. In their model the porous medium was simplified as cylindrical pipes. The model was used to predict porous media properties such as permeability and the Forchheimer coefficient. Neethirajan et al (2008) constructed 3D models of wheat and pea bulks using X-ray CT images to characterize the specific surface area, tortuosity, pore throat size, and nodal pore volume distribution for wheat and pea. They found that the spatial distributions for throat size and nodal pore size were significantly different between wheat and pea bulks. Specifically, larger size pores and pore throat in the pea bulk explained why resistance to airflow through pea was less than that through wheat. Huang et al. (2013) constructed a 3D pore network to reflect the pore structure of bulk grains. The model was a stochastic algorithm based on the concept of the maximal balls method. The model simulated that the porosity decreased with the grain depth, which was in agreement with the experimental results, and the average radii of pores and throats also decreased with the grain depth, while the number of pores and throats slightly increased.

One of the challenges in dealing with pore structures of porous beds is the variability caused by such mechanical disturbances as vibration. When a porous bed consisting of randomly packed particles is vibrated, the pore structure is altered due to re-arrangement of particles. The mechanisms by which the pore structure is affected by vibration are extremely complex. An et al. (2009) conducted experiments to study the effect of vibration on packing density and observed that there existed optimum values of vibration frequency and amplitude to achieve the maximum packing density. Frequency and amplitude should be considered separately in terms of their effect on packing density. Liu et al (2010) used a high speed camera

to study the behavior of particles in a bin subjected to vertical vibration. They reported that all particles in a porous bed vibrated as a whole when the bed was subjected to low intensity vibration, whereas individual particles vibrated in their own modes when subjected to high intensity vibration. Charles Nwaizu (2013) studied the effect of the vibration on the pore space and the internal pore connectivity of soybean grain using image processing and found that the pore space and pore connectivity reduced significantly after vibration. The difference of elongated pores in the horizontal direction and in the vertical direction was also reduced after vibration, which means the difference in airflow resistance between horizontal and vertical directions might lessened after vibration.

The effect of vibration on pore structure is complex. Most studies on the vibration of porous beds have been focused on particle packing, and few have explored how changes in particle packing caused by vibration would impact such properties as porosity and tortuosity which are related to flow through the porous bed. Traditionally, the studies of particle packing (pore structures) are pursued in the realm of particulate mechanics, while flow through porous media has established itself as a sub-discipline in fluid mechanics.

2.2.3 **Tortuosity**

Tortuosity (τ) reflects the connectivity of pore structure. It is discussed in the book of Bear (1988) that there are two definitions of tortuosity commonly used in the research community, specifically, $(L_e\ L_0^{-1})^2$ and $L_e\ L_0^{-1}$, where L_e is the actual length of flow path and L_0 is the straight length or thickness along the macroscopic pressure gradient (Fig. 2.1). The definition $L_e\ L_0^{-1}$ is appropriate when tortuosity is treated as a pure geometric variable to define the

difference between the length of flow path and the bed depth, while $(L_e L_0^{-1})^2$ is used when both flow length and the airflow velocity are considered.

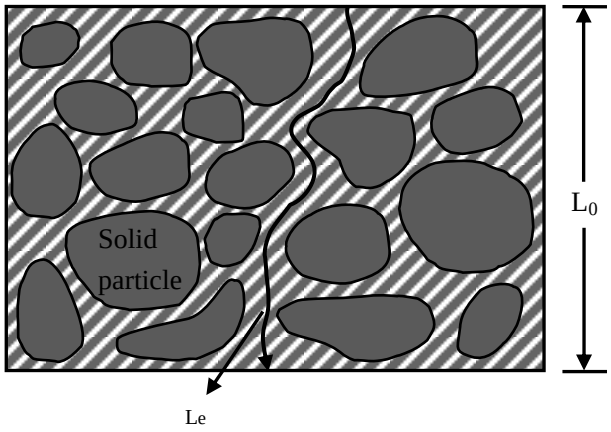

Fig. 2.1 Illustration of a tortuous airflow path

Various methods have been developed to estimate tortuosity. Based on the background concepts behind the approaches, Saomoto and Katagiri (2014) summarized those methods as: geometric models, hydraulic models, electric models and diffusive models. In terms of the methodology used in the determination, those approaches include experimental, empirical and theoretical methods (Sun et al. 2013). Different experimental methods were widely used to measure tortuosity. One of the popular experimental methods is to determine the tortuosity through the process of diffusion of fluid in porous media. This method is based on the physical principle that the diffusion of fluid through a porous medium is affected by the microscopic channel structure of the porous medium, especially at a low flow rate. Those adjustable parameters vary significantly depending on the materials used and pore structures. The other method is to measure the formation factor, which is obtained by resistivity measurements, but the experiment requires specialized equipments. Another popular experimental method is ultrasonic method, which is usually used to measure the macroscopic parameters of air

saturated porous media, such as plastic foams, the porous media saturated with a liquid like bone tissue.

Empirical equations for determining the tortuosity of flow through porous media have been developed by correlating the experimental data to one or more empirical constants. Comiti and Renaud (1989) developed an empirical equation for tortuosity through a bed of parallelepipedal particles. Three types of square-based particles of different height-to-side ratios (0.102, 0.209 and 0.440) were used in the experiments. The pressure drop was measured as a function of superficial velocity U_0 to be compared with the results calculated by Eq. 2.2:

$$\frac{\Delta P}{HU_0} = MU_0 + N \tag{2.2}$$

where

H = bed height

M and N = slope and intercept respectively of the plot of $\frac{\Delta P}{HU_0}$ versus U_0

The tortuosity was then calculated by Eq. 2.3:

$$\tau = \left[\frac{M^2}{N}\frac{2\gamma\eta\emptyset^3}{(0.0968\rho)^2}\right]^{1/4} \tag{2.3}$$

where

γ = shape factor, which was assumed to be 1 for cylindrical pores

η = dynamic viscosity of the fluid (Pa s)

ρ = density of the fluid (kg m^{-3})

$\emptyset$ = porosity of the packed bed

By fitting the experimental data, they also developed a simple equation (Eq. 2.4) to correlate tortuosity to porosity:

$$\tau = 1 + C \ln (1/\emptyset) \tag{2.4}$$

where

C = empirical constant (0.41 for spherical particles and 0.63 for cubic particles)

However, the experimental method used by Comiti and Renaud (1989) took a long time and required special equipment to measure the parameters (pore size, pore volume, porosity, conductivity, etc.) in the equations.

Westhuizen and Pless (1994) developed a model to determine the tortuosity based on the ratio of the fluid volume enclosed by a unit cell to the minimum pore cross-sectional flow area in the unit cell:

$$\tau = 1 + \sqrt{1 - \emptyset} \tag{2.5}$$

This model only works for flow through a medium of uniformly distributed square particles without overlapping. In addition, it was found that this equation underestimates the tortuosity at low porosity compared to the experimental results.

Koponen et al. (1996) derived a correlation between the average tortuosity of the flow paths and the porosity of a 2D porous medium consisted of randomly placed rectangles of equal size and with unrestricted overlap by using the Lattice Gas Automata (LGA) method, and derived equation had the following format for a porosity range from 0.5 to 1.0:

$$\tau = p(1 - \emptyset) + 1 \tag{2.6}$$

where

p = empirical constant

While Eq. 2.6 was found to be not consistent with the results obtained for the porosity range from 0.4 to 0.5, and a second equation was proposed to replace Eq. 2.7 for porosity range from 0.4 to 0.5: (Koponen et al. 1997).

$$\tau = p\frac{(1-\phi)}{(\phi-\phi_c)^m} + 1 \tag{2.7}$$

where

p and m = empirical constants

$\emptyset_c$ = percolation threshold (0.33)

The impact of the finite element size and the effect of the space discretization were not taken into account in this model.

Yu et al. (2004) developed a simple geometric model to determine the tortuosity in a porous media made of square particles. Two configurations were considered: one was cubic particles arranged in triangles without overlapping and the other with unrestrictedly overlapped. The overall tortuosity was obtained by averaging the tortuosities of the two configurations:

$$\tau = \frac{1}{2}\left[1 + \frac{1}{2}\sqrt{1-\emptyset} + \sqrt{1-\emptyset}\,\frac{\sqrt{\left(\frac{1}{\sqrt{1-\emptyset}}-1\right)^2+\frac{1}{4}}}{1-\sqrt{1-\emptyset}}\right] \quad (2.8)$$

Eq. 2.8 has been shown to be in good agreement with the Eq. 2.4 when $\emptyset$ >0.35 for flow through porous media with cubic particles but overestimates the tortuosity for flow through spherical particles by 16% at 0.40 porosity and by 9% at porosity 0.60 compared to the result calculated from Eq. 2.4 with c=0.41 (Yu 2008). In addition, the tortuosity calculated by Eq. 2.8 is only a function of porosity. However, in reality, tortuosity may also be related to the shape and size of particles (Commiti and Renaud 1989; Alam et al. 2006).

Yun et al. (2005) and Yun et al. (2010) developed similar geometrical models to estimate the tortuosity of flow through the packed beds with spherical and cylindrical particles. The advantage of such models was that they did not involve any empirical factors. However, those models were 2D and based on idealized pore structures. In reality, the pore structure of porous beds is very complicated because of the random arrangement of particles with irregular shapes

and sizes.

Lattice Boltzmann method was also used to solve the flow equations to identify the flow streamlines and determine the tortuosity of flow (Matyka et al. 2008). Pisani (2011) simulated a diffusion process through a numerical model to express the relationship between tortuosity and porosity using a single parameter (the shape factor). The procedure was simpler than previous ones. Ahmadi (2011) applied volume averaging method to determine the tortuosity of momo-sized spherical arrays. Sobieski et al. (2012) developed a numerical algorithm to calculate the tortuosity for the shortest airflow paths through the grain bed based on discrete element simulations. An airflow path was determined by a series of tetrahedron units, each consisting of four particles. The tortuosity calculated by the numerical method proposed by Sobieski et al. (2012) was very close to the value estimated form the CT image reported by Neethirajan (2006). Sun et al. (2013) determined the effective diffusion coefficient and tortuosity of a 2D porous medium using homogenization and REV with circular particles. Those theoretical models simulated the porous media which eliminated the work of experiments and fitting data. However, complicated technology, related concepts and mathematical analyses are required.

2.2.4 **Discrete element modelling of porous materials**

The difficulty in modeling flow through grain bulks at the pore scale is the characterization of the pore structure (sizes, locations, and orientations of pores and their connectivity). The discrete element method (DEM) has been shown to have the potential of predicting pore structures of porous media. The DEM was originally proposed by Cundall and

Strack (1971) to solve problems in rock mechanics. It has been widely used as an effective method to analyze granular materials, especially in granular flows, powder mechanics and rock mechanics. The granular materials are modelled as an assembly of particles in a DEM model. The trajectory and rotation of each particle are tracked to evaluate its position and orientation in a time stepping simulation. The interactions among particles, and between particles and their containing structures are computed using Newton's second law.

Many researchers have used the DEM to simulate the behavior of bulk grains in storage bins. Liu et al. (2008a) proposed a DEM model to simulate lateral pressure of corn in a bin with smooth wall and wheat in a bin with corrugated walls, respectively. Cleary and Sawley (2002) investigated the effect of the shape variation of particles on bulk density and found non-circular particles leading to higher bulk densities and highly elongated particles with random orientations had 5% more voids than circular particles, while very elongated particles resulted in 7% lower of bulk density than circular particles. Boac et al. (2010) conducted DEM simulations with varying material and interaction properties of soybean kernels to find property combinations that gave simulation results that correlated well with measured bulk properties of soybeans while maintaining or improving computational speed. Single- and multi-sphere (2-sphere, 3-sphere, and 4-sphere overlapping) soybean particle models were used in their DEM simulations of bulk density and bulk angle of response. By comparing the simulated results with the experimental findings in the literature, as well as computational time required in the simulations, the single-sphere model was found to best simulate soybean kernels.

Gonzalez-Montellano et al. (2011) developed discrete element models to simulate the

pore structure of particle assemblies considering spherical and non-spherical particles formed by clustering two spheres of 5 mm diameter with an aspect ratio of 1.5. The SP (single sphere) particles were generated randomly within this plane whilst the PP (paired-sphere) particles were generated in a rectangular lattice with a random orientation of the particle longitudinal axis. The non-spherical combined spheres model showed a more stable velocity field than did the single-sphere model, which produced the flow pattern closer to the ones observed in experiments. It indicated that multispherical particles would accurately represent the irregular shape of the real particles. Gonzalez-Montellano et al. (2011) developed 3D discrete element models to simulate the pore structure of glass beads and maize based on the preliminary parameters measured in experiments and in reported literature. In their research, the glass beads were simulated as spheres in a size distribution determined by a given mean diameter and standard deviation and the maize kernels were simulated as composing of six spheres representing the irregular shape of the real grains. It was found that the preliminary model for the glass beads worked well to predict the discharge flow but required calibration of friction values for the maize grain.

Coetzee and Els (2009) simulated corn kernels comprising of the clumps by adding two or more spheres together using DEM. Particles formed by the clumps remained at a fixed distance from each other and could overlap to any extent. The radius of the particles in the simulations was selected from a uniform distribution within the range according to the experimental data in the literature. The number of particles used to construct a clump was based on both the accuracy of the representation model and the computational time. To simulate porous beds consisting of non-spherical particles (spherical, cylindrical and polyethylene pellets), Grima

and Wypych (2011) used particles of two overlapping spheres to explore the effects of particle shape on the granular pile formation. Their results indicated that particle shape representation played a key role to obtain realistic mechanical and inter-locking behavior of real particles. However, there was a limitation of using two overlapping spheres along one axis to create a sphero-cylindrical like shape to restrict particle rotation around all axes and the moment of inertia.

A commercial DEM software package PFC^{3D} (Particle Flow Code in 3 Dimensions) has been used by many researchers for modeling the movement and interaction of particles in solid mechanics and granular flow (Cundall and Strack 1979; Baars 1996; Shimizu et al. 2004; Liu et al. 2008a, 2008b; Sobieski et al. 2012). In PFC^{3D} models, spherical particles can be created directly and non-spherical particles can be modeled by attaching two or more particles together as an autonomous object. PFC^{3D} has been used to simulate the formation of grain beds in storage bins (Itasca 2005). However, the bin size and number of particles that can be simulated by the PFC model is limited by the computer capacity (Liu et al. 2008b). It was solved by reducing the model size (radius) using a scaling factor determined by the density of bulk solids in PFC model, the test bin and the radius of test bin. That means the simulation results may be scaled up by proportionally increasing the grain density in the simulation model. This method reduced the simulation time from 24 hours for a cylindrical bin with 1.5 m (height) by 1.0 m (diameter) to 3 hours with one fifth of the original size (Liu et al. 2008b).

Sobieski et al. (2012) used DEM to simulate the pore structure of porous bed and developed a numerical algorithm to construct the pore-scale flow paths within the simulated spacial structure of porous bed to calculate the lowest geometric tortuosity. The porous bed

consisted of randomly arranged spherical spheres. The porous bed was treated as a series of tetrahedron units consisting of four spheres. Airflow was considered entering the tetrahedron unit by the base triangle and leaving through the triangle with the highest centroid, which was considered as the inlet of next tetrahedron unit. The airflow path was constructed as the series of lines connecting the centroids of base triangles from the bottom to the top surfaces of the porous bed. The tortuosity was calculated as the actual length of airflow path to the length of porous bed. The simulated tortuosity was found in good agreement with the values obtained from a CT image published in the literature. Later Dudda&Sobieski (2014) analyzed fluid flow through the porous bed based on the location and size of particles generated by a DEM model. An algorithm was developed to calculate the parameters (center of gravity, area and circumference, etc.) of the flow segment intersected by the flow path on the triangle face of tetrahedron units. The calculation results were verified in AutoCAD by creating the same geometry of the flow segment and presenting the parameters including the area, circumference and centroid coordinates of that region using an AutoCAD command. It was found that the calculation results were in good agreement with the results generated in AutoCAD (Dudda&Sobieski 2014).

2.3 Modeling flow through porous media

Much research has been done to investigate flow through porous media and many models have been developed to predict or estimate resistance to flow through porous media. Those models are grouped into theoretical models, empirical models, and numerical models in the following review.

2.3.1 **Theoretical models for flow through porous media**

Darcy developed the first law of flow resistance through porous media in 1856 (Darcy 1856). He designed experiments to describe water flow through sand filled pipes and found the flow rate of water through the filter bed was directly proportional to the area of sand and to the difference in the height between the fluid heads at the inlet and outlet of the bed, and inversely proportional to the thickness of the bed (Eq. 2.9).

$$Q = \frac{CA\Delta h}{L} \tag{2.9}$$

where

Q = the flow rate of fluid ($m^3\ s^{-1}$)

C = a property characteristic of the sand or porous media

A = the area of sand column (m^2)

$\frac{\Delta h}{L}$ = pressure gradient (Pa m^{-1})

L = the thickness of the bed (m)

In Eq. 2.9, the proportionality C can be replaced by k/μ, where μ is the viscosity of the fluid and k is the permeability of the porous medium, which is a property of porous medium only and reflects the ability of a porous medium to allow fluid pass through it. Then Darcy's equation can be stated as

$$-\frac{dp}{dL} = \frac{\mu}{\kappa} v \tag{2.10}$$

where

dL = a segment (m) along which a pressure drop occurs (dp) (Pa)

μ = dynamic viscosity coefficient (Pa s)

k = permeability coefficient (m^2)

v = the fluid velocity (m s^{-1})

The following assumptions were followed when Darcy's law was established (Amao 2007):

1) The flow is continuous and steady.

2) The flow is incompressible.

3) The flow is laminar or viscous flow and the inertia effects are neglected.

The most important property parameter in Darcy's law is the permeability coefficient for determining the pressure drop. Darcy's flow regime is applicable only for the isothermal Newtonian fluid at very low Reynolds number (Re) where the viscous effect is dominant (Morais et al. 2009).The Reynolds number for packed beds R_e is defined as (Bird et al. 1996):

$$R_e = \frac{\rho v_s D_p}{\mu(1-\emptyset)} \tag{2.11}$$

where

ρ = fluid density (kg m^{-3})

v_s = superficial velocity (m s^{-1})

D_p = diameter of the spherical particles (m)

μ = fluid viscosity (kg (m s)$^{-1}$)

$\emptyset$ = porosity

The fully laminar condition exists for Reynolds number less than about 10 and fully turbulent flow at Reynolds numbers greater than around 2000 (Rhodes 2008).

Groisman and Quake (2004) presented a microfluidic rectifier (a microscopic channel of a special shape whose flow resistance is strongly anisotropic) and tested the pressure drop across the channel at different Reynolds numbers. The patterns of flows became different at different

Reynolds numbers. Specifically, at higher Reynolds numbers, nonlinearity in the flow developed. Turbulent flow with higher Reynolds numbers increased the resistance dramatically so that large increases in pressure would be required to further increase the volume flow rate, in which Darcy's law would always underestimate the true pressure drop.

For the higher fluid velocity and low viscosity, inertial effects may become significant. Forchheimer (1901) modified Darcy's law by adding a second-order velocity term as shown in Eq. 2.12 to account for the inertial effects:

$$-\frac{dp}{dL} = \frac{\mu}{\kappa} v + \beta \rho v^2 \tag{2.12}$$

where

ρ = the fluid density (kg m^{-3})

β = the Forchheimer coefficient (m^{-1}) (β factor)

The Forchheimer coefficient is determined usually by fitting experimental data and the value was found to verify with porous beds tested (Teng and Zhao 2000). Similar to the permeability, the Forchheimer coefficient depends on the medium properties, such as porosity. Based on experimental measurements, various correlations between the permeability and the Forchheimer coefficient have been established, such as Eq. 2.13 (Jones 1987)

$$\beta = c_1 \cdot k^{c_2} \tag{2.13}$$

where

c_1, c_2= geometrical parameters

Both c_1 and c_2 are dependent on the properties of porous medium (e.g., porosity, pore connectivity, pore size distribution). The permeability and the Forchheimer coefficient also can be determined by fitting the experimental data with the Forchheimer equation (Jambhekar 2011).

Ergun (1952) presented an equation (Eq. 2.14) for flow through a porous bed consisting of spherical particles, in which the permeability and the Forchheimer coefficient were determined by considering the effect of porosity and particle diameter on pressure drop:

$$\Delta P = A\frac{\mu(1-\emptyset)^2}{{d_e}^2\emptyset^3}v + B\frac{\rho(1-\emptyset)}{d_e\emptyset^3}v^2 \quad (2.14)$$

where

ΔP = the pressure drop per unit depth (Pa m^{-1})

A = the viscous constant

B = the inertial constant

v = superficial velocity ($m^3(m^2\ s)^{-1}$)

$\emptyset$ = porosity

d_e= the equivalent particle diameter (m)

In Eq. 2.14, the pressure loss is treated as the sum of the kinetic losses and viscous energy losses. The first term dominates the resistance under laminar flow conditions, while the second term dominates under turbulent flow conditions. The combination of A and B is dependent on the ranges of the particle diameter, bed porosity and Reynolds number (Tian et al. 2016). Carman and Kozeny (Carman 1937; Kozeny 1927, 1933) developed an equation (Eq. 2.15) for laminar flow through randomly packed particles with diameter ranging from 0.25 to 50 mm:

$$\frac{\Delta P}{L} = 180\frac{\mu(1-\emptyset)^2}{{D_p}^2\emptyset^3}v \quad (2.15)$$

The Carmen-Kozeny equation only considers the kinetic losses and is applicable to laminar flow through a randomly packed bed of particles (Rhodes 2008).

Ergun's equation is widely used to predict packed bed pressure drops over the entire range of flow conditions. Hicks (1970) thought that the two coefficients (A=150 and B=1.75) in

Ergun's equation were not constants, rather as functions of Reynolds number. Ergun's equation is found to be mainly applicable for spherical particles in the porosity range of 0.35-0.55 (Nemec and Levec 2005; Endo et al. 2002; Hill et al. 2002), but not applicable to predicting the pressure drop across irregular beds, which is defined as beds with random arrangement of particles (spheres, cylinders, rings, or planes), non-uniform in size and different configurations throughout the beds (Handly and Heggs 1968). Some measured values of pressure drop for the cylindrical packing bed were only a half of those predicted by Ergun's equation (Bradshaw and Myers 1963). Also Ergun's equation was based on straight tube geometry of pore space and didn't take into account the connectivity and tortuosity of pore structure (Wu et al. 2008). Two empirical constants in Ergun's equation (150 and 1.75) have no physical meaning (Wu and Yin 2009) and may have different values at different porosities (McDonald et al. 1979)

All the models reviewed above have some common following assumptions:

1. The fluid flow is incompressible. At low velocity, the change of density of flow by the pressure could be ignored.
2. Pores and particles are uniformly distributed. The porous bed is assumed as a regular packing bed consisting of uniform sized particles (spheres, cylinders, etc.) repeated in the same arrangement.
3. The porous medium is isotropic and homogeneous, which does not react with the fluid.

2.3.2 **Empirical models for flow resistance through grain bulks**

Hendernson (1943; 1944) studied the resistance of airflow through shelled maize, soybeans, and oats and fitted the experimental data to a relationship between the airflow rate

per unit cross-sectional area and pressure drop for a given depth represented by a power function as follows:

$$Q = K\Delta P^{C} \tag{2.16}$$

where

Q = airflow rate per cross-sectional area (cfm ft^{-2})

ΔP = static pressure drop per ft, depth (in. of water ft^{-1})

K and C = constants depending on the depth of grain bed

For maize and soybeans, K was found to decrease and C to increase slightly with increasing grain depth. Whereas for oats, the plot of airflow rate against static pressures failed to give a straight line in the log scale.

Shedd (1945) repeated Henderson's work on ear corn at a moisture content of 20% for bed depths varying from 1 to 3.66 m (1 to 12 ft) and proposed a simplified equation (Eq. 2.17) involving the same variables

$$Q = 300\sqrt{\frac{\Delta P}{D}} \tag{2.17}$$

Then Shedd (1953) measured pressure drops in different grain beds at various airflow rates and found that the best relationship between airflow velocity and pressure drop was of the following form:

$$V = A\Delta P^{B} \tag{2.18}$$

where

V = airflow rate ($m^3\ s^{-1}\ m^{-2}$)

ΔP = pressure drop per unit depth of grain bed (Pa m^{-1})

A and B = constants for a particular grain

However, Shedd's equation was not able to accommodate some of his experimental observations. It performed well at certain velocities (0.005 - 0.3 m s^{-1}) but not for higher velocities. Based on Shedd's equation, Hukill and Ives (1955) proposed another equation (Eq.2.19) which performed well for a larger range of velocities (0.01-2.0 m s^{-1}) which covers both laminar and turbulent flow regimes).

$$\Delta P = \frac{A_2 V^2}{\ln (1+B_2 V)} \tag{2.19}$$

where

A_2 and B_2 = empirical constants

Hukill and Ives equation explains the non-linear nature of resistance to airflow data. The model is used in ASABE Standard to represent the airflow pressure drop data for selected grain. However, in Hukill and Ives equation，the air velocity cannot be directly rewritten as a relationship with pressure drop (Sergerlind 1983).

Shedd's equation and Hukill and Ives equation have been widely used to estimate pressure drops in grain bulks at different airflow rates (Kumar and Muir 1986; Sokhansanj et al. 1990; Jayas et al. 1991a; Alagusundaram et al. 1992; Jayas et al. 1991a; Nalladurai et al. 2002; Agullo and Marenya 2005). However, those equations have empirical constants and cannot be considered as universal. In addition, no parameters of grain bulks (porosity, interconnectivity, tortuosity, etc) and not fluid property (viscosity, Reynolds number) were considered in calculating the resistance to airflow.

2.3.3 **Numerical models for flow resistance through porous media**

Various numerical models have been developed to investigate the flow behavior in porous

media. Depending on the length scale, those models can be divided into three types: macroscopic models, continuum models, and pore-scale models (Thompson and Fogler 1997). In macroscopic models, the continuity equation together with momentum is solved and constitutive equations such as Darcy's law are utilized for velocity. These models are based on the validity of the constitutive relationships and require some inputs for semi-empirical parameters (e.g., relative permeability), and have difficulties accounting for heterogeneity, and complex pore interconnectivity (Balhoff et al. 2007). The scale of the physical parameters in macroscopic models is larger than the pore dimensions (Thompson 2002). The continuum approach applies the conservation equations at the macroscopic level by averaging the physical parameters (permeability, capillary pressure, superficial velocity, etc.) determined by experiments, while neglecting the interconnectivity and tortuosity of pore structures of porous media. Also the continuum modeling is length scale dependent. The small length may result in the averaged parameters meaningless and large scale may require upscaling. Heterogeneity, pore interconnectivity, and non-uniform flow behavior at the pore scale cannot be resolved explicitly at the macroscopic scale (Thompson 2002).

Capillary-bundle models are the simplest type of pore-scale models, which incorporate flow variation but neglect the effects of connectivity and tortuosity of porous medium. Wu et al. (2008) presented a model for resistance of flow through porous media by combining the average hydraulic radius model (Eq. 2.20) and the contracting-expanding channel model (Eq. 2.21). The total pressure drop was determined as the sum of the pressure drop caused by the viscous energy loss and the kinetic energy loss along the flow path. The model modified Ergun's equation by replacing the two constants, namely 150 and 1.75, by two expressions as a

function of tortuosity, porosity, the ratio of pore diameter to throat diameter, and the particle diameter, as well as fluid properties (Eq. 2.22).

$$\frac{\Delta P_1}{L} = \frac{72\mu\tau(1-\emptyset)^2 v_s}{{D_p}^2\emptyset^3} \tag{2.20}$$

$$\frac{\Delta P_2}{L} = \frac{3\tau(1-\emptyset)\rho v_s(\frac{3}{2}+\frac{1}{\beta^4}-\frac{5}{2\beta^2})}{4\emptyset^3 D_p} \tag{2.21}$$

$$\frac{\Delta P}{L} = \frac{\Delta P_1}{L} + \frac{\Delta P_2}{L} = \frac{72\mu\tau(1-\emptyset)^2 v_s}{{D_p}^2\emptyset^3} + \frac{3\tau(1-\emptyset)\rho v_s(\frac{3}{2}+\frac{1}{\beta^4}-\frac{5}{2\beta^2})}{4\emptyset^3 D_p} \tag{2.22}$$

where

ΔP = total pressure drop (Pa m^{-1})

ΔP_1 = pressure drop due to the viscous energy loss (Pa m^{-1})

ΔP_2 = pressure drop due to the kinetic energy loss (Pa m^{-1})

μ = viscosity of fluid (Pa s)

$\emptyset$ = porosity of porous media

v_s = superficial velocity of fluid (m s^{-1})

D_p= diameter of particles (m)

τ = tortuosity of fluid

L = length along the macroscopic gradient in porous media (m)

The underlying assumptions in those models were as following:

(a) The porous medium is isotropic and homogeneous

(b) The pores and particles are uniformly distributed

Volume-averaging is a widely used method in which a macroscopic momentum equation is derived from the Naviers-Stokes equation averaged over a small representative elementary volume. Du Plesis and Maslivyah (1991) and Du Plessis and Woudberg (2008) applied the volume-averaging concept to a Representative Unit Cell (RUC) model for flow through

isotropic granular porous media. The RUC was defined as the smallest rectangular control volume into which the average geometric properties of the granular packed bed were embedded (Fig. 2.2). In the RUC model, U_s denotes the solid phase volume and U_f the fluid phase volume, while the total volume is given as U_o. The corresponding linear dimension of the solid cube is d_s, and the linear dimension of the RUC is d. The RUC model considers interconnectivity of the pore spaces and avoids the introduction of empirical coefficients. Based on the mean geometrical properties of an idealized microstructure, the momentum transport equations are derived, which is applicable to porous media over the entire porosity range from zero through unity (Du Plesis and Maslivyah 1991).

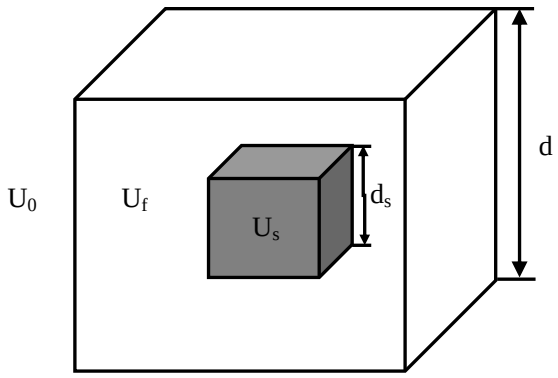

Fig. 2.2. Illustration of the Representative Unit Cell (RUC) model

Network modeling is a useful tool to study the flow and transport phenomenon in porous media at the pore-scale. In pore-scale network models, the pore structure can be approximated by 2D networks (Xiao et al. 2008; Yiotis et al. 2010; Ljung et al. 2012; Lao et al. 2004) or 3D networks (Kharaghani et al. 2010; Wang et al. 2012; Zhang et al. 2013; Surasani et al. 2010). While 2D pore network models are relatively simple, 3D irregular pore network models, consisting of either spherical or cylindrical particles, better represent the real pore structures in

porous media. The pore networks are either created by computational algorithms (Chu and Ng 1989; Bryant et al. 1992; Thompson and Fogler 1997; Blunt and King 1990; Thompson 2002; Kharaghani et al. 2010; Chareyre et al. 2012) or extracted from image processing (Monga et al. 2007; Al-Kharusi and Blunt 2007; Dong 2007; Nasiru 2009; Huang et al. 2013; Zhang et al. 2013; Wang et al. 2012). In network modelling, the pore space of porous medium is discretized into an interconnected set of pores and pore throats, such as triangles using Delaunay triangulation for 2D pore network models (Blunt and King 1990), and spheres connected by cylinders (Bafna and Baird 1992; Sangani and Acrivos 1982; Larson and Highdon 1987) and tetrahedrons using Delaunay and Voronoi tessellations (Jerauld et al. 1984a, b; Thompson and Fogler 1997; Blunt and King 1990; Mason and Mellor 1991; Thompson 2002) for 3D pore network models.

Network modeling has been widely used in investigating pore-scale flow mechanics and macroscopic behavior (permeability, relative permeability and capillary pressure) of single-phase and multiphase-phase flow, Newtonian and Non-Newtonian flow through idealized lattices, and disordered packing of spheres (Fatt 1956; Haring and Greenkorn 1970; Mohanty and Salter 1982; Lin and Slattery 1982; Bakke and Oren 1997; Bryant et al. 1993a, 1993b; Bryant and Blunt 1992; Lopez et al., 2003; Balhoff and Thompson 2004; Valvatne and Blunt 2004).

Fatt (1956) developed a solution method for network models. Specifically, fluid transport was modeled by using fluid conservation equations and a flow conductivity was assigned to each pore in the network. Applying the boundary conditions (most commonly a pressure gradient in one direction), a numerical solution of overall pressure and velocity within the

network was obtained. Thompson and Fogler (1997) proposed a pore-scale network approach to study flow through a packed bed. The packed bed was simulated as an assembly of random spheres with a specified volume. An algorithm called Delaunay tessellation was used to develop the network of pores and throats by dividing spheres into nearest-neighbor groups of four to form tetrahedron units. Flow was considered through each pore (space in the group of spheres) by any of four pore throats (constrictions that are created where three spheres meet). The final flow solution was obtained from a linear matrix equation representing fluid conservation at each pore by applying the balance on the net volumetric flow rate in each interior tetrahedron. The linear matrix equation was solved at the pore level and the overall pressure and flow profiles were obtained.

Voronoi-Delaunay tessellation is another technology to construct irregular lattice with topological and morphological information for calculating the transport coefficients without distorting the lattice structure obtained or introducing arbitrary or empirical parameters (Vrettos et al. 1989). Voronoi-Delaunay tessellation has been also applied to studying percolation properties and the modelling of reservoir work (Winterfeld et al. 1981; Jerault et al. 1984; Pathak et al. 1980). Vrettos et al. (1989) applied the Voronoi – Delaunay tessellation technique to simulate a network of cylindrical pores consisting of a random packing of uniform spheres. The structural characterization (pore diameter, pore angle and pore length distribution) generated was used to calculate the effective transport coefficients of various transport modes. The results of ordinary diffusion were in good agreement with the experimental data whereas the errors existed when estimating the pore overlapping volume for Knudesen and viscous flow. The Voronoi network has been used to model multiphase flow in disordered fibrous materials

at the pore scale. The results have shown that Voronoi network modelling is a powerful tool to quantify macroscopic transport based on microscale properties (Thompson 2002).

Lao et al. (2004) developed a 2D computational method to construct a random pore network model by dividing the porous medium into a series of cylindrical pipes with different orientations, lengths, diameters and connectivity. Based on the porosity and the pore size distribution of the medium, they calculated the medium properties, such as the permeability, the Forcheheimer coefficient, and the relationship between them. The results were in good agreement with theoretical and experimental results.

The Lattice Bolzmann method (LBM) has developed into an efficient algorithm for simulating single-phase and multiphase fluid flows through porous media and modelling physics in fluids, especially dealing with complicated boundaries (Chen and Doolen 1998). Based on the Boltzmann equation, the LBM considers the microstructure of porous medium as a lattice meshwork in which the representative volume element is represented by a particle velocity distribution function for each fluid component at each grid point. Applying the boundary conditions, a numerical solution of the Boltzmann equation at the pore-scale is obtained. Gao et al. (2012) developed a Lattice Boltzmann (LB) model combined with X-ray computed tomography to simulate fluid flow at pore-scale to calculate the anisotropic permeability of porous media. Their results showed that the LB model was efficient to simulate pore-scale flow in porous media and investigate the anisotropic permeability.

2.3.4 **Summary of model review**

Classical theoretical models, such as Darcy's law, Forchheimer's law and Ergun's

equation usually work for certain airflow velocity and do not take into account the interconnectivity and tortuosity of the pore structure of porous media. Empirical models (Shedd's equation, Hukill and Ives' equation) are fitted from the experimental data by measuring the pressure drop along a column of material at different flow rates. The empirical constants in those models are dependent on the grain bulks, which results in those models may not work for different grain bulks. Numerical models like RUC model, Capillary-bundle models considers the mean geometrical properties of an idealized microstructure and the derived momentum transport equations are applicable to porous media over the entire porosity range. Pore-scale network models are powerful to simulate the pore structure of porous medium and investigate the interconnectivity and tortuosity of the pore structure. In pore-scale network models, the pore structure is characterized by the sizes and locations of particles, the orientations of pores and their connectivity via pore-throats. However, in reality the detailed pore structure of real materials is rarely known and the idealized arrays of geometrically simple pores and pore-throats are assumed to study the flow behavior in porous media. Secondly, it is difficult to obtain general solutions to the equations of motion in these complex pore geometries. Therefore, there is a need to develop a model to take into account the connectivity and tortuosity of the pore structures of porous media and integrate it with the fluid mechanics to predict the resistance to airflow through porous media.

3 Materials and Methodology

A porous medium is made up of solid particles and random-size pores between particles. Given that the pore structure is highly randomized in its nature, it is challenging but vital to characterize the geometrical pattern of pore structure to understand fluid flow within the medium. As illustrated in Fig.3.1, when fluid (air) enters a porous medium, the flow paths consisting of interconnected pores are random and multiple. Most of previous research assumed simple (idealized) pore structures and used representative unit volumes to average the flow resistance along the flow path. However, the resistance to flow through each pore is different, which results in complex paths of flow through the porous medium. The proposed methodology was concentrated on flow behavior through each pore based on the pore structure simulated by a discrete element model. There were four main steps in the proposed methodology: (1) developing a discrete element model to simulate the pore structures of porous beds; (2) developing an algorithm to quantify airflow paths based on the simulated pore structure, (3) developing a pore-scale branched path flow model and a network model based on simulated airflow paths for predicting the resistance to airflow; and (4) conducting experiments to validate the airflow resistance models. These four steps are discussed in the following sections.

3.1 DEM modelling of pore structures in grain bulks

A commercial software package PFC^{3D} (4.0 EV, Itasca Consulting Group Inc., Minneapolis, MN) was used to develop a DEM model to simulate porous beds filled with soybeans. Two bed configurations were simulated based on the availability of experimental

data for model validation. The first bed was a small-scale rectangular grain bin of 0.25×0.02×0.275 m filled with soybeans (Fig. 3.1a). This bin was used by Nwaizu and Zhang (2015) in their experiments to investigate airflow paths using smokes and imaging techniques. The second bed was a cylindrical bin of 0.15 m in diameter and 0.28 m in height and filled with soybeans to a depth of 0.25 m (Fig. 3.1b). This bin was used by Liu et al. (2012) to conduct experiments for determining the effect of vibration on pore structures. Both bins were made of Plexiglas. The first bin was simulated for airflow paths and the second bin for vibration effect.

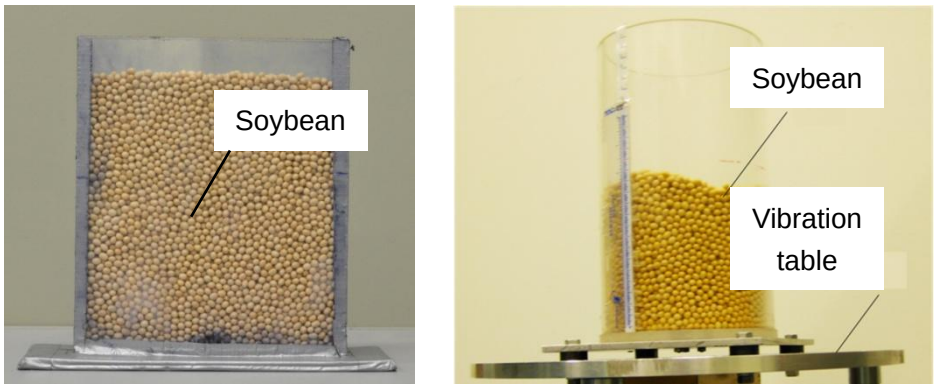

Fig. 3.1. Small-scale grain bins filled with soybeans. (a) rectangular bin used by Nwaizu and Zhang (2015), (b) cylindrical bin subjected to vibration, used by Liu et al. (2012).

Soybeans were selected because of their smooth surface and relative round shape so that the grain bed could be simulated as an assembly of spherical particles. It should be noted that soybean kernels were not completely spherical, but they resemble a sphere with high average sphericity values (above 0.8), and therefore, most researchers have used spheres to approximate soybean kernels when simulating bulk soybean characteristics in DEM models to reduce computation times (Boac J.M. et al., 2014). The measured average long, intermediate, and short axis dimensions for soybean used in this study were 7.6, 6.7, and 5.7 mm, respectively, and the corresponding geometric mean diameter was 6.6 mm, and sphericity 0.87.

The PFC^{3D} model essentially simulated the formation process of a grain bed. Firstly, the boundaries of the model were defined by walls to create the Plexiglas container with given normal and shear stiffness (Table. 3.1). Secondly, balls (spherical particles representing grain soybean kernels) were filled into the bin one by one to form a porous bed (an assembly of balls) at a prescribed porosity. During the bed formation process, the movement of each ball was tracked and its coordinates were calculated as the bed approached a (force) equilibrium state. Interaction between particles was governed by contact and frictional forces. Newton's second law was used to calculate motion of each particle and a force-displacement law at the contacts to update the contact forces. Both displacements and rotations of discrete balls were calculated. Complete detachment between balls was permitted and contacts between balls were automatically detected and updated during simulation (Itasca, 2005).

To achieve the prescribed porosity, small-radius (R_0) particles were generated first and then particle sizes were increased using an initial radius multiplication factor until the desired porosity was obtained (Itasca, 2005). The process is described as follows. First, the porosity was calculated

$$\emptyset = 1 - V_p/V \tag{3.1}$$

$$V_p = \sum \frac{4}{3}\pi R^3 \tag{3.2}$$

where

$\emptyset$ = target (prescribed) porosity

V_p = total volume occupied by particles

V = total volume of the porous bed

R = radius of an individual particle

And then, the total void volume was determined:

$$\emptyset V = V - \sum \frac{4}{3}\pi R^3 \tag{3.3}$$

From Eq. 3.3, the particle radius was calculated:

$$\sum R^3 = 3V(1-\emptyset)/4\pi \tag{3.4}$$

If the initial particle radius was assigned as R_0, and the corresponding porosity was $\emptyset_0$, from equation (3.4), we obtained:

$$\frac{\sum R^3}{\sum {R_0}^3} = \frac{1-\emptyset}{1-\emptyset_0} \tag{3.5}$$

where

R_0 = initial particle radius

$\emptyset_0$ = initial porosity

A radius multiplication factor was introduced to increase (expand) the particle radii gradually to achieve the desired (prescribed) porosity.

$$R = mR_0 \tag{3.6}$$

$$m^3 = \frac{1-\emptyset}{1-\emptyset_0} \tag{3.7}$$

where

m = radius multiplication factor

An initial guess of the radius multiplier m was made, based which an initial porosity was calculated from:

$$\emptyset_0 = 1 - (1-n)/m^3 \tag{3.8}$$

The mean particle radius and the number of particles generated were calculated:

$$\overline{R} = \left\{\frac{3V}{N4\pi}(1-\emptyset_0)\right\}^{\frac{1}{3}} \tag{3.9}$$

$$N = \frac{3V}{4\pi}(1-\emptyset_0)/\overline{R}^3 \tag{3.10}$$

where

N = the number of particles generated

$\overline{R}$ = the mean particle radius

3.2 Simulating grain beds subjected to vibration

Grain beds are often subject to vibration during operations. Vibration may cause significant changes in pore structures of grain beds. DEM simulations were conducted to explore the effect on vertical vibration on pore structures of grain beds. Once the porous bed was formed in the DEM model (discussed in the previous section), a vibration excitation was applied. Simulations were conducted for a model bin of 0.28 m height and 0.15 m in diameter, filled with soybeans. This bin was used by Liu et al. (2010) to study the vibration of soybean during storage. Therefore the simulation results could be compared with the data reported by Liu et al. (2010). A simple harmonic excitation was used to vibrate the bin. Vibration excitation was applied to bin floor in the vertical direction with prescribed frequencies and amplitudes as follows:

$$D_z(t) = A\sin(\omega t) \tag{3.11}$$

where

$D_z(t)$ = displacement in the vertical direction (m)

A = vibration amplitude (m)

ω = angular velocity (rad s^{-1}), = $2\pi f$

f = vibration frequency (Hz)

t = time (s)

A frequency of 15 Hz and amplitudes of 0.5, 1.0, 2.0, 3.0 and 4.0 mm were used in simulations. These frequency and amplitudes combinations were selected to achieve the

maximum densification. According to the experimental results reported by An et al. (2009), the dense packing was achieved with vibration intensity between 1.5g (g= gravitational acceleration) and 4.0g (the peak density occurred at 2.0g - 2.5g). The vibration intensity levels, determined as $A(2\pi f)^2$, were 0.45g, 0.91g, 1.81g, 2.72g, and 3.62g for amplitudes of 0.5, 1.0, 2.0, 3.0, and 4.0 mm at 15 Hz, respectively.

Vibration was simulated in time steps of 3.3 μs. This time step (Δt) was determined from the mass (m) and the stiffness (k) of particles ($\Delta t = \sqrt{m/k}$) (Itasca, 2005). Preliminary simulations were conducted to determine the total length of vibration time required to reach the maximum density and it was found the 16 s was sufficient for all vibration intensities. At each time step, the position (x, y and z coordinates) of each particle was saved in a data file for late use in calculating flow parameters.

One of the most important parameters affecting flow through a porous bed is porosity. In this study, both global (overall) and local porosity values were calculated based on DEM simulation data. The global porosity was calculated as the ratio of the total volume occupied by the particles to the total volume of porous bed.

$$\emptyset = 1 - V_p/V \tag{3.12}$$

$$V_p = \sum \frac{4}{3}\pi r^3 \tag{3.13}$$

where

$\emptyset$ = global porosity (decimal fraction)

V = total volume of porous bed (m^3)

V_p = total volume occupied by particles volumes (m^3)

r = particle radius (m)

Σ = summation of all particles in the porous bed

In a porous bed consisting of randomly packed particles, the pore distribution would not be uniform. Therefore, local porosity was also determined using the built-in function in PFC^{3D} at five locations, which were denoted as B1(0.06, 0, 0.119), B2(0.06, 0, 0.129), B3(0.06, 0, 0.130), B4(0.06, 0, 0.136), and B5(0.06, 0, 0.146) (three numbers in parenthesis are x-, y- and z- coordinates, respectively) (Fig. 3.2). The instantaneous local porosity values at these locations were calculated at every time step (3.3 μs) during vibration simulation.

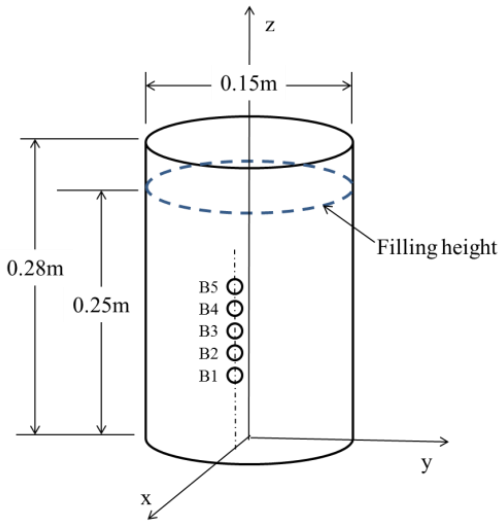

Fig. 3.2. A Schematic of simulated bin showing the locations (B1-B5) where local porosity was calculated

3.3 Physical properties of grain and bin for DEM simulations

The DEM model requires parameters of grain and grain bin, including particle diameter, bulk density, porosity, particle stiffness, friction coefficient between particles, friction coefficient between particle and wall. All of the physical properties of grain and bin used in the

simulations were shown in Table 2, which were adopted from a previous study on DEM modeling of grain beds filled with soybeans reported by Liu et al. (2008a). Both the normal stiffness and shear stiffness for the bin wall were determined from the modulus of the bin wall as follows (Liu et al. 2008a):

$$k_n = Et \tag{3.14}$$

$$k_s = 0.5\ k_n \text{to } 1.0\ k_n \tag{3.15}$$

where

k_n = normal stiffness of wall (N m^{-1})

k_s = shear stiffness of wall (N m^{-1})

E = elastic modulus of Plexiglas wall (3.03 GPa) (Mohsenin 1980)

t = thickness of wall (m)

Similarly, the normal stiffness and shear stiffness of grain were determined from modulus elasticity of the grain as follows:

$$k_{pn} = E_p(2d_p) \tag{3.16}$$

$$k_{ps} = 0.5\ k_{pn} \text{ to } 1.0\ k_{pn} \tag{3.17}$$

where

k_{pn} = normal stiffness of grain kernel (N m^{-1})

k_{ps} = shear stiffness of grain kernel (N m^{-1})

E_p = elastic modulus of grain kernel, which is a measurement of grain kernel's resistance to being deformed elastically when a force is applied to it. Elastic modulus was determined through compression test by Liu et al. (2007).

d_p= diameter of grain kernel (m)

Internal friction angle, friction coefficient between particle and wall were determined by direct shear test (Liu et al. 2008a). The particle density and porosity were assumed to be 1285 kg m^{-3} and 40.8% (Milani et al. 2000).

Table 3.1. PFC simulation parameters reported by Liu et al. (2008a).

Parameters	value
Wall normal stiffness (k_n), N m^{-1}	1.8×10^7
Wall shear stiffness (k_s), N m^{-1}	0.9×10^7
Particle normal stiffness (k_{pn}), N m^{-1}	4.0×10^6
Particle shear stiffness (k_{ps}), N m^{-1}	2.0×10^6
Friction coefficient between particles	0.47
Friction coefficient between particle and wall (Plexiglass)	0.3
Particle density (ρ_p), kg m^{-3}	1285
Bulk density (ρ_b), kg m^{-3}	761
Porosity (Ø), %	40.8
Particle diameter (d_p), mm	5.5-7.5

3.4 Simulation of airflow paths through grain bulks

3.4.1 Algorithm for calculating airflow paths

Algorithms were developed in MATLAB (R2013b, Mathworks Inc., USA) to determine all the possible paths (the widest, narrowest, etc.) for airflow through the pore spaces between particles in grain beds based on the locations and sizes of balls (grain kernels) simulated by the DEM model. These algorithms treated the porous bed as a collection of four-particle tetrahedron units stacked over each other from the bottom to the top of the grain bed (Fig. 3.3), as proposed by Sobieski et al. (2012). Each tetrahedron unit had four "throats" (T1-T4), with T1 being the space between particles A, B and C (ΔABC), T2 between particles A, B and D (ΔABD); T3 between particles A, C and D (ΔACD); and T4 between particles B, C and D (ΔBCD). If air entered the tetrahedron unit through a throat, say T1, it could exit from T2, T3 or

T4. In other words, there were three possible airflow paths through each tetrahedron unit, termed as local paths in this thesis.

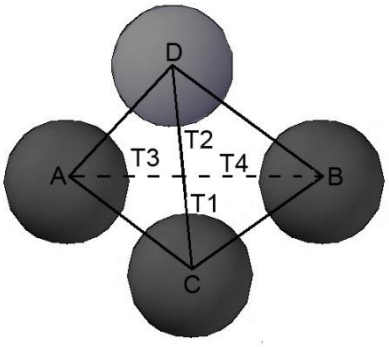

Fig. 3.3. A tetrahedron unit representing grain mass at a point in the grain bed.

Because air flows from the bottom to the top in typical grain bins during aeration or in-bin drying, and therefore a random point at the bottom of the grain bin was first selected as an air entrance point (AEP). An AEP was physically a pore space between particles on the bin floor. Three particles nearest to the AEP were selected to form the pore space for AEP, and these three particles also formed the initial base triangle of a tetrahedron unit. The next step was to find a particle as the fourth vertex to construct a tetrahedron. All the particles in the grain bed whose coordinates had been determined by the DEM model were sorted by their distances to the centroid of the base triangle and the particle that was closest to the base triangle was selected as the first candidate for the fourth particle to construct the tetrahedron.

A candidate particle was confirmed to be the fourth particle of the tetrahedron if the following two conditions were met: (1) the center of the fourth particle should be higher than the centroid of the base triangle because the air flows upwards; and (2) the space among the four particles that formed the tetrahedron should be sufficiently small (not be able to accommodate another particle inside the tetrahedron), i.e., the inscribed sphere within the

tetrahedron must be smaller than a particle. If these conditions were not met, the next closest particle was considered, and the process was repeated until a suitable particle was found as the fourth particle to form a tetrahedron. Once a tetrahedron was constructed, the air was assumed to enter the tetrahedron through the base triangle (T1) and exit through the other three triangular faces of the tetrahedron (T2, T3 and T4) (Fig. 3.3). The length of a local path was determined as the distance between the centroids of the two triangles associated with the path. For example, the length of the T1-T2 path was the distance between the centroids of ΔABC and ΔABD (Fig. 3.3).

Among the three local airflow paths in each tetrahedron unit, one had the widest cross-section and one had the smallest (narrowest) cross-section, representing the widest and narrowest flow path, respectively. To determine which of the three paths was the widest or the narrowest path, the areas of the three "exit" triangles were calculated by the Huron equation and compared (Kendig 2000):

$$S = \sqrt{p \times (p-a)(p-b)(p-c)} \tag{3.18}$$

$$p = \frac{1}{2}(a+b+c) \tag{3.19}$$

where

p = a half of perimeter of triangle

a, b, c= lengths of three sides of triangle

The open area was calculated as the area of face triangle less the projected area of three particles on the triangle face (Dudda W. and Sobieski W., 2014). Take ΔACD as an example (Fig. 3.4), the total area of triangle was calculated as follows:

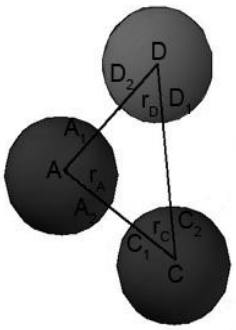

Fig. 3.4. Illustration of the cross-sectional area for airflow through a triangle.

$$p = \frac{1}{2} \times (AC + AD + CD) \tag{3.20}$$

$$S(\Delta ACD) = \sqrt{p \times (p - AC)(p - AD)(p - CD)} \tag{3.21}$$

The areas occupied by the three particles A, C, D were calculated respectively as follows:

$$\begin{aligned} S(A_1AA_2) &= \frac{1}{2} \times \angle CAD \times {r_A}^2 \\ S(C_1CC_2) &= \frac{1}{2} \times \angle ACD \times {r_C}^2 \\ S(D_1DD_2) &= \frac{1}{2} \times \angle ADC \times {r_D}^2 \end{aligned} \tag{3.22}$$

where

$S(A_1AA_2)$, $S(C_1CC_2)$, $S(D_1DD_2)$= the areas occupied by particles A, C, D, respectively, within triangle ACD

r_A, r_C, r_D = radius of particles A, B, C, respectively

Therefore, the (open) area available for air flow through ΔACD was calculated as:

$$S_f = S(\Delta ACD) - S(\Delta A_1AA_2) - S(\Delta C_1CC_2) - S(\Delta D_1DD_2) \tag{3.23}$$

The triangle with the largest open area was selected as the exit triangle for the widest path, whereas the triangle with the smallest open area was selected as the exit triangle for the narrowest path. Once a triangle was selected, the actual pore throat area was calculated as the

open space between the three particles that formed the triangle (Fig. 3.5). The equivalent path width was considered as the diameter of a circle which had the same area as the open area.

$$d_f = 2\sqrt{\frac{S_f}{\pi}} \tag{3.24}$$

where

d_f = equivalent airflow path width (diameter) of a local path

S_f = open area between three particles in a triangular face of tetrahedron (m^2)

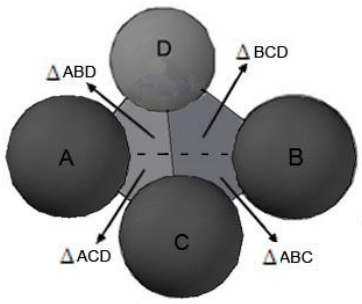

Fig. 3.5. Pore throat sizes for airflow paths in a tetrahedron unit.

After the local paths within the first tetrahedron were determined, the corresponding exit triangle (outlet) was used as the base triangle (inlet) to construct the next connecting tetrahedron. The process was repeated from the bottom to the top of the grain bed until the last tetrahedron unit reached the top surface of the grain bed (Fig. 3.6). The total airflow path length was then calculated as the sum of lengths of all associated local flow paths (LFP) (LFP1 + LFP2 + ……,), or the sum of distances connecting the centroids of base triangles in all associated tetrahedron units (Fig. 3.6).

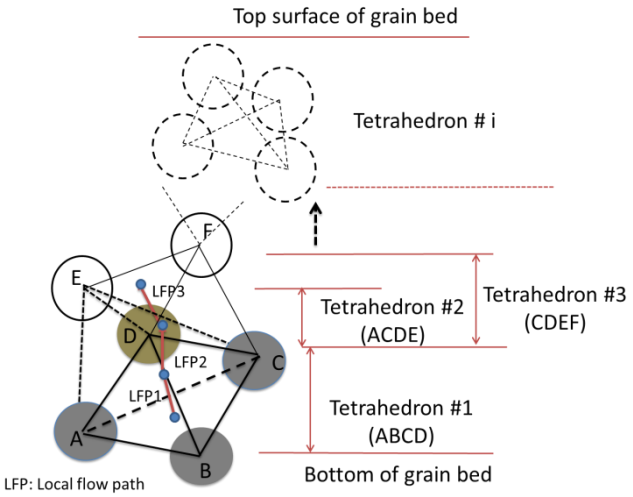

Fig. 3.6. Illustration of the step-increment procedure to construct a global airflow path.

However, this step-increment procedure of constructing a flow path might not always converge. There were two cases that required reselecting the exit triangle to arrive at convergency. In the first case, when the exit triangle from the current tetrahedron was selected as the base triangle for the next tetrahedron, the area S of the exit triangle overlapped with other triangles of a tetrahedron unit that had been used in a previous step. This case is graphically illustrated in Fig.3.7 where air enters the current tetrahedron unit from ΔABC. If ΔABD was selected as the base triangle to construct the next tetrahedron unit with particle E, air would passed through ΔACD which had been considered in last tetrahedron to reach the exit triangle ΔABD. In this case, another triangle (other than ΔABD) from the current tetrahedron would be selected as the base triangle for the next tetrahedron unit.

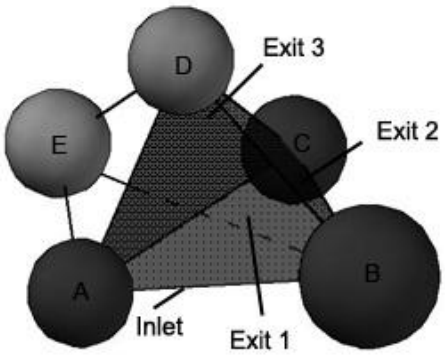

Fig. 3.7. An example which requires reselecting the exit triangle.

In the second case, a particle penetrated into the exit triangle, causing the flow area (calculated by Eq. 3.23) to be negative (ΔACD in Fig. 3.8). In this case, another particle would be selected to construct a new tetrahedron unit.

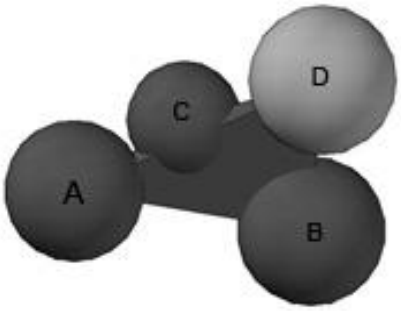

Fig. 3.8. An example of pore space larger than a particle, resulting in an unstable tetrahedron.

3.4.2 **Predicting tortuosity of airflow paths**

The tortuosity was calculated as the ratio of the actual length of flow path to the straight distance between the air entry and exit. As shown in Fig. 3.9, C_1, C_2, C_3, ..., C_n were the centroids of the base triangles of all tetrahedron units along an airflow path, which was constructed as lines connecting the centroids (C_1, C2, C_3…, C_n) of base triangles in all tetrahedron units (Fig. 3.9). The actual length of flow path was calculated as the summation of the line segments (local paths) ($C_1C_2 + C_2C_3 + \ldots\ldots + C_{n-1}C_n$). The bed depth was considered as

the straight length (L_0).

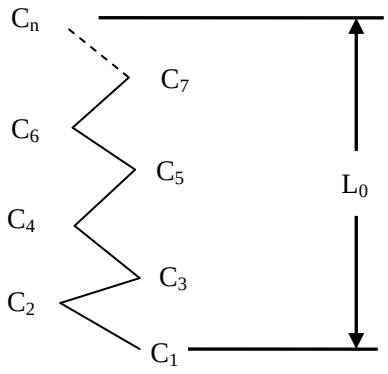

Fig. 3.9. Schematics of local airflow paths.

However, connecting the centroids (C_1, C_2, C_3…, C_n) of base triangles in all tetrahedron units to form an (global) airflow path resulted in sharp turns between two adjacent local paths (Fig. 3.9). Given that flowing air cannot make sharp turns, an airflow path should not have sharp turns. Therefore, the sharp angles were replaced by an arc to "smooth" the airflow path (Fig. 3.10), as recommended by Sobieski et al. (2012). Specifically, a local path was divided into two segments of length $\frac{a_i}{2} + \frac{b_i}{2}$ and the angle ω_i was determined as (Fig. 3.10):

$$\cos\omega_i = \frac{a_i^2 + b_i^2 - c_i^2}{2 \times a_i \times b_i} \tag{3.25}$$

where

i = the current point of path.

a_i, b_i, c_i = length of the sides of the triangle formed by three neighboring points of the path, respectively.

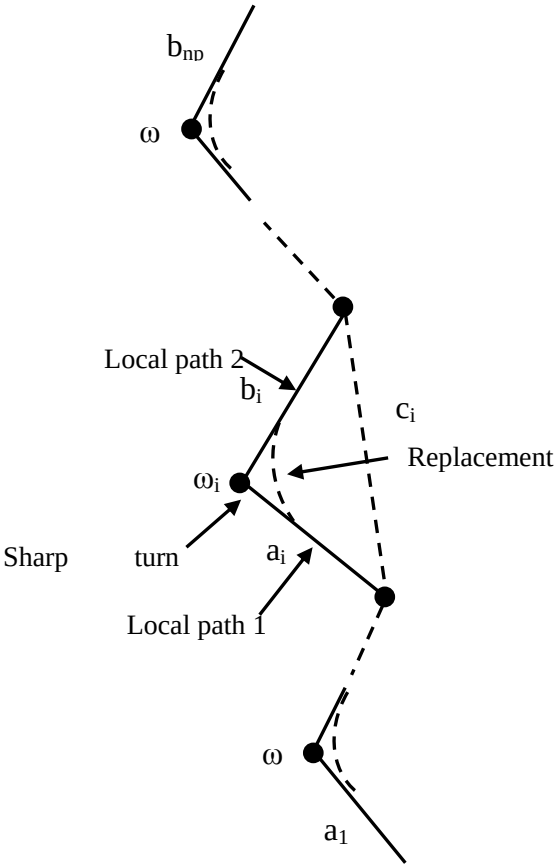

Fig. 3.10. Schematic representation of smoothing the airflow path by replacing the sharp turning angle with an arc (Sobieski et al. 2012).

Replacing sharp angles with arcs reduced the total length of flow path. A length correction factor ω_i^{cor} was calculated as follows (Sobieski et al. 2012):

$$\omega_i^{cor} = \frac{\exp(\omega_a(\omega_i - \omega_b))}{1+\exp(\omega_a(\omega_i - \omega_b))} \tag{3.26}$$

where

ω_i = the sharp angle between two adjacent local paths

ω_a, ω_b = coefficients. The values of ω_a and ω_b must satisfy $\omega_i^{cor} = 1$ for $\omega_i = 180$ and 0 for $\omega_i = 0$. In Sobieski et al.'s (2012) research ω_b was assumed to 90, which corresponds to a straight angle; $\omega_a = 0.1$ was selected used to calculate the correction coefficient in our research.

Once the length correction factor was determined, the "smoothed" path length was

calculated as follows (Sobieski et al. 2012):

$$L_p{}^{cor} = \frac{1}{2}\left(a_1 + b_{n_p}\right) + \sum_2^{n_p-1}\frac{1}{2}(a_i + b_i)\omega_i{}^{cor} \quad (3.27)$$

where

$L_p{}^{cor}$= length of path after smoothing

a_1 = the first section of the path

b_{np} = the last section of the path

n_p = number of connecting point of the path

The tortuoisty of airflow path was calculated as the ratio of the "smoothed" path length to the bed depth.

3.5 Pore-scale fluid flow models for predicting airflow resistance through grain bulks

3.5.1 Branched path model

Based on the DEM simulations of the pore structure of the grain bed, each tetrahedron unit had one air inlet and three outlets. Therefore, air flowed into each tetrahedron unit from an inlet (the main tube) and branched into three outlets (the branch tubes)(Fig. 3.11). The length of the main tube (l_0) was calculated as the distance from the centriod of the inlet triangle (C_0) to the centroid of the tetrahedron (C_t), the lengths of three branch tubes (l_1, l_2, l_3) were calculated as the distance from the centroid of the tetrahedron (C_t) to the centroids of three outlet triangles (C_1, C_2, C_3), respectively. Angles θ_1, θ_2, θ_3 are the branching angles from the main flow to the three branched flows.

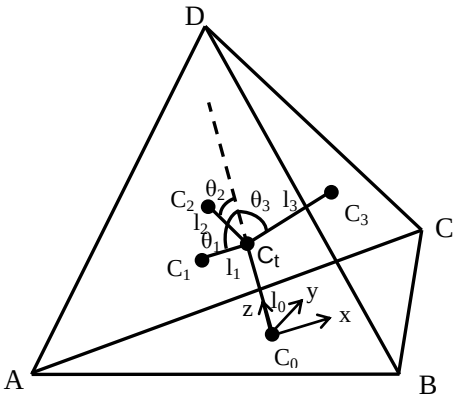

Fig. 3.11. The definition of branched flow model for airflow through each tetrahedron unit.

When a flow is divided into branches, the introduction of new dividing surfaces makes the flow velocity profile highly skewed, and the pressure or energy loss increases much more compared with the parabolic velocity profile in straight flow channels. Details of flow transition in the region of a tube branch are very complicated, and the characteristics of pressure loss in a tube branch are not well formulated yet even in laminar flow conditions (Lee et al. 2007). The approach used in this research followed a framework proposed by Lee et al. (2007) for determining pressure drops due to branching in airflow through the human bronchial tree. Specifically, the total pressure drop through a branching region was considered as the pressure drop in the main flow section (mother tube) plus pressure drops due to branching (daughter tubes). Following this framework, it was proposed in this thesis that the total pressure drop through in a tetrahedron unit could be written as the sum of the pressure drop of airflow through a straight inlet section (ΔP_S) (shown as C_0-C_t in Fig. 3.12) and the pressure drop in branching zone (ΔP_{b1}, ΔP_{b2}, or ΔP_{b3}, corresponding to C_t-C_1, C_t-C_2 or C_t-C_3 in Fig. 3.12), which was mathematically expressed as:

$$\Delta P = \Delta P_S + \Delta P_{b1,2 \text{ or } 3} \tag{3.28}$$

where

ΔP = the total pressure drop of airflow through a tetrahedron unit (Pa)

ΔP_S = the pressure drop of airflow through the inlet (straight) section (mother tube) (Pa)

$\Delta P_{b1,2\ or\ 3}$ = the pressure drop due to branching (daughter tubes)(Pa)

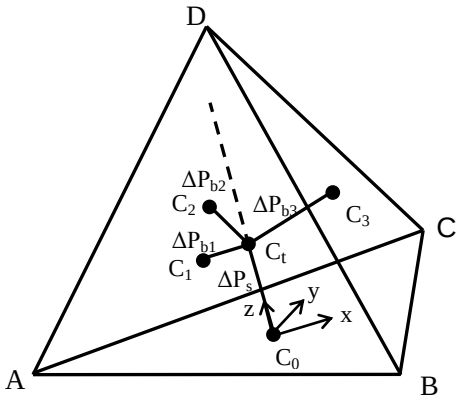

Fig. 3.12. Illustration of the total pressure drop calculation.

The flow rates considered in this research was very low (0.25 L s^{-1}) and the Reynolds number was calculated to be 34. Fluid flow through a packed bed with Reynolds number less than 10 is considered as laminar flow. The airflow in our research could be considered as laminar flow with inertial effects. The pressure drop for a fully developed laminar flow in the straight section was calculated by the Hagen-Poiseuille formula in terms of Darcy friction factor (Brown 2002):

$$\Delta P_s = f_D \times \frac{L}{D} \times \frac{\rho {v_0}^2}{2} \qquad (3.30)$$

f_D = Darcy friction factor (a dimensionless coefficient)

L = length of the tube (m)

D = hydraulic diameter of the tube (m)

V_0 = average velocity of the fluid flow, equal to the volumetric flow rate per unit cross-sectional wetted area (m s^{-1})

The Darcy friction factor can be calculated from the Reynolds number as follows (Lee et

al. 2007):

$$f_D = \frac{F_i}{R_{ei}} \quad (3.31)$$

R_{ei} = Reynolds number

F_i = proportional coefficient

The proportional coefficient was estimated to be 64 for laminar flow (Re<1000) in a straight tube (Hagen-Poiseuille) (Lee, et al. 2007). Therefore, the pressure drop for the straight section was determined by Eq 3.32:

$$\Delta P_S = f_D \cdot \frac{L_0}{D_0} \cdot \frac{\rho {V_0}^2}{2} \quad (3.32)$$

$$f_D = \frac{64}{R_e} \quad (3.33)$$

$$R_e = \frac{\rho D_0 V_0}{\mu} \quad (3.34)$$

$$V_0 = \frac{4Q_0}{\pi {D_0}^2} \quad (3.35)$$

where

L_0 = length of the mother tube (m)

D_0 = diameter of the mother tube (m)

V_0 = velocity of airflow in the mother tube (m s^{-1})

Q_0 = volumetric flow rate in the mother tube (m^3 s^{-1})

Lee et al. (2007) also proposed a method to calculate the pressure drops due to branching. Specifically, the pressure drop at a branch was determined by adding a multiplier function to the equation for the straight tube as follows:

$$\Delta P_{bi} = f(\theta_i) \cdot f_D \cdot \frac{L_i}{D_i} \cdot \frac{\rho {V_i}^2}{2}$$

i = 1, 2, 3, (3.36)

$$f_D = \frac{2100}{R_e} \tag{3.37}$$

$$V_i = Q_0 \cdot \frac{\pi {D_i}^2/4}{\sum_{i=1,2,3} \pi {D_i}^2/4} \cdot (\pi {D_i}^2/4)^{-1} \tag{3.38}$$

where

L_i = lengths of daughter tubes (m), i =1, 2, 3

D_i = diameters of daughter tubes (m), i =1, 2, 3

V_i = airflow velocity in daughter tubes (m s^{-1}), i =1, 2, 3

$f(\theta_i)$ = multiplier function

θ_i = branching angle (degree)

Eq. 3.38 shows that the assumption of the flow rate in a daughter tube being proportional to its cross-sectional area led to an equal flow velocity in all three daughter tubes. This velocity was simply the total flow rate divided by the sum of cross-sectional areas of the three daughter tubes.

The multiplier function $f(\theta_i)$ described the effect of branching angle on pressure drop in the branching region, with a value of 0 for $\theta_i = 0$ (no branching, or a straight tube). Lee et al. (2007) proposed a monotonically increasing function for $f(\theta_i)$ in the form of:

$$f(\theta_i) = a - b\cos\theta_i \tag{3.39}$$

where a and b are two empirical constants. Based on the work of Jamison & Villemonte (1971), Lee et al. (2007) concluded that the maximum value of $f(\theta_i)$ lied between 2 and 3 because the pressure drop for a sharp branching of a rigid circular tube was almost three (3) times as high as that in a straight tube, but it became smaller for a smooth branching at the same branching angle. Based on this conclusion, Lee et al. (2008) presented and verified two empirical equations for $f(\theta_i)$. The first one $f(\theta_i) = 3\text{-}2\cos\theta_i$ was suggested if the maximum pressure drop

due to branching at 90 °was three times as high as that at 0 °, and the second one $f(\theta_i) = 2\text{-}\cos\theta_i$ was proper if the pressure drop was twice as high at 90 ° as that at 0°. These two multiplier functions were denoted as MF×3 and MF×2, respectively in the following sections of this thesis.

The size of flow channels (tube diameters) was required in calculating pressure drops. However, the available cross-sectional area (ACSA) for air to flow through a tetrahedron was variable, as shown in a typical tetrahedron unit in Fig. 3.13. Taking the inlet ΔABC as an example, the maximum possible ACSA was the area of triangle ABC, while the minimum ACSA was calculated as the area of triangle ABC less the area occupied by the three particles at the vertices (Fig. 3.13b). The maximum and minimum ACSA's for other three faces (triangles in the tetrahedron) could be determined in the same fashion. Given that the variations in ACSA along the flow path were too complicated to be theoretically quantified, the minimum and maximum ACSAs were used to establish the upper and lower bounds of pressure drop, respectively, while the average of the minimum and maximum ACSAs was calculated to predict the average pressure drop through a tetrahedron unit.

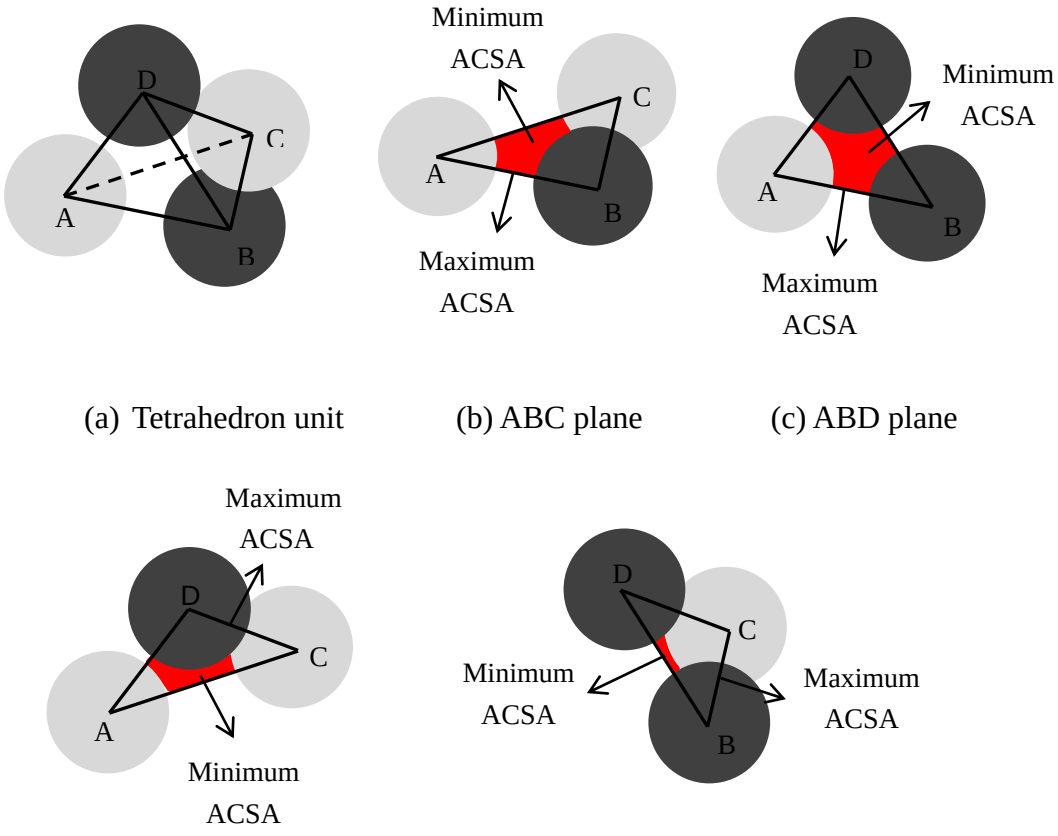

(a) Tetrahedron unit (b) ABC plane (c) ABD plane

(d) ACD plane (e) BCD plane

Fig. 3.13. Illustration of three cases of cross sectional area.

3.5.2 **Pore-scale network model**

Network modeling is a useful tool to study the flow and transport phenomenon in porous media at the pore scale level. It provides a link between microscopic properties of porous media and transport behavior at the macroscopic level. In network models, the porous media is considered as a series of interconnected pores and pore throats. Fluid transport is modeled by imposing conservation equations at each pore in the network. Applying the boundary conditions, numerical solutions of overall pressure within the network are obtained (Thompson and Fogler 1997; Thompson2002). The process of network modeling consists of three steps: 1).

simulation of the packed bed structure; 2) Delaunay tessellation; 3) solution of the pressure at the pore level and solution of the overall pressure.

3.5.2.1 **Simulation of grain bed**

The PFC^{3D} DEM model was used to simulate the cylindrical bin described in Section 3.1 (Fig. 3.1). The details of PFC^{3D} simulation were the same as presented in Section 3.1. The position (x, y and z coordinates) and the radius of every grain kernel (sphere) determined in the simulation were used to carry out the Delaunay tessellation.

3.5.2.2 **Delaunay tessellation**

The Delaunay tessellation was used to divide spheres (grain kernels) into tetrahedrons, each consisting of the nearest four spheres to each other (Fig. 3.14) (Thompson and Fogler 1997). Specifically, each Delaunay tetrahedron was considered as a pore unit and the centers of spheres were the four vertices of the Delaunay tessellation. The pore space was defined as the central void with the four constrictions connecting the void to the remaining pore space and the pore throat was defined as the area projected onto a tetrahedron's face (Fig. 3.15). Air was assumed to enter the tetrahedron unit through any four constrictions at tetrahedron's faces. Because the tetrahedron vertices were at sphere centers, the void projected onto each of the four faces was necessarily the smallest constriction that was encountered when traversing a passage into the central pore.

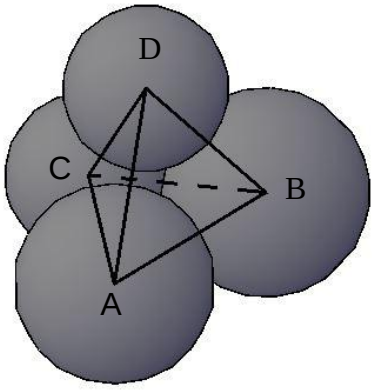

Fig. 3.14. A Delaunay tetrahedron representing grain mass in the bin.

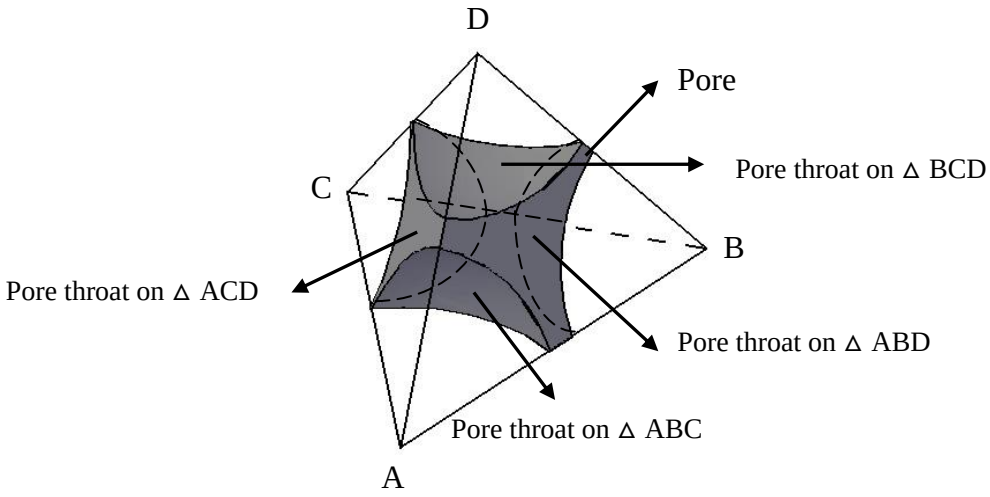

Fig. 3.15. Illustration of the pore and pore throat of a Delaunay tessellation.

The Delaunay tetrahedron requires that the circumsphere defined by four vertices encompassed no other sphere centers from the packed bed (Bowyer 1981; Wastson 1981). The algorithm of Delaunay tessellation of the packed bed was performed in Matlab (R2013b, Mathworks Inc., USA). The process of Delaunay tessellation was shown in Fig. 3.16. First, the dataset of coordinates of particles generated in the DEM model of grain bed was imported to the Matlab algorithm. Then the DT=delaunayTriangluation (x, y, z) procedure was used to

create a 3D Delaunay triangulation in matrix format from the coordinates of points (centers of particles) in the column vectors x, y, and z. The criterion was that no spheres contained in the interior of the circumsphere associated with each tetrahedron. After the tessellation was completed, the pore network (connectivity) within the grain bed was obtained. The numbers of points (centers of particles) for constructing the Delaunay tessellation (number of tetrahedron × 4) and the neighboring tetrahedrons (number of tetrahedron × 4) were determined. The procedure is outlined in Fig. 3.16. The boundary of the Delaunay tessellation was considered as the noncounducting edges which lied in a few layers of spheres inside the edge of the packed bed (Thompson and Fogler 1997).

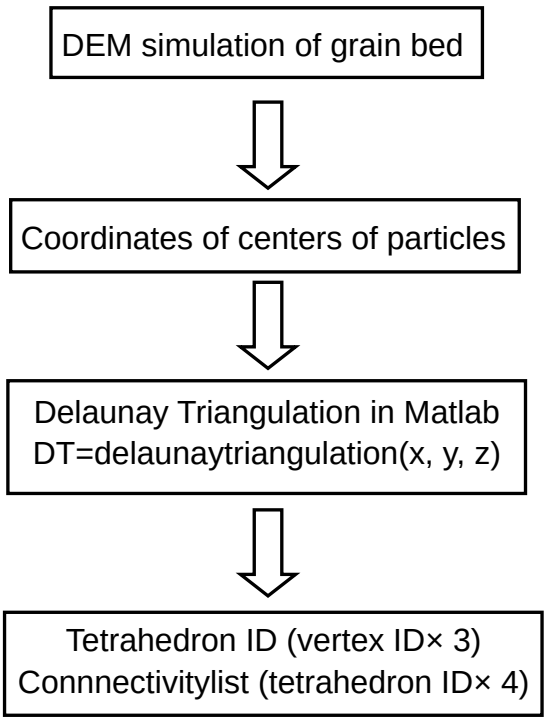

Fig. 3.16. The process of Delaunay tessellation.

3.5.2.3 **Pressure drop at pore level**

To model flow through the network of packed bed, flow at the pore level was considered first and then scaled up to the global network. Specifically, the balance equation for the net volumetric flow rate in each interior tetrahedron was applied as follows (Thompson and Fogler 1997):

$$q_{net} = 0 = \sum_{j=1,4}[(p_j - p_i)g_{i,j}] \quad (3.39)$$

where

q_{net} = net volumetric flow rate in each interior tetrahedron (m s^{-3})

i = the *ith* interior tetrahedron (pores)

j = four neighboring pores

p_i = pressure in each pore (Pa)

p_j = pressure in four neighboring pores (Pa)

$g_{i,j}$ = fluid conductivity

The fluid conductivity $g_{i,j}$ is equal to the ratio of volumetric flow rate and pressure drop across a pore throat (Thompson and Fogler 1997). The numerical values for the throat conductivities ($g_{i,j}$) between any two pores were required to solve the fluid transport equation at each pore. The throat conductivity depends on the throat geometry as well as fluid viscosity. The shape of throat cross sections in a tetrahedron unit were highly irregular and was defined by the dimensions of the triangular faces and the radii of the bounding spheres (Fig. 3.17). There were four types of pore throat shapes as shown in Fig. 3.17. Type (a): three particles did not touch; Type (b): two particles were in contact but the third one did not touch with either of them; Type (c): two particles were in touch and the third one in contact with one of other two;

and Type (d): three particles were in touch with each other. Because the bounding surfaces of a pore throat were formed by three spheres, the area of cross sections (thus the conductivity) decreased with the increase in the radius of three spheres (the cross sections of pore throat converged and diverged in the direction perpendicular to the paper, as shown in Fig. 3.17).

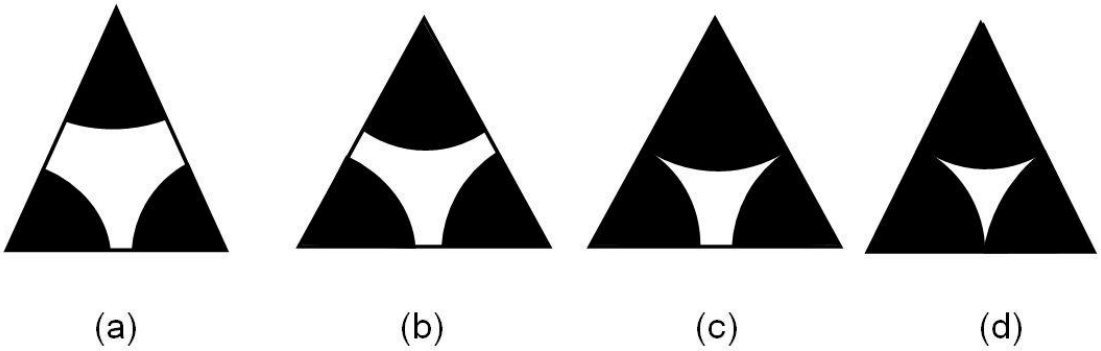

Fig. 3.17. Four types of throat geometries on a triangle face (Thompson and Fogler 1997).

Thompson and Fogler (1997) developed a relationship between flow rate and pressure drop for parallel and incompressible flow through an arbitrary shaped duct by dedimensionlizing Navier-Stoke's equation to a dimensionless form of Poisson's equation solved using the finite-element method. The dimensionless flow rate was obtained by integrating the dimensionless velocity $u^* = f(x^*, y^*)$

$$\frac{\partial^2 u^*}{\partial {x^*}^2} + \frac{\partial^2 u^*}{\partial {y^*}^2} = 1 \tag{3.40}$$

The conductivity for a pore throat was determined as follows:

$$g = \frac{Q}{\Delta P} = \frac{Q^* {r_1}^4}{\mu L} \tag{3.41}$$

where

Q = flow rate ($m\ s^{-3}$)

Q^* = dimensionless flow rate

ΔP = pressure drop (Pa)

r_1 = average radius of the bounding spheres (m)

μ = viscosity of air (Pa s)

L= pore length, which was assumed as the average diameter of three bounding spheres

Q* is the dimensionless flow rate, which was determined by integrating the dimensionless velocity over the cross sectional area using Eq.3.42 (Thompson and Fogler 1997).

$$Q^* = \int_A u^* \, dx^* dy^* \qquad (3.42)$$

In this work, an algorithm was developed in Matlab to calculate the fluid conductivity $g_{i,j}$. Combining for the Eqs. 3.39 and 3.41 for every tetrahedron unit in the grain bed resulted in a set of linear equations for p_i (i = 1 to n, where n is the total number of interior tetrahedron units in the grain bed). The boundary condition for solving these simultaneous equations was to specify the net volumetric flow rate along with pressure on the inlet faces of the network. An additional constraining equation was added to the matrix that represents the sum over all inlet pores (Thompson and Fogler 1997). The linear matrix equations were solved to obtain the solution of the pressure in each interior tetrahedron by using the Gauss-Seidel method with overrelaxation in Matlab,

3.6 Validation experiment

An experiment was conducted to measure the relationship between pressure drop and airflow rates through a grain bulk to validate the simulation models for airflow resistance. The experimental apparatus consisted of an air pump, a cylindrical plenum and a test grain bin (Fig. 3.18). A cylindrical bin 0.275 m high (H) and 0.154 m in diameter (D), made of 7 mm thick PVC, was designed and constructed to conduct the experiment. A cylinder of the same diameter (0.32 m H × 0.15 m D) was used as the plenum under the test section to produce

uniform pressure at the bottom of test bin. Grain (soybeans) was filled in the bin using a funnel placed 0.025 m above the bin. The air was supplied by an air pump (Sidewinder A/C WEB-62055 C, Bestway, USA) to the plenum and then to the grain bed through a perforated floor with 1 mm diameter holes spaced 1 cm apart. To enhance the uniformity of airflow through the grain bed, two additional perforated floors were used as flow strainers at 0.09 m and 0.18 m from the bottom of the grain bed. The flow rate was measured by a gas flow calibrator (Model M-30, A. P. Buck, Inc. USA) with a range of 0.1 to 30 LPM and accuracy of ±0.5%. A differential pressure transmitter (Model 332, Furness Controls Ltd, UK) with the range of 0 to 50 Pa and accuracy of f ±0.25% was used to measure the pressure drop at different depths of the grain bed (Figs.3.18 and 3.19).

In each test, the pressure at point 0 (plenum) was measured to represent the pressure at the inlet of the grain bed. The pressure differences between point 0 and 1, 1 and 2, 2 and 3 were measured, respectively, to investigate pressure drops with the bed depth (Figs. 3.18 and 3.19). To test if there was variation in pressure drop in the radial direction of the grain bed, the pressure difference between Location 2A and atmosphere and Location 2B and atmosphere were also measured and compared.

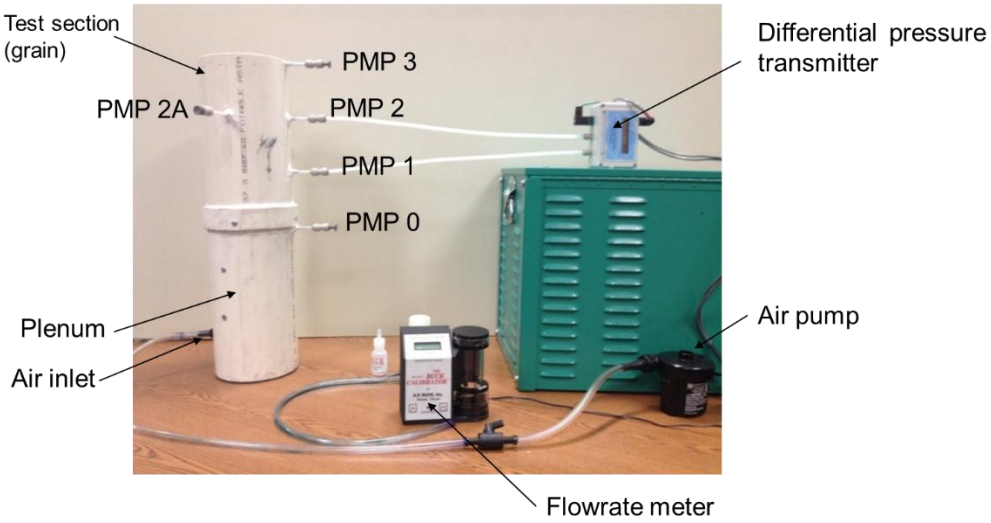

Fig. 3.18. The experiment apparatus for measuring the pressure drops of airflow through the test grain bin.

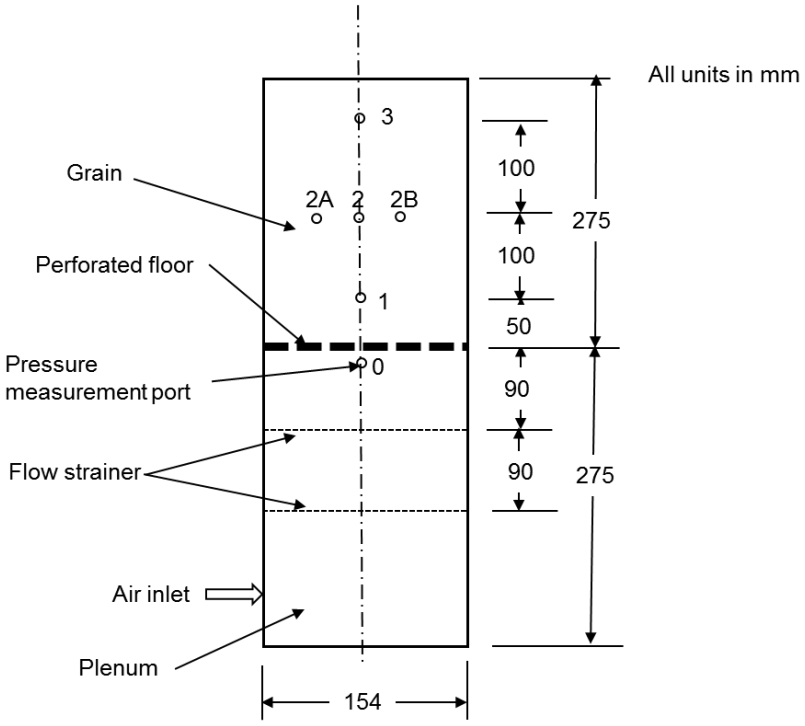

Fig. 3.19. Schematics of the test grain bin for airflow resistance measurement.

4 Results and Discussion

4.1 Simulated pore structures of grain bed and airflow paths

4.1.1 Simulated grain beds

The simulated rectangular and cylindrical bins are illustrated in Fig. 4.1a and 4.1b, respectively. A sample of numerical results (particle coordinates and radii) is shown in Appendix A. For the rectangular bin, the DEM model generated a grain bed consisting of 5,146 spherical particles with diameters randomly distributed between 5.5 mm to 7.5 mm. For the cylindrical bin, the DEM model generated a porous bed consisting of 18,188 particles. To verify if the simulated beds properly represented the actual grain beds, the numbers of particles were compared between simulated and actual beds for the cylindrical bin. Based on the measured weight and the volume of the grain bed, the total number of particles in the bin was estimated to be 18,498. In other words, the total number of particles in the simulation was 1.7% lower than the measured value. It should be noted that estimation of the total number of particles in the bin was based on the assumption that all kernels were spherical and had an average diameter of 6.5 mm. However, the measured geometric mean diameter was 6.6 mm. Using this measured diameter of 6.6 mm, the total number of particles in the bin was estimated to be 17,670, which was 2.9% lower than the simulated value. Also, the simulated global (overall) porosity was 0.408, which was in good agreement with the measured value of 0.398±0.006 (±standard deviation).

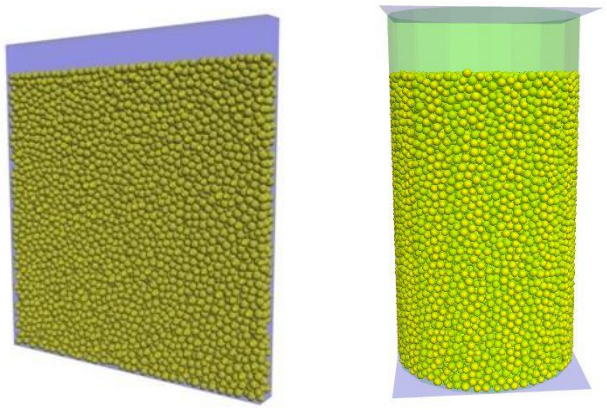

(a) (b)

Fig. 4.1. Simulated grain beds by PFC^{3D} DEM model. (a) rectangular bin, (b) cylindrical bin.

To describe the structure of porous media, particle size distribution of the simulated porous beds were analyzed. Taking the rectangular bin as an example, the distribution of particle size (diameter) generated from the simulated porous bed was shown in Fig. 4.2. It can be seen that the particle size distribution was fairly uniform in the 5.5 to 7.5 mm range. There were 2.5% of particles with diameters outside that range. This was because there was not enough space in the bin to accommodate all the large particles during the expansion to achieve the prescribed porosity (as discussed in Section 3.1)

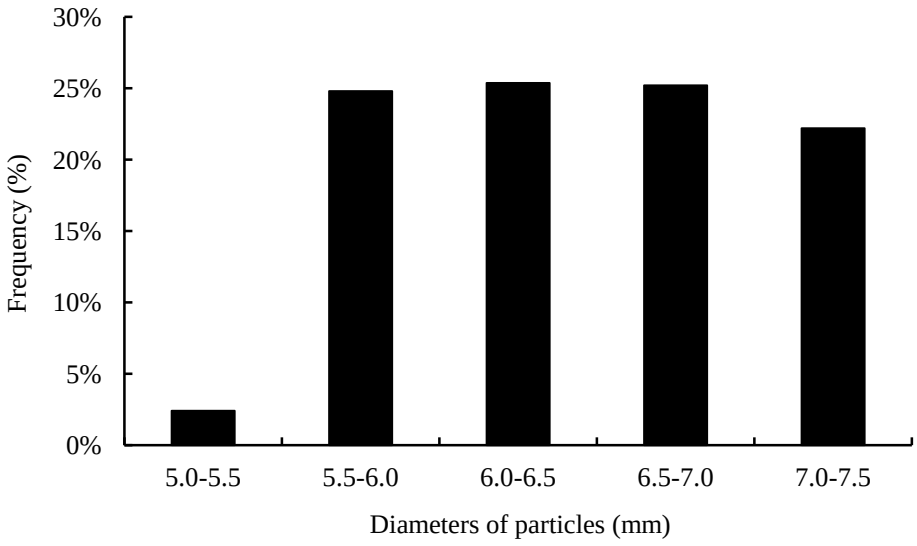

Fig. 4.2. The frequency distribution of particle size.

Another important parameter that is often used to describe the structure of granular materials is the coordination number. The distribution of coordination number for rectangular bin model was determined using the DEM simulation results. To minimize the effect of walls, the packing bed was cut off (x[-0.05,0.05], y[-0.05,0.05], z[0.02, 0.23]) for structure analysis. The frequency of coordination numbers of selected structure for different vibration amplitude and frequency was shown in Fig. 4.3. The results were obtained using a cutoff distance $1.05d_{max}$ (0.008). That means a contact between two particles was counted if the distance between them was less than 1.05_{max}. It appeared that the distribution of coordination number was close to a normal distribution, with a peak frequency at 9. An (2012) observed that the peak values were 7 for the amorphous state with a packing density of 0.64 and 12 for the crystalline state with a packing density of 0.74.

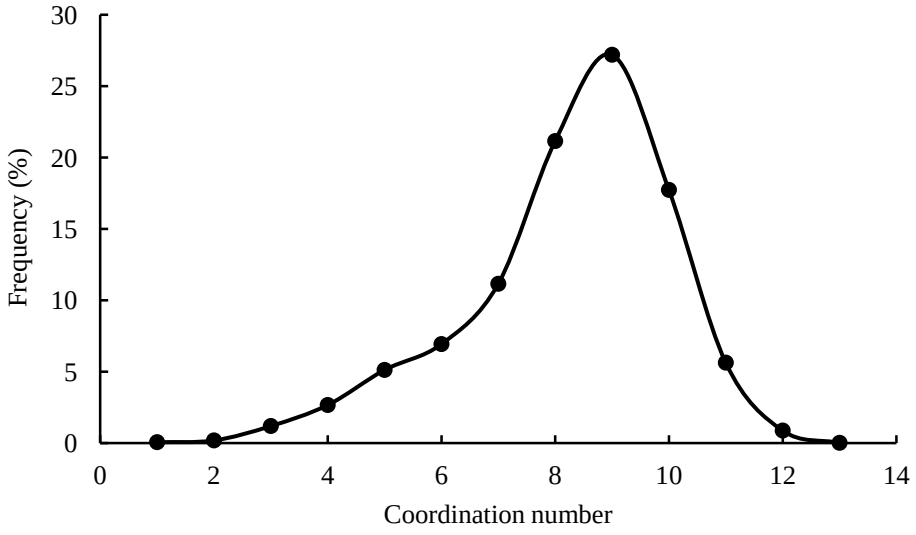

Fig. 4.3. Distribution of coordination number in the simulated grain bed for rectangular bed.

4.1.2 **Simulated airflow paths**

Three different air entrance points (AEP) ((0.02, 0, 0); (-0.07, 0, 0); (0.09, 0, 0)) located at

the bottom of the grain bed were randomly selected to construct the flow paths as examples to demonstrate the characteristics of airflow paths through the grain bed. It should be noted that the selection of the three AEP's was random, but with one constraint – the AEP should not be too close to the vertical walls as recommended by Sobieski (2012) to avoid the boundary effect. The simulated airflow paths were tortuous and of random shape (in terms of path length and width, and local turns), as expected (Table 3, Figs. 4.4 & 4.5).

Table 4.1 Summary of calculated flow path parameters of three widest and three narrowest airflow paths.

	AEP location (x, y, z)(m)	Path length L_e (m)		Path width W (mm)		No. of tetrahedron units	
		Widest	Narrowest	Widest	Narrowest	Widest	Narrowest
AEP1	(0.02,0,0)	0.365	0.390	2.91	1.99	152	148
AEP2	(-0.07,0,0)	0.365	0.376	2.83	1.85	160	142
AEP3	(0.09,0,0)	0.385	0.401	2.73	2.00	162	154

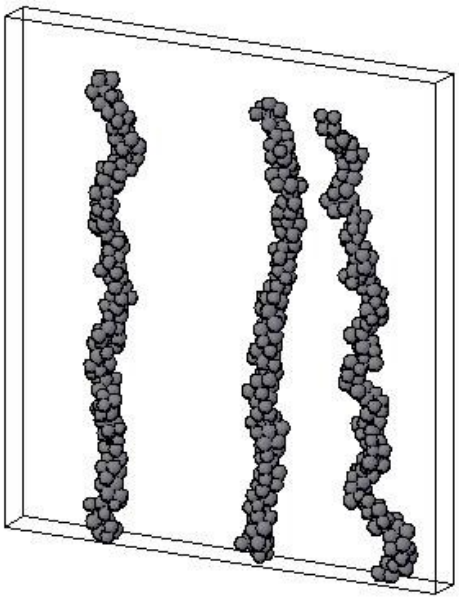

(a)

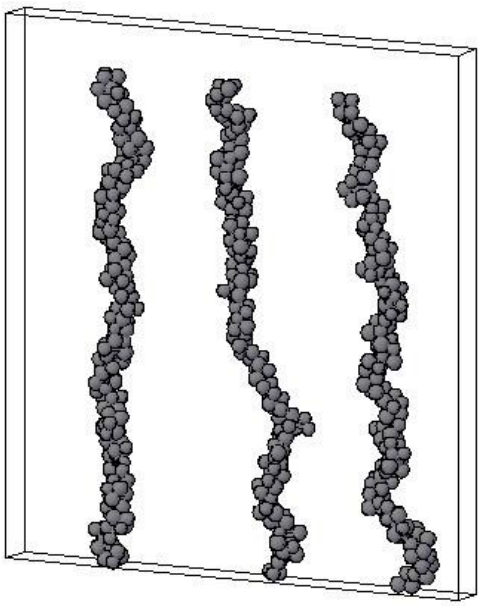

(b)

Fig. 4.4 Simulated airflow paths, as represented by the associated tetrahedron units. (a) three widest paths and (b) three narrowest paths.

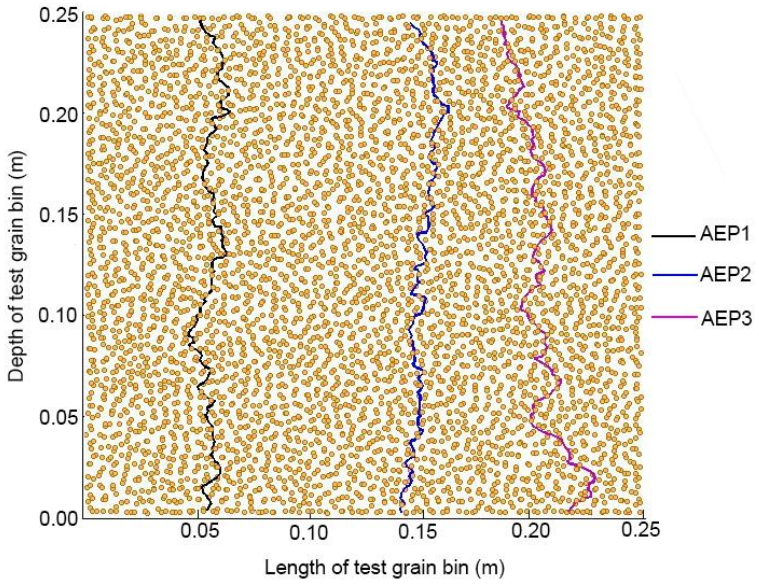

(a)

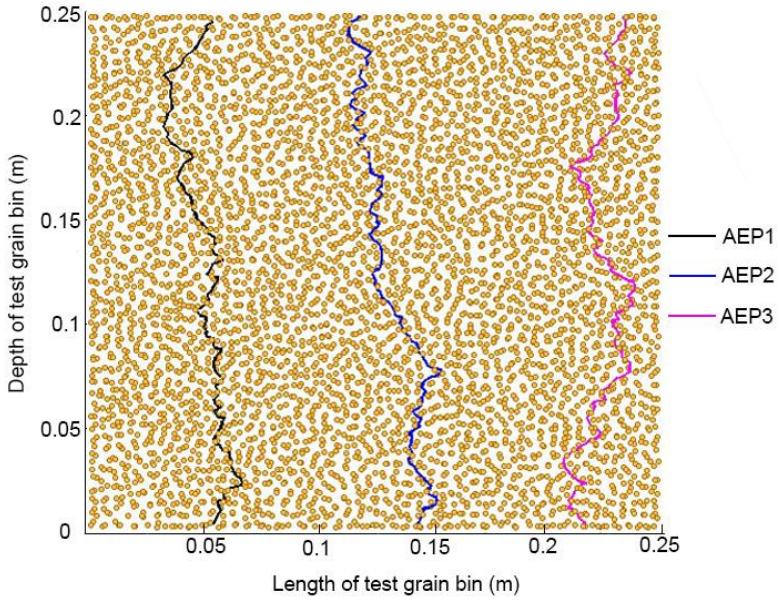

(b)

Fig. 4.5. Simulated airflow paths in two-dimension. (a) three widest paths and (b) three narrowest paths.

Of the six simulated paths, the longest path was 0.401 m and the shortest was 0.365 m, while the depth of bed was 0.25 m. The three narrowest paths appeared to deviate more from the entry point in comparison with the three widest paths (Fig. 4.5), which resulted in longer

local paths and less number of tetrahedrons for the narrowest paths (Table 4.1). It was apparent that different AEP's resulted in different flow paths. For example, the largest difference was 7% in path length and 8% in path width among the three randomly selected AEP's for the narrowest paths. This meant that air entering a grain bin at a particular point would follow a unique path and be subjected to specific resistance as it passed through the grain bed.

The flow path changed its direction within each and every tetrahedron unit (local turns) (Fig. 4.5). A few local turns were in the range of 80°-90°, while more in the range of 0°-10°.The distribution of local turning angles for three widest and three narrowest airflow paths are shown in Fig. 4.6. It can be observed that more than 50% of the local turning angles were smaller than 30°. There was no significant difference in the frequency distribution of local turning angles between the widest and the narrowest paths.

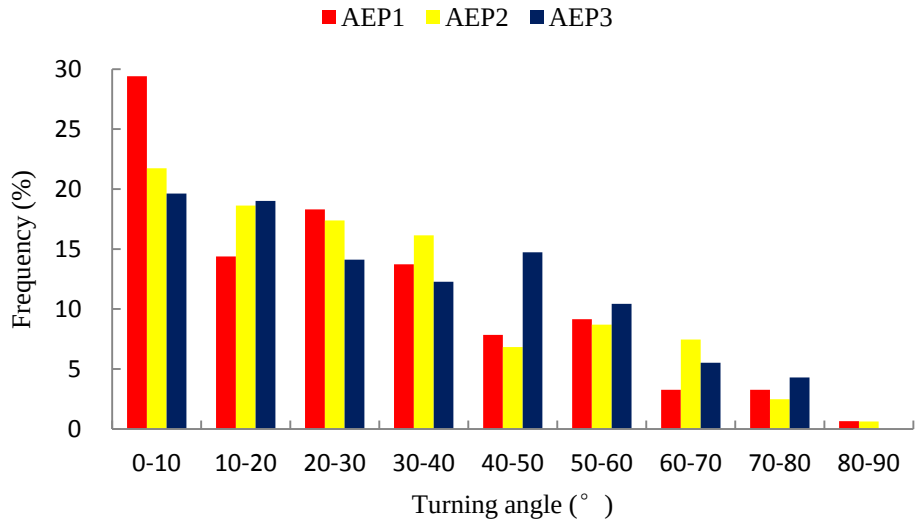

(a)

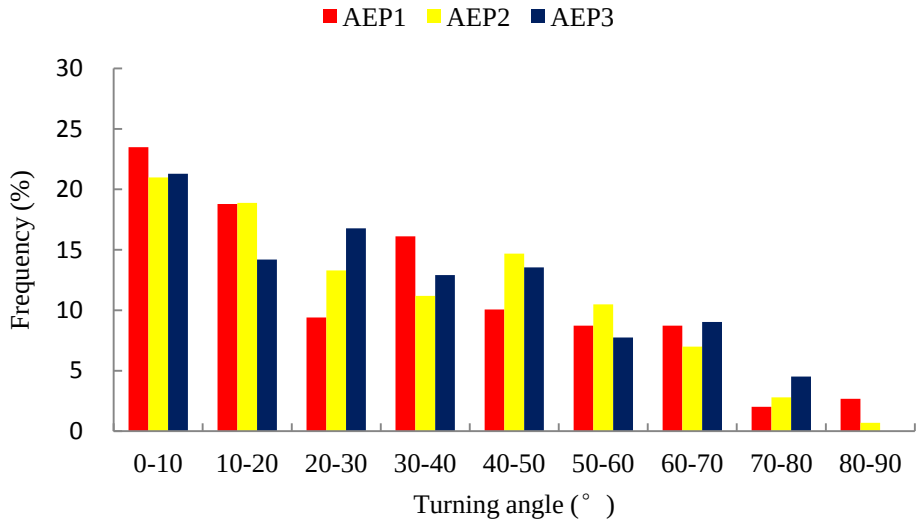

(b)

Fig. 4.6. The frequency distribution of local turning angles for (a) three widest paths, and (b) three narrowest paths.

The simulated path width varied from 1.85 to 2.91 mm (Table 4.1). The average path width of three widest airflow paths (2.91, 2.83, and 2.73 mm) were 45% bigger than that of three narrowest airflow paths (1.99, 1.85, and 2.00 mm). It was observed that the path width varied randomly along the path, ranging from 0.98 to 5.93 mm for three widest paths and 0.83 mm to 4.29 mm for three narrowest paths (Fig. 4.7). Most path widths were in the 2-3 mm

range for three widest airflow paths and 1-2 mm for three narrowest airflow paths (Fig. 4.8).

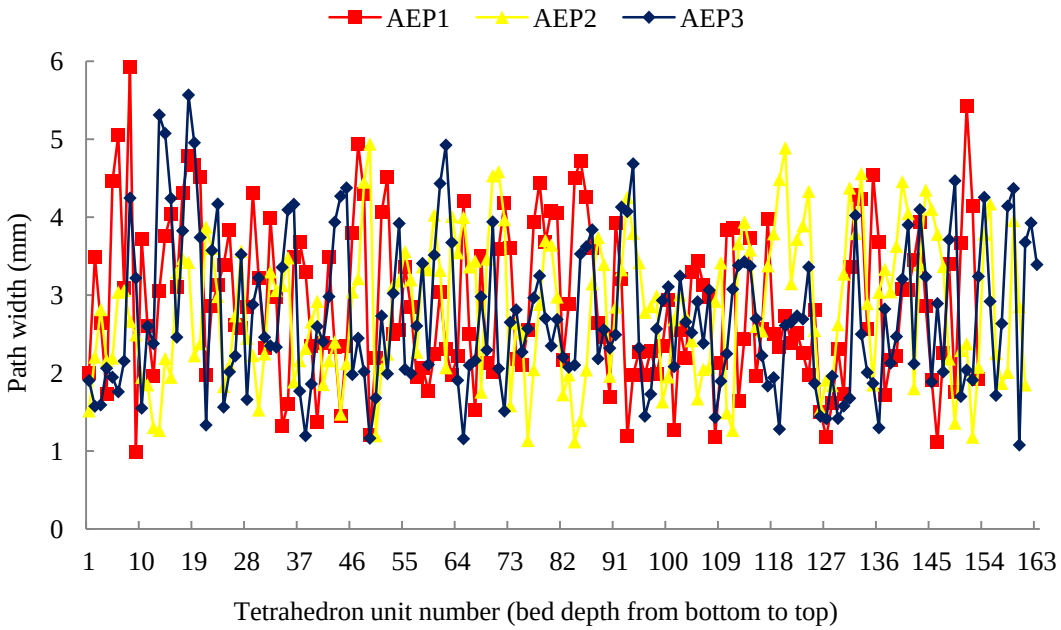

(a)

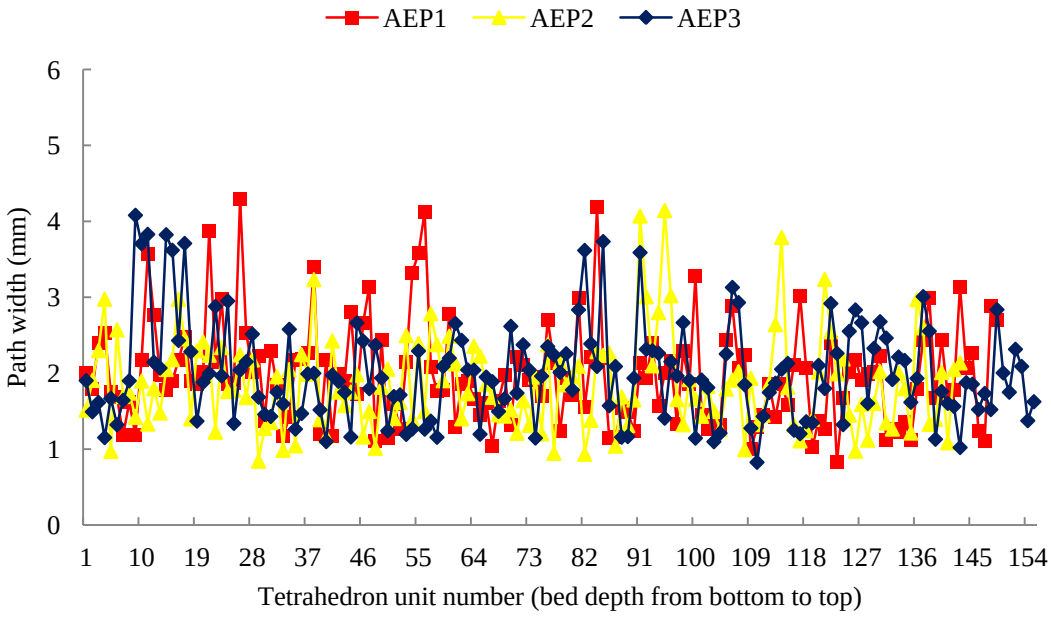

(b)

Fig. 4.7. The variation of the path width in the vertical direction for (a) three widest paths and (b) three narrowest paths.

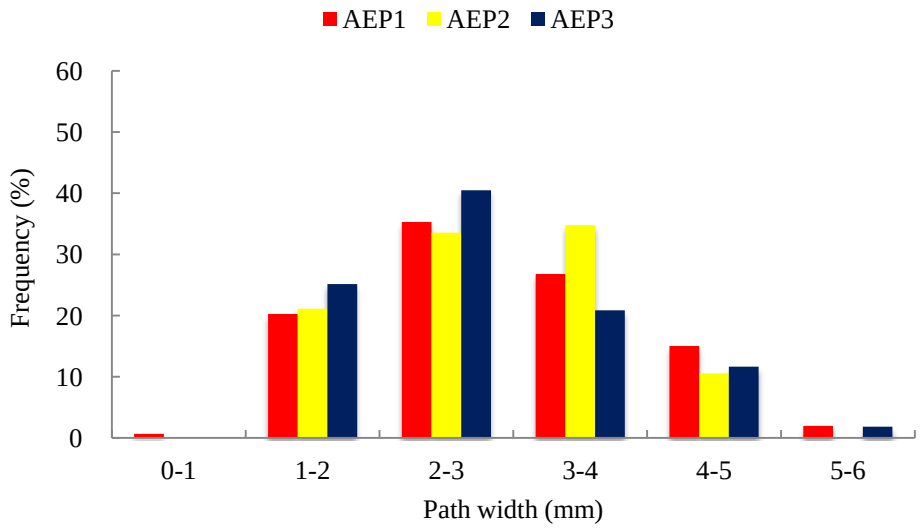

(a)

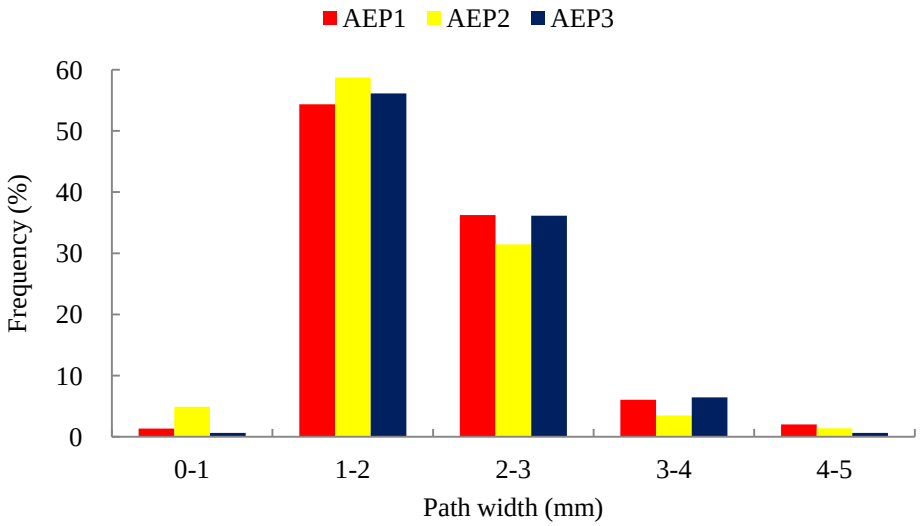

(b)

Fig. 4.8. Distribution of airflow path width for (a) three widest paths and (b) three narrowest paths.

The average simulated tortuosity was 1.39, which seems higher than those reported in the literature (Table 4.2). Yun et al. (2005) reported tortuosity values from 1.0 to 1.4 for porosities from 1.0 to 0.4. Neethirajan et al. (2006) used 2D CT images to construct the shortest flow path and obtained the averaged tortuosity to be 1.07. Based on the pore structures simulated by the

discrete element model, Sobieski (2012) obtained an average tortuosity of 1.14 for the shortest airflow path in porous beds. Using smoke to visualize airflow, Charles (2013) determined the average tortuosity was 1.17 with flow rate of 0.25 L s^{-1} for loosely packed grain and 1.20 for densely packed grain (soybeans). It should be noted that tortuosities predicted in this study were for the widest and narrowest flow paths, while most results reported in the literature are for the shortest path. Therefore, it was expected that the tortuosities in this study were higher than those reported in the literature.

Table 4.2. Simulated tortuosities for three widest and three narrowest airflow paths after smoothing.

AEP	Widest airflow path	Narrowest airflow path
AEP1	1.33	1.40
AEP2	1.39	1.34
AEP3	1.45	1.47
Average	1.39	1.40

4.1.3 **Comparison of pore structures between the vertical and horizontal directions**

The simulated flow paths in the horizontal direction were generally similar to those in the vertical direction (Fig. 4.9 and Table 4.3).

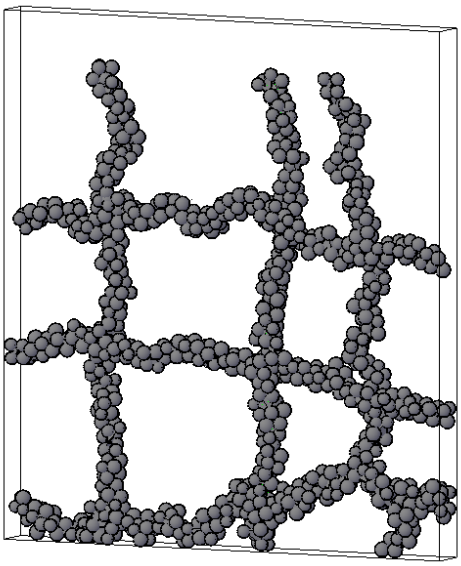

Fig. 4.9. Three widest airflow paths in the vertical direction and three widest airflow paths in the horizontal direction.

Table 4.3 Summary of calculated flow path parameters for three widest airflow paths in the vertical direction and in the horizontal direction.

Direction	AEP	Path length L_e (mm)	No. of tetrahedron units	Tortuosity
Vertical	AEP1	365	152	1.40
	AEP2	363	160	1.34
	AEP3	385	162	1.47
	Average	371	158	1.40
Horizontal	AEP4	355	153	1.34
	AEP5	363	154	1.40
	AEP6	390	159	1.40
	Average	369	155	1.38

The differences in the average path length and tortuosity between the vertical and horizontal directions were negligible (Table 4.3). These small differences might be attributed to the fact that the soybean kernels were simulated as spheres in the DEM model instead of elongated shape. Using elongated particles might have resulted in larger differences between

the vertical and horizontal directions as the packed bed of elongated particles may cause most grain kernels to lie with the long axis in the horizontal direction, resulting in more connected pores in the horizontal direction. The path width of three widest airflow paths in the horizontal direction is shown in Fig. 4.10. The most path width was 2-3 mm in the horizontal direction, which was also similar to the vertical direction. Specifically, the average path width of three widest paths in the horizontal direction (2.86, 2.63, 2.81 mm) was 2% smaller than the average path width of three widest airflow paths in the vertical direction (2.91, 2.83, and 2.73 mm).

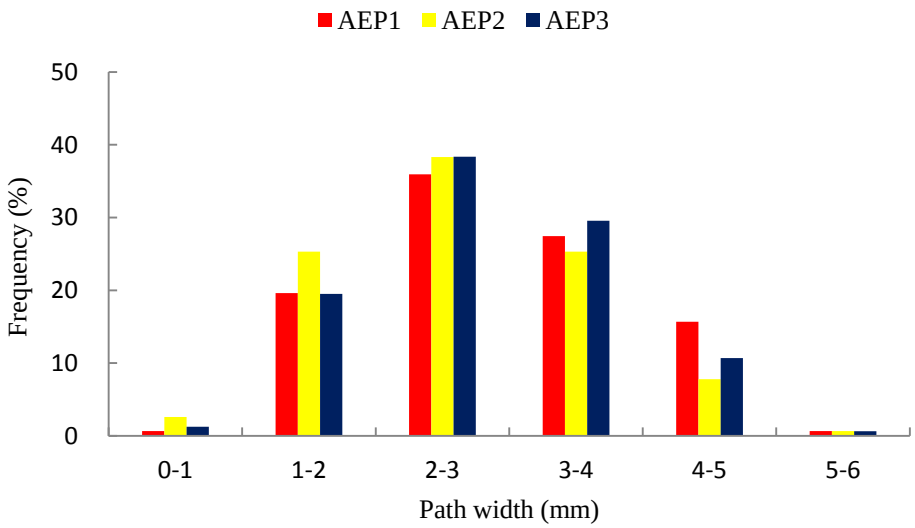

Fig. 4.10. Distribution of airflow path width for three widest paths in the horizontal direction.

4.1.4 Effects of vertical vibration on pore structure

4.1.4.1 Properties of simulated grain bed and comparison with experimental data.

Vertical vibration caused porosity to decrease in general. The simulated minimum porosity decreased from 0.401 to 0.379, whereas the measured value changed from

0.398±0.006 to 0.366±0.001 after vibration (at 1.0g intensity). The relative change (decrease) in porosity after vibration was 5.5% in simulations, which was lower than that in measurements (8.0%). The simulated porosity changes were within the range reported by Liu (2008): 0.7% to 6.1% reduction in porosity of soybean in a model bin after vibration.

The simulated local porosity, calculated from the PFC^{3D} built-in function in a small region within the porous bed, varied with the location. Specifically, the local porosity before vibration was 0.402, 0.395, 0.395, 0.393, and 0.389 at the five selected locations (B1-B5), respectively. The average of the five locations was close to the measured value (0.395 vs. 0.398). Local porosity also varied with both vibration duration and intensity, which is discussed in the next sections.

4.1.4.2 **Variation in porosity during vibration**

Fig. 4.11 shows typical curves of simulated local porosity during vibration. The minimum porosity was reached at about 9 s for all locations (all simulations were run for 16 s). The local fluctuations in porosity were apparent, and they were attributed to the cyclic nature of vibration which compressed and relaxed the porous material during each vibration cycle (An X.Z. et al., 2005). The magnitudes of these local fluctuations could be as high as 0.02 (e.g., from 0.37 to 0.39 in porosity). The overall trend was that local porosity decreased as vibration progressed, but not monotonically (large global fluctuations were apparent). Taking location B2 as an example, the porosity increased quickly from the initial level of 0.395 to 0.430 in 0.04 s, and then dropped to 0.370 at about 0.3 s. This observation did not agree with the result reported by An X.Z. et al. (2005). Based on discrete element simulations, they observed that packing

fraction (opposite to porosity) increased monotonically (with local fluctuations) with time of vibration. It should be noted that it was not clear if the porosity reported by An X.Z. et al. (2005) was the local or global porosity. Given that the pore structure in a porous bed varies from location to location, one would expect that local porosity varies with location. An X.Z. et al. (2005) observed that macro-pores (pores large enough to accommodate a particle) existed in loosely packed sphere assemblies. Therefore, high porosity could exist locally where a macro-pore exists. During vibration, particles re-arrange themselves and macro-pores would be destructed (An X.Z. et al. 2005). However, it was also possible that some macro-pores were created at an instant through particle re-arrangement during vibration, resulting in high local porosity. These instant macro-pores might not be stable and would be destructed quickly by vibration. During vibration, destruction and creation of macro-pores might occur repeatedly, resulting in fluctuations in porosity; however, more macro-pores would be destructed than created, leading to a general trend of decrease in local porosity, as well as gradual decrease in the global porosity. A similar pattern of fluctuations in local porosity were observed by Liu C. (2008) in his experiments to investigate the vibration effect on porosity of soybean. He used a high speed camera to record movements of soybean kernels in a transparent bin made of Plexiglas. Based on the recorded video images, he tracked three particles that formed a triangle and calculated the area of this triangle at different times during vibration. He considered that changes in the triangle area reflected changes in local porosity. At a vibration frequency of 25 Hz and amplitude of 0.4 mm, the relative change (the initial area of triangle was considered to be 100%) in the triangle area with time is shown in Fig. 4.12. It was apparent that the triangle

area (reflecting the local porosity) fluctuated during vibration, with an overall trend of decrease.

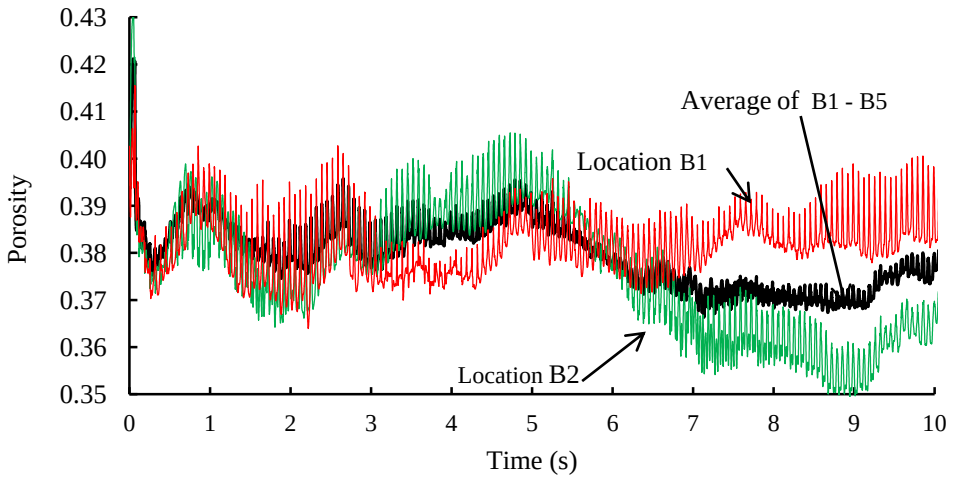

Fig. 4.11. Simulated local porosity during vibration at locations B1(0.06, 0, 0.119) and B2(0.06, 0.129), and the average porosity of all five locations for vibration intensity of 1.8g (15 Hz frequency and 2 mm amplitude).

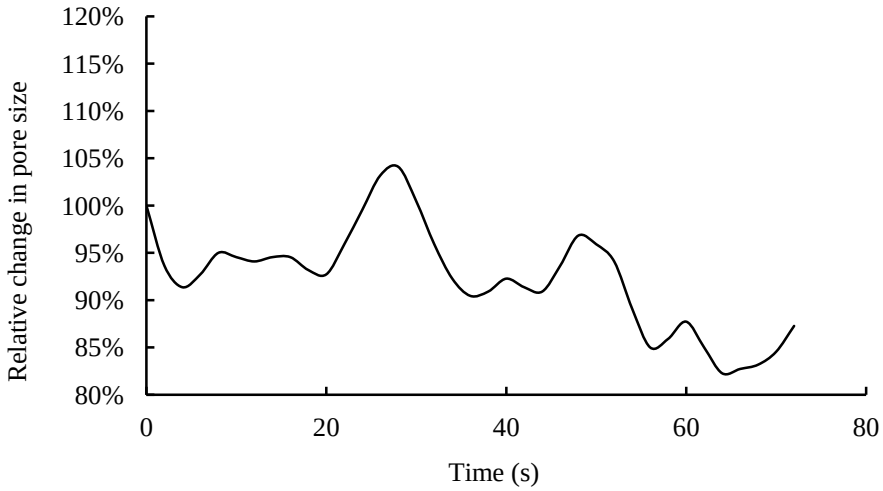

Fig. 4.12. Relative change in area of triangle formed by three particles during vibration at 25 Hz frequency and 0.45 mm amplitude (based on data reported by Liu 2008).

4.1.4.3 **Effects of vibration intensity on porosity**

Vibration intensity had noticeable effect on porosity during vibration (Fig. 4.13). The higher the intensity, the greater the fluctuations. Among the five intensity levels simulated (0.45g, 0.91g, 1.81g, 2.72g, and 3.62g), 1.81g resulted in the lowest porosity (Fig. 4.14). A similar observation was reported by An X.Z. et al. (2009). Based on experimental measurements, An X.Z. et al. (2009) observed that an assembly of spheres with diameter of 5.02 mm in a 229.70-mm diameter container when subjected to vibration between 0.25g and 5.0g, and observed that the highest packing density occurred in the mid-range vibration intensities between 2.0g and 5.0g. Theoretically speaking, if the acceleration of particles in a porous bed is greater than 1g in the vertical direction, the particles could become "afloat" once in every vibration cycle, which could result in a high probability of creating a large void into which another particle can slide, thus providing the best opportunity to form a dense structure. Therefore, lower vibration intensity (<1g) would produce lower reduction in porosity. However, it should be noted that a porous bed is a discrete systems and not all particles vibrate at the same frequency and amplitude as the excitation applied on the containing structures (the bin bottom in this study). Energy transfer in the porous bed when subjected to vibration is extremely complicated, however it is a reasonable assumption that not all vibration energy from the vibration source applied at the bin bottom would be transferred to the particles in the porous bed because of energy dissipation by collision and friction among particles and between particles and the containing structures. Energy dissipation in granular materials during vibration has been shown to be significant in many studies in the area of particle impact damping (Friend and Kinra 2000). The reason of the maximum reduction in porosity occurred

at 1.8g instead of 1g is that the critical vibration intensity would vary with many factors that influence energy transfer in porous beds, including particle size and shape, particle density, friction between particles, friction between particles and containing structures, restitution coefficient, and even porosity itself, which dictates the distances between particles and between particles and containing structure.

An et al. (2009) explained that too high energy input would over-excite particles in porous beds, which would lead to less dense structures. While low amplitude vibration induces subtle changes in the microstructure of a granular material, resulting in higher bulk density, strong vibration leads to fluid-like behavior of the granular material, resulting in lower bulk density (Rosato et al. 2002). Hunt et al. (1994) conducted experiments to study the behavior of a granular material subjected to vertical vibration at acceleration levels from 1g to 5g. They observed that the volume of the granular material began to expand at acceleration of 2g.

At high vibration intensity (3.62g), porosity fluctuated markedly both locally and globally. In contrast, at low intensity of 0.45g, porosity only fluctuated slightly around its average (Fig. 4.13.) This meant that vibration energy at low intensity was not sufficient to cause significant particle re-arrangement and particles vibrated as continuum with the bin. Liu et al. (2010) used a high speed camera to study vibration of individual particles in a bin subjected to vertical vibration and observed that all particles in the bin vibrated as a continuum with the same frequency and amplitude as the excitation at low intensities (<1g), whereas individual particles vibrated “irregularly” (not following the harmonic excitation) when the vibration intensities were high (>1g). When vibration intensity is too high, it may over-excite the packing structure, resulting in a less dense packing (An et al. 2009).

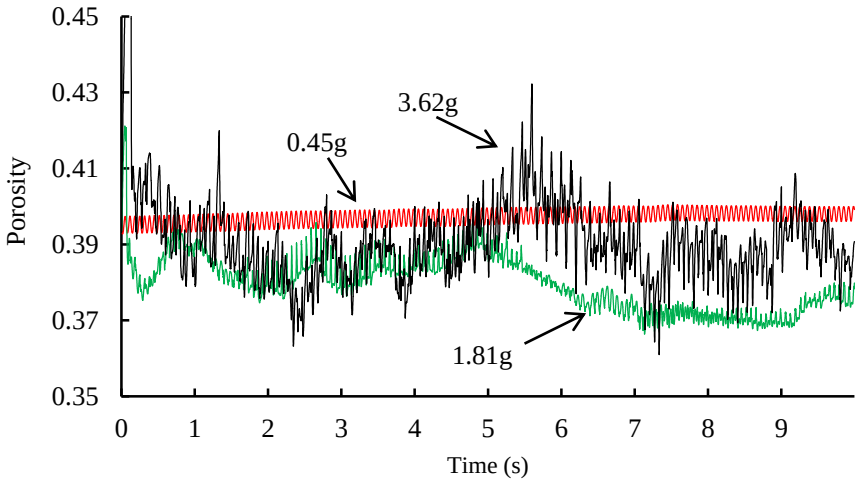

Fig. 4.13. Simulated average local porosity during vibration at intensities of 0.45g, 1.81g, and 3.62g.

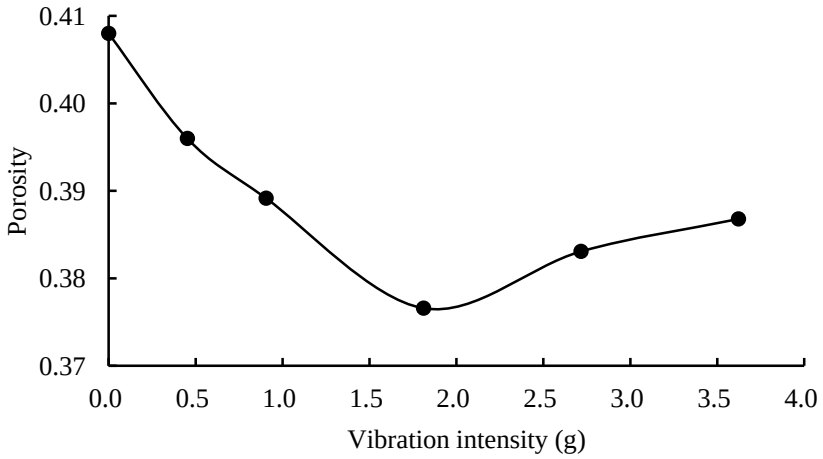

Fig. 4.14. Effect of vibration intensity on porosity.

4.1.4.4 **Effects of vibration on airflow path**

Vibration changed the shape of airflow path (Fig. 4.15). Qualitatively speaking, the deviation of flow path (the exit point) from the entry point was less before vibration than after vibration. This was probably because of higher flow resistance in more dense porous beds after vibration made it more difficult for flow to go upwards directly. Nwaizu and Zhang (2015) used

imaging techniques to study airflow through grain bulks subjected to vibration and observed that reduction in porosity after vibration caused more lateral “branching” of flow when air entered the grain bulks vertically. In other words, more air was forced to flow in non-vertical directions after vibration. It was interesting to note that while there was less degree of deviation of flow path from the entry point after vibration, but more sharp local turns was observed. This became apparent when comparing the flow paths between 0g and 1.81g vibration intensities. Specifically, many small sharp local turns could be seen in the 0g path, whereas long sections of relatively smooth line existed in the 1.81g path (Fig.4.15).

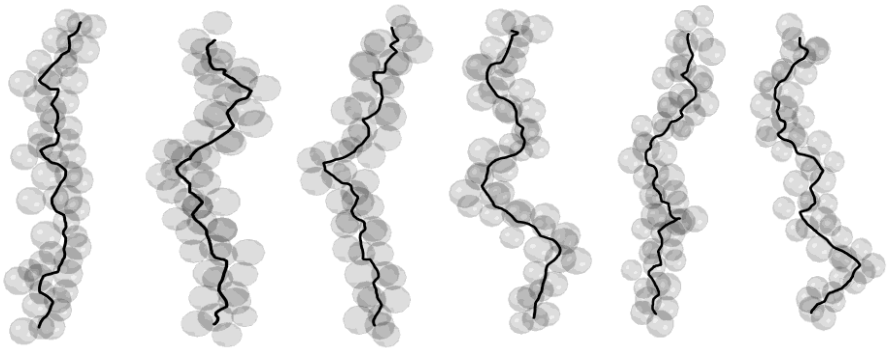

Fig. 4.15. Typical simulated airflow paths (reduced to 2D) for different vibration intensities.

Both the deviation of flow path from the entry point and the local turns would result in longer flow paths (higher tortuosity). To further quantify the differences in airflow path among different vibration intensities, the simulated tortuosity values were compared (Fig. 4.16). The tortuosity decreased after vibration generally, but no clear pattern could be identified. A maximum reduction of 9% was observed for vibration intensity of 1.81g and a minimum 2% for 2.72g. Many studies have shown that tortuousness of flow through porous media decreases

with porosity (Pisani 2011). As discussed earlier, the lowest porosity occurred at 1.81g. Therefore, it was expected that flow path for 1.81g vibration would be less tortuous. This also meant the sharp local turns (dominant before vibration) had more effect on the tortuousness of flow path than did the deviation (dominant after vibration) from the entry point. Although the maximum reduction in tortuosity corresponded to the minimum porosity at 1.81g, the pattern of variation in tortuosity with vibration intensity did not quite follow that for porosity shown in Fig. 4.14.

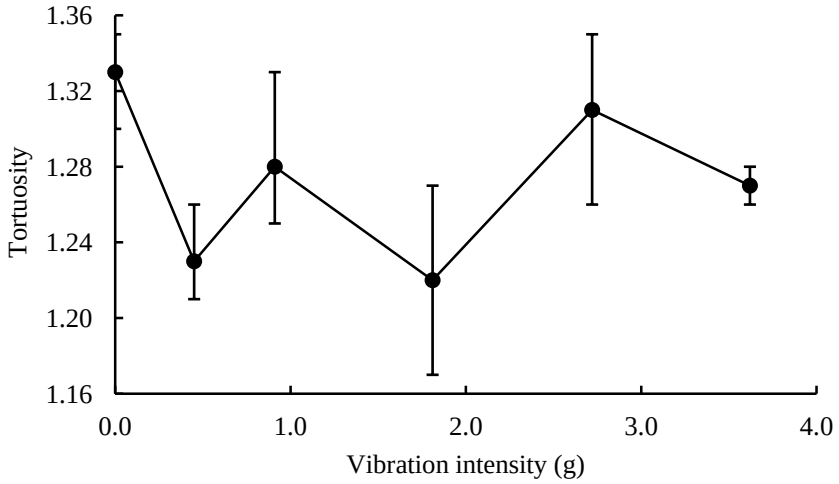

Fig. 4.16. Variation of simulated tortuosity with vibration intensities (each data point represents the average of three simulated paths and the error bar indicates the minimum and maximum values).

The pore throat width (the equivalent diameter) of the widest local flow path was calculated for each tetrahedron unit associated with a global flow path (Fig. 4.17). It was observed that the throat width varied randomly between 1.3 and 4.6 mm, with one exception before vibration – a high value of 6.8 mm was observed. A pore throat of 6.8 mm was apparently greater than the average particle diameter. This meant that a macro-pore (defined as pores large enough to accommodate a particle, An X.Z. et al. 2005) existed in the porous bed

before vibration, but no macro-pores were observed after vibration at any of the five vibration intensities studied.

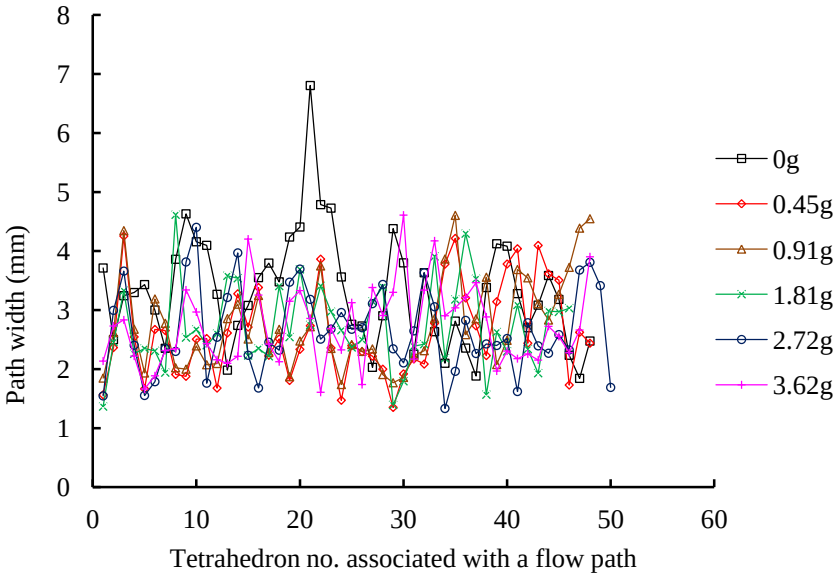

Fig. 4.17. Pore throat width of local flow paths from the bin bottom (tetrahedron no. 1) to the top under different vibration conditions.

To further examine the effect of vibration intensity on pore throat width, the distributions of throat width were plotted (Fig. 4.18). The highest percentage of pore throats was in the 3-4 mm range before vibration, while the highest percentage after vibration was in the 2-3 mm range. The percentage of pore throats in the range of 1-2 mm and 2-3 mm before vibration was much lower than that after vibration, whereas the percentage in 4-5 mm before vibration was much higher than that after vibration. This observation indicated that vibration reduced the pore throat width. On average, the pore throat width was 3.3, 2.6, 2.8, 2.7, 2.7, and 2.7 mm for 0g (before vibration), 0.45g, 0.91g, 1.81g, 2.72g, and 3.62g, respectively. While the average pore throat before was greater than those after vibration, the differences in pore throat width among the five different vibration intensities were negligible (< 0.2 mm).

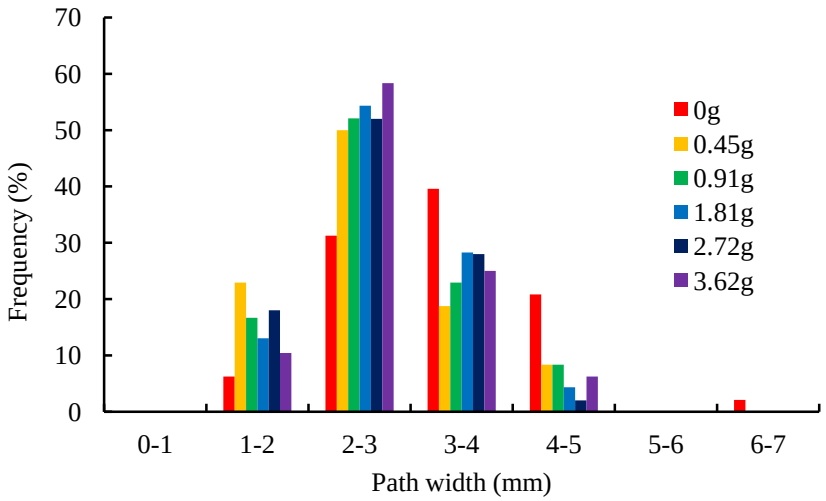

Fig. 4.18. Distribution of pore throat width under different vibration intensities.

4.2 Airflow resistance

4.2.1 Experimental results

The measured pressure drops varied little in the radial direction at the measurement depth of 150 mm. Specifically, the measured pressure along the bin central line (Location 2, Fig. 3.19) was 1.12 ±0.042 Pa at a specific flow rate of 0.013 $m^3 s^{-1} m^{-2}$ while the corresponding pressures at 0.5r (r is the bin radius) from the bin central line (Locations 2A and 2B) were 1.14 ±0.025 Pa and 1.14 ±0.050 Pa. The maximum difference was 2% between the pressure drop at the bin centre and that at 0.5r. Therefore, pressure variation in the radial direction was negligible.

Fluid flow through a packed bed with Reynolds number less than 10 is generally considered as laminar flow (Dwivedi, 1977). The Reynolds number used in this study was 34, and therefore, some inertial effect might exist. To assess a possible inertial effect, pressure drops were measured at a range of airflow rates four airflow rates (6.0×10^{-5} $m^3 s^{-1}$, 1.2×10^{-4} $m^3 s^{-1}$, 2.5×10^{-4} $m^3 s^{-1}$ and 5.0×10^{-4} $m^3 s^{-1}$) were selected to measure the pressure drop (Fig. 4.19). The general trend of pressure variant with the superficial velocity was fairly linear (R^2 = 0.98),

meaning the initial effect was minimal. However, further comparison of the slope of each individual line segment connecting two consecutive data points with the regression line revealed that the pressure variation with superficial velocity was fairly linear up to 0.013 $m^3 s^{-1} m^{-2}$, but became slightly nonlinear (a greater slope) between 0.013 and 0.027 $m^3 s^{-1} m^{-2}$. This indicated that slight inertial effect might exist at superficial velocity higher than 0.013 $m^3 s^{-1} m^{-2}$ in the experiments.

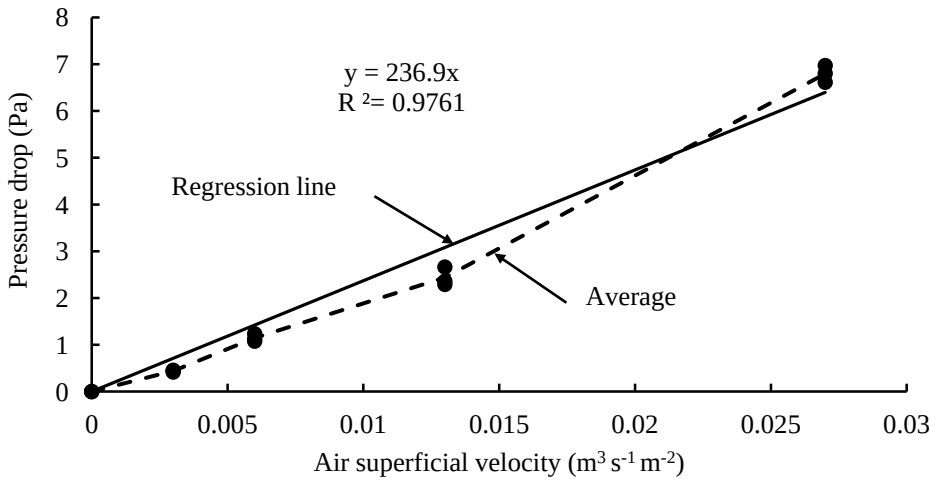

Fig. 4.19. Pressure drop of airflow through the grain bed at different superficial velocities (three replicates).

4.2.2 **Prediction by branched path model**

As discussed in Section 3.4.1, the local flow path width (LFPW), determined as the cross-sectional area of local flow path within each tetrahedron, was one of the most important parameters in calculating the pressure drop, but the LFPW was highly irregular and varied along the local flow path, as illustrated in Fig. 4.20. Specifically, LFPW shrank from the centroid of tetrahedron to the pore throats. To investigate the effect of LFPW on pressure drop calculation, three values of LFPW were considered – the maximum, the minimum and the

average, which were calculated using Eq. 3.24 in Section 3.2.1. The pressure drops predicted by the branched path model based on these three LFPW values, as well as different multiplier functions (MF×2 and MF×3) are shown in Table 4.4a&b. The LFPW value had a drastic effect on predicted pressure; the differences in predicted pressure drops between the minimum and maximum LFPW values ranged from 2.8 to 7.2 times. The averaged predicted pressure drops with multiplier function MF×3 were 2.74 and 5.65 Pa for superficial velocity of 0.013 $m^3 s^{-1} m^{-2}$ and 0.027 $m^3 s^{-1} m^{-2}$, respectively, while the averaged predicted pressure drops with multiplier function MF×2 were 1.99 Pa and 4.13 Pa, respectively. In comparison with experimental data (2.44±0.20 Pa and 6.80 Pa for superficial velocity of 0.013 $m^3 s^{-1} m^{-2}$ and 0.027 $m^3 s^{-1} m^{-2}$, respectively), it was apparent that MF×3 was closer (12% vs. 18% and 17% vs 39% for superficial velocity of 0.013 $m^3 s^{-1} m^{-2}$ and 0.027 $m^3 s^{-1} m^{-2}$, respectively) to the experimental data than with MF×2. This might be attributed to sharp flow branching inside each tetrahedron unit because the local flow paths inside tetrahedrons were highly irregular. Therefore, it was concluded that the MF×3 multiplier function should be used in predicting pressure drop. When the MF×3 multiplier (along with the average LFPW) was used in the model, the predicted pressure drops were in good agreement with measured value. Specifically, the predicted pressure drops were 3.07 Pa and 2.40 Pa for the narrowest and the widest paths, respectively, while the experimental value was 2.44±0.20 Pa (for superficial velocity of 0.013 $m^3 s^{-1} m^{-2}$). The average predicted pressure (2.74 Pa) was 12% higher than the measured value. For superficial velocity of 0.027 $m^3 s^{-1} m^{-2}$, the predicted pressure drops were 6.30 Pa and 5.00 Pa for the narrowed and the widest paths, respectively, which were lower (17% on average) than the measured pressure drop of 6.80±0.18 Pa. The lower predicted pressure drop by the

proposed model at higher flow rate was probably related to the inertial effect (as shown in Fig. 9), which was not considered in the model.

In comparison with experimental data, it was apparent that the use of minimum LFPW over predicted the pressure drop, whereas the use of maximum LFPW under predicted. For example, using the minimum LFPW with MF×3, the predicted pressure drops were 11.30 Pa and 6.67 Pa for the narrowest and widest paths, respectively (for superficial velocity of 0.013 $m^3 s^{-1} m^{-2}$), while the measured pressure was 2.44±0.20 Pa. This meant that the average predicted pressure drop (8.99 Pa) was 268% higher than the measured value. In contrast, using the maximum LFPW with MF×3, the predicted pressure drops were 1.80 Pa and 1.73 Pa for the narrowest and widest paths respectively, and the average predicted value (1.77 Pa) was 27% lower than the measured value. This trend was expected as the minimum and maximum LFPW represented two extreme cases. The true local path width lied between the maximum and minimum LFPWs, but it could not be obtained through model simulations or any other means. In this work, the average path width (the arithmetic mean of the minimum and maximum path width) was used as the best approximation to the width of local flow path in calculating the average pressure drop. Using the average LFPW, the predicted pressure drop was 12% higher than the measured value for superficial velocity of 0.013 $m^3 s^{-1} m^{-2}$ and 17% lower than the measured value for superficial velocity of 0.027 $m^3 s^{-1} m^{-2}$.

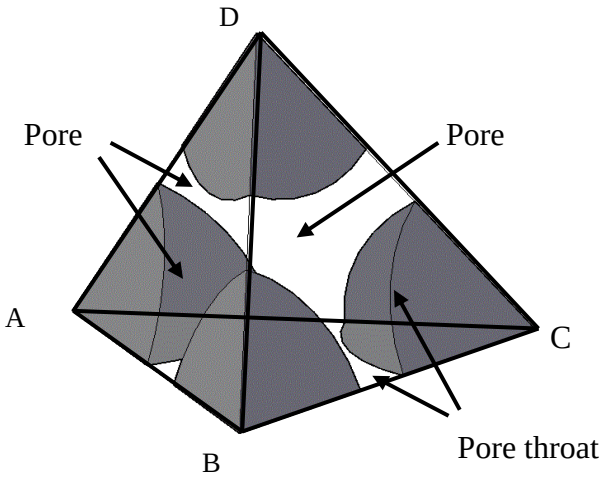

Fig. 4.20. Illustration of local flow path in a tetrahedron unit.

Table 4.4a. Predicted pressure drops for the three widest airflow paths through the grain bed based on different LFPW as well as different multiplier functions.

LFPW		Pressure drop (Pa)			
		(MF×3)		(MF×2)	
		HSV	LSV	HSV	LSV
AEP1	Max	2.9	1.4	2.0	1.0
	Min	14.4	6.9	10.6	5.1
	Average	4.1	2.0	3.0	1.4
AEP2	Max	3.7	1.8	2.6	1.2
	Min	10.3	5.0	7.5	3.6
	Average	5.1	2.4	3.6	1.7
AEP3	Max	4.1	2.0	2.9	1.4
	Min	16.9	8.1	12.4	6.0
	Average	5.8	2.8	4.2	2.0

Table 4.4b. Predicted pressure drops for the three narrowest airflow paths through the grain bed based on different LFPW as well as different multiplier functions.

	LFPW	Pressure drop (Pa)			
		(MF×3)		(MF×2)	
		HSV	LSV	HSV	LSV
AEP1	Max	3.3	1.6	2.5	1.2
	Min	23.6	11.4	17.2	8.3
	Average	5.8	2.8	4.3	2.1
AEP2	Max	3.7	1.8	2.8	1.3
	Min	22.3	10.7	16.6	8.0
	Average	6.1	3.0	4.5	2.2
AEP3	Max	4.2	2.0	3.1	1.5
	Min	24.6	11.8	18.4	8.9
	Average	7.0	3.4	5.2	2.5

Note:
AEP: Air entry point
LFPW: Local flow path width
MF×3: Multiplier function $f(\theta) = 3 - 2\cos\theta_i$
MF×2: Multiplier function $f(\theta) = 2 - \cos\theta_i$
LSV: low superficial air velocity at 0.013 $m^3 s^{-1} m^{-2}$
HSV: high superficial air velocity at 0.027 $m^3 s^{-1} m^{-2}$

The predicted pressure drops were also compared with the ASABE Standard (ASABE 2011). In ASABE Standard, the airflow resistance (pressure drop) was calculated as follows:

$$\frac{\Delta P}{\Delta L} = \frac{a_2 Q^2}{log_e(1+b_2 Q)} \quad (4.1)$$

Where ΔP is pressure drop (Pa), ΔL is bed depth (m), Q is airflow superficial velocity (m s^{-1}) and a_2, b_2 are constants for a particular grain.

For soybeans, the two constants were found to be a = 1.02×10^4 Pa s^2 m^{-3} and b = 16.0 m^{-1} s. The pressure drops of airflow through soybeans were calculated to be 2.28 Pa and 5.18 Pa for superficial velocities of 0.013 and 0.027 $m^3 s^{-1} m^{-2}$, respectively.

The predicted pressures were also compared with Ergun's equation. Using an air viscosity

of 1.93×10^5 Pa s and density of 1.20 kg m^{-3}, the Ergun equation yielded a pressure drop of 1.27 Pa for superficial velocity of 0.013 $m^3 s^{-1} m^{-2}$ and 2.90 Pa for 0.027 $m^3 s^{-1} m^{-2}$.

The comparison between the experimental results of pressure drop with their simulated values and the data found in the literature is summarised in Table 4.5. The relative differences were calculated as the ratio of the difference divided by the experimental value. The pressure drop estimated by ASABE Standard was 24% and 7% lower than the experimental results for superficial velocities of 0.013 $m^3 s^{-1} m^{-2}$ and 0.027 $m^3 s^{-1} m^{-2}$, respectively, while the value estimated by Ergun's equation was 57% and 48% lower than the measured value for 0.013 m s^{-1} and 0.027 m s^{-1}, respectively (Table 4.5). The average pressure drop predicted by the branching model was 20% and 9% higher than the value estimated by ASABE Standard for air superficial velocity of 0.013 $m^3 s^{-1} m^{-2}$ and 0.027 $m^3 s^{-1} m^{-2}$, respectively (Table 4.5). The pressure drop predicted by the branching model was 116% and 95% higher than the value estimated by Ergun's equation for superficial velocity of 0.013 $m^3 s^{-1} m^{-2}$ and 0.027 $m^3 s^{-1} m^{-2}$, respectively (Table 4.5).

Table 4.5. Comparison of simulation results of pressure drop for airflow through the grain bed with experimental results and the literature data.

Calculation method	Pressure drop (Pa)		Pressure drop difference compared with experiment	
	HSV	LSV	HSV	LSV
Experiment	6.80	2.44	/	/
Branched model	5.65	2.74	-17%	12%
ASABE Standard	5.18	2.28	-24%	-7%
Ergun's equation	2.90	1.27	-57%	-48%

LSV: low superficial air velocity at 0.013 $m^3 s^{-1} m^{-2}$
HSV: high superficial air velocity at 0.027 $m^3 s^{-1} m^{-2}$

4.2.3 **Prediction by network model**

The grain bed simulated by the DEM model consisted of 19,171 spheres which were used in Delaunay tessellation, which in turn resulted in 119,309 tetrahedron units (pores). The interior tetrahedrons were selected by the lowest centroid of the three triangle faces within a certain range of location (-0.051 m< x <0.051 m,-0.051 m< y<0.051 m, 0.026 m < z <0.224 m). Consequently 51170 interior tetrahedrons were selected, in which 1348 pores bordering the inlet and 1380 pores bordering outlet. A set of 51170 linear matrix equations were obtained by rearranging the Eq. 3.39 for the pressures in each pores. Then an additional equation constraining the sum of flow rates (2.5×10^{-4} m) into all inlet pores was added to the matrix as a boundary consition to sovle the pressure in each tetrahedron unit. Two widest airflow paths calculated from the algorithm were tracked from the bottom to the top surface of the grain bed and the pressure drops along these two airflow paths were determined.

Compared with the 108 and 109 tetrahedrons units along the two airflow paths calculated from the algorithm, Delaunay tessellation resulted in 90 and 89 tetrahedron units along two widest airflow paths, respectively, and corresponding pressure drops were 1.65 and 1.67 Pa for the two paths. The tetrahedron units which located lower than 0.026 m and higher than 0.224 m were removed when selecting the interior tetrahedrons. By adding the averaged measured values of pressure drop (0.54 Pa) for bed depth of 0.5 m, the estimated average predicted pressure drop of two paths through a 0.25 m thicked bed was 2.20 Pa at a flow rate of 0.013 m^3 s^{-1} m^{-2}. This predicted pressure drop was 2.20 Pa (10%) lower than the measured value (2.44 Pa). The predicted pressure was almost identical to the ASABE standard (2.28 Pa for a 0.25 m thick bed of soybeans at a flow rate of 0.013 m^3 s^{-1} m^{-2}).

Using Ergun's equation, the pressure drop for airflow through a 0.25 m bed was calculated to be 1.27 Pa. In other words, the pressure drop predicted by the current model was 73% higher than that calculated by Ergun's equation (2.20 vs. 1.27 Pa). The difference could be explained as the Ergun's equation did not consider the connectivity and tortuosity of pore structures of porous beds.

5 Conclusions

5.1 Discrete element modeling of pore structure and airflow path

The discrete element model (DEM) developed using PFC^{3D} provided a powerful tool to simulate the pore structures of grain beds. Based on the DEM simulations, airflow paths through the pore space between grain kernels could be geometrically constructed and some critical pore structure parameters for flow through grain beds could be predicted, including porosity, tortuosity, pore throat width, and flow path geometry (length and shape).

The simulated (local) porosity varied from location to location in the grain bed. Macro-pores, defined as a pore large enough to accommodate a particle, existed locally in the grain bed, and these macro-pores could result in high local porosity. Based on the DEM simulation, the widths of airflow paths could be quantified. On average, the path widths of three randomly selected widest airflow paths were 57% bigger than that of three narrowest airflow paths. More degree of deviation but less sharp turns of the airflow path were observed for three narrowest paths than that of three widest paths. However, the average tortuosities for

the two types of paths were almost the same (1.39 vs. 1.40). Air entering a grain bin (bed) at a particular point would follow a unique path and be subjected to specific resistance as it passed through the grain bed.

5.2. Airflow resistance modelling

The pore structures simulated by the discrete element method provided a base on which pore-scale models could be developed for predicting resistance to airflow through grain beds. By considering pressure drop within a local flow path as the sum of friction and branching losses, the proposed branched path model adequately predicted pressure drops through a grain bulk. The predicted pressure drop was about 12% higher than the experimental value at a low superficial velocity of 0.013 $m^3 s^{-1} m^{-2}$ at which the inertial effect was negligible, but 17% lower than the experimental value at a high superficial velocity of 0.027 $m^3 s^{-1} m^{-2}$ at which some inertial effect might exist.

The DEM simulations of the pore structure combined with Delaunay tessellation provided a powerful tool for developing the network models for the porous media. The predicted pressure drop of flow through the grain bed based on the pore-scale network model was about 10% lower than the experimental value at an airflow superficial velocity of 0.013 $m^3 s^{-1} m^{-2}$.

5.3. Effect of vibration

The influence of vibration on porosity was clearly demonstrated. A vibration intensity of 1.81g resulted in the lowest porosity (6% lower than that before vibration). Lower vibration

intensity did not have enough energy to cause much change in porosity, while higher intensity over-excited particles, producing less dense packing than did 1.81g. Local porosity fluctuated markedly during vibration, probably due to repeated formation and destruction of instant (unstable) macro-pores (defined as pores large enough to accommodate a particle). Tortuousness of flow path was noticeably affected by vibration. Tortuosity of the porous bed before vibration was higher (2% - 9%) than that after vibration. Pore throats larger than the average particle diameter (due to macro-pores) existed in the porous bed before vibration, but were not observed after vibration. Vibration reduced the pore throat width. The highest percentage of pore throats was in the range of 3-4 mm before vibration, and reduced to 2-3 mm after vibration. The reduction in average pore throat width was 22% after vibration.

6 Recommendations

In the DEM model of grain bulks, soybeans were assumed as spherical particles in the simulations, which is not true in the real case. The non-spherical shape of grain kernels may result in the difference of pore structure (air space, path width and length, etc.) and the resistance to airflow in the vertical and horizontal direction of grain bulks. Further research is needed to simulate the pore structure of non-spherical particles and investigate the difference of pore structure and corresponding resistance to airflow through the porous bed.

In the pore-scale branching model, the average LFPW calculated by the arithmetic mean of maximum and minimum LFPW did not predict the true airflow path width very well. It is recommended to find a better predictor of true airflow path to calculate the pressure drop for flow through the grain bed. Flow through grain beds was assumed as laminar flow without

considering inertial effects. Inertial effects should be considered in further research.

The influence of vibration in terms of vibration intensity given by a fixed of frequency and multiple amplitudes on porosity of porous beds was demonstrated. It is imperative to further clarify the effect of vibration intensity given by a varying frequency and fixed amplitudes on porosity of porous beds.

References

Acton, J. M., H. E. Huppert, and M. G. Worster. 2001. Two-dimensional viscous gravity currents flowing over a deep porous medium. *Journal of Fluid Mechanics*, 440: 359-380.

Agrawal K. K., and P. Chaud. 1974. Pressure drop across fixed beds of rough rice. Transactions of the ASAE, 17(3): 560-563.

Agullo, C. F., and M. O. Marenya .2005. Airflow resistance of parchment Arabica coffee. *Biosystems Engineering*, 91 (2): 149-156.

Alem, P., T. Byholm and M. Toivakka. 2006. Calculating tortuositiy in quasi-random anisotropic packings. *Nordic pulp and paper research Journal*, 21(5): 670-675.

Al-Kharusi, A. S. and M. J. Blunt. 2007. Network extraction from sandstone and carbonate pore space images. *Journal of Petroleum Science and Engineering*, 56(4): 219-231.

Amanlou. Y and A. A. Zomorodian. 2011. Resistance to air flow across a thin green fig bed. Journal of Agricultural Science and Technology, 13(5): 677-685.

An X. Z., C. X. Li. R. Y. Yang. R. P. Zou and A. B. Yu. 2009. Experimental study of the packing of mono-sized spheres subjected to one-dimensional vibration. *Powder Technology*, 196: 50-55.

An X. Z., R. Y. Yang. K. J. Dong. R. P. Zou and A. B Yu. 2005. Micromechanical simulation and analysis of one-dimensional vibratory sphere packing. *Physical Review Letters*, 95: 205502.

ASABE Standards. 2011. D272.3: Resistance to airflow of grains, seeds, other agricultural products, and perforated metal sheets. St. Joseph, Mich.: ASABE.

Asaf, Z., D. Rubinstein, and I. Shmulevich. 2006. Evaluation of link-track performances using DEM. *Journal of Terramech*, 43(2): 141-161.

Baars, S. V. 1996. Discrete element modelling of granular materials. Heron, 41(2): 139-157.

Bafna, S. S., and D. G. Baird. 1992. An impregnation model for the preparation of thermoplastic prepregs. *Journal of Composite Materials*, 26(5): 683-707.

Bakke, S., & Oren, P. E. 1997. 3-D pore-scale modelling of sandstones and flow simulation in the pore networks. Society of Petroleum Engineers Journal, 2(2): 136-149.

Balhoff, M. T., & Thompson, K. E. 2004. Modeling the steady flow of yield stress fluids in packed beds. *American Institute of Chemical Engineers Journal*, 50(12): 3034-3048.

Balhoff M. T., K. E. Thompson and M. Hjorts¢a 2007. Coupling pore-scale networks to continuum-scale models of porous media. *Computers & Geosciences*, 33: 393-410.

Barr, D. W. 2011. Coefficient of permeability determined by measurable parameters. *Ground Water,* 39(3), 356-361.

Beard, D. C., and P. K. Weyl. 1973. Influence of texture on porosity and permeability of unconsolidated sand. *AAPG Bulletin*, 57: 349-369.

Bear, J., D. Zaslavsky, and S. Irmay. 1968. Physical Principles of Water Percolation and Seepage, UNESCO, Paris.

Bern, C. J., and L. F. Charity .1975. Airflow resistance characteristics of corn as influenced by bulk density. ASAE Paper No. 75-3510. St. Joseph, MI: ASAE.

Bird, R. B. 1996. Transport Phenomena. Madison, Wisconsin: John Wiley & Sons. New York.

Blunt, M., and P. King. 1990. Macroscopic parameters from simulations of pore scale flow. Physical Review A, 42(8): 4780-4787.

Boac, J. M., M. E. Casada, R. G. Mafhirang, and J. P. Harner. 2010. Materials and interaction properties of selected grains and oilseeds for modeling discrete particles. *Transactions of ASABE*, 53(4): 1201-1216.

Boac J. M., R. P. K. Ambrose. M. E. Casada. R. G. Maghirang and D. E Maier. 2014. Applications of discrete element method in modeling of grain postharvest operations. *Food Engineering Reviews*, 6: 128-149.

Bowyer, A. 1981. Computing Dirichlet tessellations. *The Computer Journal*, 24(2): 162-166.

Bradshaw, R. D., & Myers, J. E. 1963. Heat and mass transfer in fixed and fluidized beds of large particles. *AIChE Journal*, 9: 590-595.

Brown, G. O. 2002. The history of the Darcy-Weisbach equation for pipe flow resistance. In A. Fredrich and J. Rogers, editors, Proceedings of the 150th Anniversary Conference of ASCE, Wachington D.C., pages 34-43. American Society of Civil Engineers, November 3-6. Available at http://bioen.okstate.edu/Darcy/DarcyWeisbach/HistoryoftheDarcyWeisbachEq.pdf, assessed 2 August 2011.

Bryant, S. L., & Blunt, M. 1992. Prediction of relative permeability in simple porous-media. Physical Reviews A, 46(4): 2004-2011.

Bryant, S. L., King, P. R., & Mellor, D. W. 1993a. Network model evaluation of permeability and spatial correlation in a real random sphere packing. Transport in Porous Media. 11(1): 53-70.

Bryant, S. L., Mellor, D. & Cade, C. A. 1993b. Physically representative network models of transport in porous-media. American Institute of Chemical Engineers Journal, 39(3):

387-396.

Calderwood, D. L. 1973. Resistance to airflow of rough, brown, and milled rice. *Transactions of ASAE*, 16(3): 525-527,532.

Carman, P. C. 1937. Fluid through granular beds. *Transactions of the Institution of Chemical Engineers*, 15:150-166.

Chakraverty, A., A. S. Mujumdar, G. S. V. Raghavan, and H. S. Ramaswarmy. 2003. Handbook of postharvest technology: cereals, fruits, vegetables, tea and spices. Marcel Dekker, Inc. US. P20.

Chen, S., and G. D. Doolen. 1998. Lattice Boltzmann Method for fluid flows. *Annual Review of Fluid Mechanics*, 30: 329-364.

Chareyre B., A. Cortis. E. Catalano. and E. Barthelemy. 2012. Pore-scale modeling of viscous flow and induced forces in dense sphere packings. *Transport in Porous Media*, 92(2): 473-493.

Chu. C. F., and K. M. Ng .1989. Flow in packed tubes with a small tube to particle diameter ratio. A.I.C.h.E. J. 35: 148-156.

Chung, D. S., and H. H. Converse. 1971. Effect of moisture on some physical properties of grains. *Transactions of ASAE*, 14(4): 612-614, 620.

Chung, Y. C., and J. Y. Ooi. 2008. A study of influence of gravity on bulk behavior of particulate solid. *Particuology*, 6(6): 467-474.

Cleary, P. W. 1999. The effect of particle shape on hopper discharge. Second International Conference on CFD in the Minerals and Process Industries CSIRO, Melbourne, Australia.

Cleary, P. W., and M. L. Sawley. 2002. DEM modeling of industrial granular flows: 3D case

studies and the effect of particle shape on hopper discharge. *Applied Mathematical Modeling Journal*, 26(2): 89–111.

Coetzee, C. J., and D. N. J. Els. 2009. Calibration of discrete element parameters and the modeling of silo discharge and bucket filling. *Computers and Electronics in Agriculture*, 65(2): 198-212.

Coles, M. E., and K. J. Hartman. 1998. Non-Darcy measurements in dry core and the effect of immobile liquid. *In: SPE 39977, presented at SPE Gas Technolofy Symposium*, Calgary, Alberta, Canada.

Comiti, J., and M. Renaud. 1989. A new model for determining mean structure of fixed beds from pressure drop measurements: application to beds with parallelepipedal particles. *Chemical Engineering Science*, 44(7):1539-1545

Coskun, M. B., I. Yalçın, and C. Özarslan. 2006. Physical properties of sweet corn seed. *Journal of food engineering*, 74(4): 523-528.

Cundall, P. A. 1971. A computer model for simulating progressive large scale movements in blocky rocks systems. *Proceedings of the Symposium of the International Society of Rock Mechanic*s, 2(8): 129.

Cundall, P. A., and O. P. L. Strack. 1979. A discrete numerical model for granular assemblies. *Geotechnique*, 29(1): 47-65.

Dagan, G., U. Hornung, and P. Knabner. 1991. Mathematical modeling for flow and transport through porous media. *Kluwer Acamedic Publisher*. The Netherlands.

Dairo, O. U., and O. O. Ajibola 1994. Resistance to airflow of bulk sesame seed. *Journal of Agricultural Engineering Resource*, 58(2): 99-105.

Dong, H. .2007. Micro CT imaging and pore network extraction. Ph.D. thesis. Imperial College London.

Dudda W. and W. Sobieski. 2014. Modification of the pathfinder algorithm for calculating granular beds with various particle size distributions. *Technical Sciences*, 17: 135-148.

Dukhan, N. 2006. Correlations for the pressure drop for flow through metal foam. *Experiments in Fluids*, 41(4): 665-672.

Du Plessis, J. P., and J. H. Masliyah. 1991. Flow through isotropic granular porous media. *Transport in Porous Media*, 6(3): 207–221.

Du Plessis, J. P., and S. Woudberg. 2008. Pore-scale derivation of the Ergun equation to enhance its adaptability and generalization. *Chemical Engineering Science*, 63(9): 2576-2586.

Endo, K., K. Sairyo, S. Komatrsubara, T. Sasa, H. Egawa, D. Yonekura, D. Adachki, R. Murakami, and N. Yasui. 2002. Cyclooxygenase-2 inhibitor inhibits the fracture healing. *Journal of Physiol Anthropol Appl Human Science*, 21(5): 235-238.

Ergun. (1952). Fluid Flow through Packed Columns. *Chemical Engineering Progress* 48(2): 89-94.

Farmer, G. S., G. S. Busewitz. and R. W. Whitney. 1981. Resistance to airflow of Bluestem grass. *Transactions of ASAE*, 24(2): 480-483.

Fatt, I. 1956. The network model of porous media II: dynamic properties of a single size tube network, Transactions of AIME, 207: 160-163.

Forchheimer. P. F. 1901. Wasserbewegung durch Boden. Zeitschrift des Vereines Deutscher Ingenieure, 45 (5): 1781-1788.

Friend R. D. and V. K.Kinra. 2000. Particle impact damping. *Journal of Sound and Vibration*, 233: 93-118.

Gao Y, X. Z, P. Rama, Y. Liu, R. Chen, H. Ostadi and K. J. 2011. Calculating the Anisotropic permeability of porous media using the Lattice Boltzmann Method and X-ray computed Tomography. *Transport in Porous Media*, 92:457-472.

Giner, S. A.,and E. Denisienia. 1996. Pressure drop through wheat as affected by air velocity, moisture content and fines. *Journal of Agricultural Engineering Research*, 63, 73-86.

Gonzalez-Montellano, C. 2011. Applications of the discrete element method to the study of granular materials stored in silos and hoppers. Ph.D thesis. University of Politecnica de Madrid, Spain.

Grama S. N., C. J. Bern, and Jr. C. R. Hurburgh. 1984. Airflow resistance of mixtures of shelled corn and fines. *Transactions of ASAE*, 27:268-272.

Grima, A. P., and P. W. Wypych. 2011. Discrete element simulations of granular pile formation: Method for calibrating discrete element models. *Engineering Computations*, 28(3): 314-339.

Groisman, A., and S. R. Quake. 2004. A microfluidic rectifier: Anisotrpic flow resistance at low Reynolds numbers. 2004. *Physical Review Letters*, 92(9).

Gunasekaran, S., and C. Y. Jackson. 1988. Resistance to airflow of grain sorghum. Transactions of the ASAE, 31(4): 1237-1240.

Handly, D., and P. J. Heggs. 1968. Momentum and heat transfer mechanics in regular shaped packings. Transactions of the Institution of Chemical Engineers, 46:

Hao, D., Q. Zhang, and M. G. Britton. 1994. Effect of vibration on loads in a corrugated model

grain bin. *Canadian Agricultural Engineering*, 36(1): 29-35.

Haque E., Y. N. Ahmed and C. W. Deyoe. 1982. Static pressure drop in a fixed bed of grains as affected by grain moisture content. *Transactions of ASAE*, 25(2): 1095-1098.

Haring, R. E., and R. A. Greenkorn .1970. A statistical model of a porous medium with nonuniform pores. *AIChE J*., 16(3): 477-483.

Henderson, S. M. 1943. Resistance of shelled corn and bin walls to air flow. *Agricultural Engineering*, 24(11): 367-369.

Henderson, S. M. 1944. Resistance of soybeans and oats to air flow. *Agricultural Engineering*, 25(4): 127-128.

Hicks, R. E. 1970. Pressure drop in packed beds of spheres. Eng. Chen. Chem. Fund. 9: 500-502.

Hill, R. J., D. L. Koch, A. J. C. Ladd. 2001. The first effects of fluid inertia on flows in ordered and random arrays of spheres. *Journal of Fluid Mechanics*, 448: 213-241.

Hood. T. J. A., and G. R. Thorp. 1992. The effects of the anisotropic resistance to airflow on the design of aeration systems for bulk stored grains. Agricultural Engineering Australia, 21: 18-23.

Huang, K., X. Wang, X. Liu, X. Wang, and D. Yang. 2013. Construction of three-dimensional pore network in bulk grain. *Drying Technology*, 31(15): 1871-1878.

Hukill, W. V., and N. C. Ives. 1955. Radial airflow resistance of grain. *Agricultural Engineering* 36(5), 332-335.

Hunt M.L., S. S.Hsiau and K. T.Hong. 1994. Particle mixing and volumetric expansion in a vibrated granular bed, *Journal of Fluids Engineering*, 116: 785-791.

Husain, A. and T. P. Ojha. 1969. Resistance to the passage of air through rice. *Journal of Agricultural Engineering Research*, 14(4): 47-53.

Jacob, B. (1988). Danymics of Fluids in Porous Media, New York, USA: Elsevier.

Jambhekar, V. A. 2011. Forchheimer porous-media flow models-numerical investifation and comparison with experimental data. Master's thesis. Universität Stuttgart.

Jamison, D. K., and Villemonte. J. R. 1971. Junction losses in laminar and transitional flows. *Journal of the Hydraulics Division Proceedings of the American Society of Civil Engineers*, 97(7): 1045-1063.

Jayas, D. S. 1988. Resistance of airflow through granular products-a review. *ASAE Paper No*.88-6534.

Jayas, D.S., and W. E. Muir. 1991. Airflow-pressure drop data for modeling fluid flow in anisotropic bulks. *ASAE*, 34(1): 251-254.

Jeraul, G. R., J. C. Hatfield. L. E. Scriven, and H. T. Davis. 1984a. Percolation and conduction on voronoi and triangular networks- a case-study in topological disorder. *Journal of Physics C: Solid State Physics*, 17: 1519-1529.

Jerauld, G. R., J. C. Hatfield, and H. T. Davis. 1984. Percolation and conduction on Voronoi and triangular networks: a case in topological disorder. Journal of Physics C, 17: 1519-1529.

Jerauld, G. R., L. E. Scriven, and H. T. Davis. 1984. Percolation and conduction on the 3d voronoi and triangular networks- a 2nd case-study in topological disorder. *Journal of Physics C: Solid State Physics*, 17(19): 3429-3439.

Jones, S. C. 1987. Using the inertial coefficient, βto characterize heterogeneity in reservior

rock. In: SPE 16949, presented at SPE Annual Technical Conference and Exhibition. Dallas, Texas, USA.

Kaleta, A., and K. Górnicki. 2011. Air flux (resistance) in plants and agricultural products. Encyclopedia of Agrophysics, part of the series Encyclopedia of Earth Sciences Series, 48-49. DOI:10.1007/978-90-481-3585_12

Kashaninejad, M., and L. G. Tabil. 2009. Resistance of bulk pistachio (Ohadi variety) to airflow. *Journal of Food Engineering*, 90(1):104-109.

Kendig, K. 2000. Is a 2000-year-old formula still keeping some secrets? *The American Mathematical Monthly*, 107(5): 402-415.

Kharaghani, A., T. Metzger, and E. Tsotsas. 2010. A proposal for discrete modeling of mechanical effects during drying, combining pore networks with DEM. AIChE Journal. 57(4): 872-885.

Khayargoli, P., V. Loya, L. P. Lefebvre, and M. Medraj. 2004. The impact of microstructure on the permeability of metal foams. *In: Proceedings of the CSME*, London, Canada, 220-228.

Koponen, A., M. Kataja, and J. Timonen. 1996. Tortuous flow in porous media. *Physical Review E*, 54(1): 406-410.

Koponen, A., M. Kataja, and J. Timonen. 1997. Permeability and effective porosity of porous media. *Physical Review E*, 56(3): 3319-3325.

Kozeny, J. 1927. Capillary motion of water in soils. Sitzungsberichte der Akactemie der Wissenschaften in Wien. Mathematisch-Naturwissenchaftliche Klasse, 136(5-6): 271-306.

Kozeny, J. 1933. Z. Pfl.-Ernahr. Dung. Bodenk, 28A: 54-56.

Lao, H. W., H. J. Neeman, and D. V. Papavassiliou. 2004. A network model for the calculation of non-Darcy flow coefficients in fluid flow through porous media. *Chemical Engineering c*ommunications, 191(10): 1285-1322.

Larson, R. E., and J. J. L. Higdon. 1987. Microscopic flow near the surface of two-dimensional porous media. *Journal of Fluid Mechanics*, 178:119-136.

Lee, J. W., M. Y. Kang, H. Y. Yang, and E. Lee. 2007. Fluid-dynamic optimality in the generation-averaged length-to-diameter ratio of the human bronchial tree. *Annals of Biomedical Engineering*, 45(11): 1071-1078.

Lee, E., M. Y. Kang, H. Y. Yang, and J. W. Lee. 2008. Optimality in the variation of average branching angle with generation in the human bronchial tree. *Annals of Biomedical Engineering*, 36(6): 1004-1013.

Lin, C. Y., & Slattery, J. C. 1982. Three-dimensional, randomized, network model for two-phase flow through porous media. AIChE journal, 28(2): 311-324.

Liu, C., Q. Zhang and Y. Chen. 2008a. PFC^{3D} simulation of vibration characteristics of bulk solids in storage bins. ASABE Paper No. 083339. St. Joseph, Mich.: ASABE.

Liu, C. Y., Q. Zhang, and Y Chen. 2008b. PFC3D simulation of lateral pressures in model bins. *ASABE* Paper No. 083340. St. Joseph, MI: ASABE.

Liu C., Q. Zhang and Y. Chen. 2010. Discrete element simulations of vibration characteristics of bulk grain in storage bins, *Transactions of the ASABE*, 53: 1653-1659.

Ljung, A. L. V. Frishfelds, T. S. Lundstrom, and B. D. Marjavaara. 2012. Discrete and continuous modeling of heat and mass transport in drying of a bed of iron ore pellets. *Drying Technology,* 30(7): 760-773.

Lopez et al, X. P. H. Valvatne, and M. J. Blunt. 2003; Predictive network modeling of single-phase non-Newtonian flow in porous media. *Journal of Colloid Interface Science*, 264: 256-265.

Løvoll, G., Y. Meheust, K. J. Maløy, E. Aker, and J. Schmittbuhl. 2005. Competition of gravity, capillary and viscous forces during drainage in a two- dimensional porous medium, a pore scale study. *Energy*, 30(6): 861-872.

Lukaszuk. J., M. Molenda, J. Horabik, B. Szot, and M.D. Montross. 2008. Airflow resistance of wheat bedding as influenced by the filling method. Resource of Agriculture Engineering, (2): 50-57.

Madamba P. S., R. H. Driscoll, and K. A. Buckle. 1993. Bulk density, porosity and resistance to airflow of garlic slices. *Drying technology*,11(7): 1837-1854.

Marousis, S. N., and G. D. Saravacos. 2006. Density and porosity in drying starch materials. *Journal of food science*, 55(5): 1367-1327.

Mason, G., and D. W. Mellor .1991. Analysis of the percolation properties of a real porous medium. Characterization of Porous Solids Ⅱ, F. Rodriquez-Reinoso et al., eds., Elsevier, Amsterdam, 41.

Matteis, M. 1969. Donnes Techniques su la Ventilation du Grain. Centre National d' Etudes et d'Experimentation de Machinisme Agricole.

Matyka, M., A. Khalili, and Z. Koza. 2008. Tortuosity-porosity relation in the porous media flow. *Physical Review E*, 78(2), 1-8.

McDonald, F., M. S. Ei-Sayed, K. Mow, and F. A. L. Dullien. 1979. Flow through porous media-the Ergun equation revisited. *Ind. Eng. Chem. Fundam*, 18 (3): 199-208.

McEwen, E., W. H. C. Simmonds, and G. T. Ward. 1954. The drying of wheatgrain: Part IV: The resistance to air flow of beds of agricultural products. *Experimental work. Transactions of the Institution of Chemical Engineering*, 32(2): 121-129.

Mohanty, K. K., & Salter, S. J. 1982. Multiphase flow in porous media: II. pore-level modeling, SPE, 11018, Proc. Annual Fall Technical Conference of the SPE-AIME, 26-29, New Orleans.

Mohsenin, N. N. 1980. Physical Properties of Plant and Animal Materials. Third Edition, *Gordon and Breach Science Publisher*, New York, NY.

Molenda, M. D. Montross, S. G. McNeill and Horabik. J. 2005. Airflow reisstance of seeds at different bulk densities using Ergun's Equation. *Transactions of ASAE*, 48(3): 1137-1145.

Mukhopadhyay, S., and G. C. Layek. 2012. Effect of variable fluid viscosity on flow past a heated stretching sheet embedded in a porous medium in presence of heat source/sink. *Meccanica*, 47(4): 863-876.

Monga, O., F. N. Ngom, and J. F. Delerue. 2007. Representing geometric structures in 3D tomography soil images: Application to pore-space modeling. *Computers & Geosciences*, 33: 1140-1161.

Montross, M. D., and S. G. McNeill .2005. Permeability of corn soybeans and soft red and white winter wheat as affected by bulk density. *Applied Engineering in Agriculture*, 21(3): 479-484.

Morais, A. F., H. Seybold, H. J. Herrmann, and J. S. Andrade Jr. 2009. Non-Newtonian fluid flow through three-dimensional disordered porous media. Physics Rev Lett, 103(19):

194502.

Nalladurai, K., K. Alagusundaram, and P. Gayathri. 2002. Airflow resistance of paddy and its byproducts. *Biosystems Engineering*, 83(1):67-75.

Nasiru, A. I. 2009. Pore-scale modeling: Stochastic network generation and Modeling of rate effects in waterflooding. Ph.D thesis, Imperial College London.

Neethirajan, S., and D. S. Jayas. 2008. Analysis of pore network in three dimensional (3D) grain bulks using X-ray CT images. *Transport in Porous Media* 73(3): 319-332.

Nemec, D., and J. Levec. 2005. Flow through packed bed reactors: 1. Single-phase flow. *Chemical Engineering Science*, 60(24): 6947-6957.

Neethirajan, S., C. Karunakaran. D. S. Jayas and N. D. G. White. 2006. X-ray computed tomography image analysis to explain the airflow resistance differences in grain bulks. *Biosystems Engineering* 94(4), 545-555.

Nimkar, P. M., and P. K. Chattopadhyay. 2002.Airflow resistance of green gram. Biosystems Engineering: 82 (4): 407-414.

Nowak E.R., J. B. Knight. E. Ben-Naim. H. M. Jaeger and S. R. Nagel. 1998. Density fluctuations in vibrated granular materials, *Physical Review E*, 57: 1971-1982.

Nwaizu C. (2013). Characterizing airflow paths in grain bulks. Ph.D thesis. University of Manitoba.

Nwaizu C. and Q. Zhang. 2015. Characterizing tortuous airflow paths in a grain bulk by using smoke visualization, *Canadian Biosystems Engineering*, 57: 3.13-13.22.

Okura, Y., H. Ochiai, P. A. Cundall, and Y. Shimizu. 2004.Fluid coupling in PFC3D using the measure spheres. Numerical modeling in micromechanics via particle methods,

proceedings of the 2nd international PFC symposium, Kyoto, Japan, 257-264.

Ostermeier, R. M. 1995. Stressed oil permeability of deepwater gulf of Mexico turbidite sands: Measurements and theory. SPE 30606 prepared for presentation at the 70th ATCE of SPE, Dallas, TX.

Pagano, A. M., D. E. Crozza, and S. M. Nolasco. Pressure drop through in-bulk flax seeds. *Journal of American Oil Chemists*, 75(12): 1741-1747.

Panda, M. N., and L. W. Lake .1994. Estimation of single-phase permeability from parameters of particle-size distribution. *AAPG Bulletin*, 78(7): 1028-1039.

Pathak, P., P. H. Winterfeld, H. T. Davis, and L. E. Scriven. 1980. Rock structure and transport therein: unifying with Voronoi models and percolation concepts. First Joint SPE/DOE/Symp. on Enhanced Oil Recovery, Tulsa, Okalahoma.

Pisani L. 2011. Simple expression for the tortuosity of porous media. *Transport in Porous Media*, 88: 193-203.

Rajabipour, A., F. Shahbazi, S. Mohtasebi, and A. Tabatabaeefar. 2001. Airflow resistance in walnuts. Journal of *Agriculture Science and Technology*, 3(4): 257-264.

Rapusas, H. R., D. G. Bottrell, and M. Coll. 1995.

Ray, S. J., L. O. Pordesimo, and L. R. Wilhelm. 2004. Airflow resistance of some pelleted feed. *Transactions of ASAE*, 47(2):513-519.

Rhodes, M. 2008. Introduction to particles technology, 2nd Edition. John Wiley & Sons Ltd. West Susex, England.

Sacilik. K. 2004. Resistance of bulk poppy seeds to airflow. *Biosystems Engineering*, 89(4): 435-443.

Sangani, A. S., and A. Acrivos 1982. Slow flow through a periodic array of spheres. *International Journal of Multiphase Flow*, 8(4): 343-360.

Shahbazi, F. 2011. Resistance of bulk chickpea seeds to airflow. Journal of *Agriculture Science and Technology*, 13: 665-676.

Shedd, C. K. 1945. Resistance of ear corn to air flow. *Agricultural Engineering*, 26(1): 19-23.

Shedd, C. K. 1953. Resistance of grains and seeds to airflow. *Agricultural Engineering* 33(9),616-619.

Shimizu, Y., R. Hart, and P. Cundall. 2004. Numerical modeling in micromechanics via particle methods: Proceedings of the 2nd international PFC symposium, Taylor & Francis, London, UK.

Siebenmorgen, T. J., and V. K. Jindal. 1987. Airflow resistance of rough rice as affected by moisture content, fines concentration and bulk density. *Transactions of the ASAE, 30(4): 1138-1143.*

Sobieski, W., Q. Zhang, and C. Liu. 2012. Predicting tortuosity foe airflow path through porous beds consisting of randomly packed spherical particles. *Transport in Porous Media*, 93(3): 431-451.

Sokhansanj, S., D. S. Jayas, and A. A. Falachinski. 1988. Resistance of bulk lentils to airflow. Paper 88-6535. *ASABE*. St. Joseph.MI. 23 pp.

Sokhansanj, S., W. Li, and O. O. Fasina. 1993. Resistance of alfalfa cubes, pellets, and compressed herbage to airflow. *Canadian Agricultural Engineering.* 35(3): 207-213.

Stirniman, E.J., Bodnar G.P and Bates, E.N. 1931. Tests on resistance to the passage of air through rough rice in a deep bin. *Agricultural Engineering*, 12(5): 145-148

Surasani, V. K., T. Metzger. and E. Tsotsas. 2010. Drying simulations of various 3D pore structures by a nonisothermal pore network model. *Drying Technology*, 28(5): 615-623.

Sutera, S. P., and R. Skalak 1993. The history of Poiseuille's law. Annual Review of Fluid Mechanics 25,1-19.

Thompson, M T., & Hjortso, M. 2007. Coulping pore-scale networks to continuum-scale models of porous media. Computers and Geosciences, 33(3): 393-410.

Thompson, K. E., & Fogler, H. S. 1997. Modeling flow in disordered packed beds from pore-scale fluid mechanics. AIChE journal, 43(6): 1377-1389.

Thompson, K.E. 2002. Pore-scale modeling of fluid trnasport in disordered fibrous materials. Fluid Mechanics and Transport Phenomena, 48(7): 1369-1389.

Thompson R. A. and Isaacs G. W. 1967. Porosity Determinations of Grains and Seeds with an Air-Comparison Pycnometer. Transactions of ASAE, 693-696.

Vallabh, R., P. Banls-Lee and A.F. Seyam. 2010. New Approach for Determining Tortuosity in Fibrous Porous Media. *Journal of Engineered Fibers and Fibrics*, 5(3): 7-15.

Valvatne, P. H., & Blunt, M. J. 2004. Predictive pore-scale modeling of two-phase flow in mixed wet media. Water Resources Research, 40(7), W07406, DOI: 10.1029/2003WR002627.

Vrettos, N. A., H. Imakoma, and M. Okazaki. 1989. Transport properties of porous media from the microgeometry of a three-dimensional voronoi network. *Chem, Eng, Process*, 26: 237-246.

Wang, Y. J., A. Kharaghani, T. Metzger, and E. Tsotsas. 2012. Pore network drying model for particle aggregates: Assessment by X-ray microtomography. *Drying Technology*,

30(15): 1800-1809.

Watson, D. F. 1981. Coumputering the n-dimensional delaunay tessellation with application to voronoi polytopes.*The Computer Journal*, 24(2): 167-172.

Webb. P. A. 2001. Volume and Density Determination for Particle Technologists. Micrometrics Instrument Corp.

Winterfeld, P. H., L. E. Scriven, and H. T. Davis. 1981. Percolation and conduction of two-dimensional composites. *Journal of Physics C*, 14(17): 2361-2376.

Wu, J. and S. Yin. 2009. A micro-mechanism model for porous media. Commun. Theor. Phys, 52: 936-940.

Wu, J.S., B. M. Yu and M.J. Yun. 2008. A resistance model for flow through porous media. *Transport in Porous Media* 71: 331-343.

Wu, J.S. and S. X. Yin. 2009. A novel method for tortuous streamtubes in porous media. Flow in Porous Media-Phenomena to Engineering and Beyond Conference Paper from 2009 International Forum on Porous Flow and Applications, Wuhan City, China.

Wu, J. S., B. M. Yu and M. J. Yun. 2008. A resistance model for flow through porous media. *Transport in Porous Media* 71(3): 331-343.

Xiao, Z. D., Yang. Y. Yuan. B. Yang and X. Liu. 2008. Fractal pore network simulation on the drying of porous media. *Drying technology*, 26: 651-665.

Xiao, Z. F., D. Y. Yang. Y .J. Yuan. B. B. Yang and X. D. Liu. 2008. Fractal pore network simulation on the drying of porous media. *Drying Technology*, 26: 651-665.

Yiotis, A. G., I. N. Tsimpanogiannis. and A. K. Stubos. 2010. Fractal characteristics and scaling of the drying front in porous media: A pore network study. *Drying Technology*,

28(8): 981-990.

Yue, R., and Q. Zhang. 2013. Modeling airflow path through grain bulks using the discrete element method. CSBE Paper No. 13-031. Winnipeg, MB.: CSBE.

Yu, B. M., and J.H. Li. 2004. A Geometry Model for Tortuosity of Streamlines in Porous Media. *Chinese Physical Latters* 21(8), 1569-1571.

Yu B M. 2008.Analysis of Flow in Fractal Porous Media.Applied Mechanics Reviews 61(5). doi:10.1115/1.2955849.

Yun, M. J., B. M. Yu, B. Zhang, and M. T. Huang. 2005. A Geometry Model for Tortuosity of Streamlines in Porous Media with Sphere Particles. *Chinese Physical Latters* 22(6), 1464-1467.

Yun, M. J., Y. Yue, B. M. Yu, J. D. Lu, and W. Zhang. 2010. A Geometry Model for Tortuosity of Streamlines in Porous Media with Cylindrical Particles. *Chinese Physical Latters* 27(10), 104704-1-104704-4.

Zhang, T., D. Li, J. Yang, and D. Lu. 2013. A study of the effect of pore characteristics on permeability with a pore network model. *Petroleum Science and Technology*, 31(17): 1790-1796.

Appendix A. PFC^{3D} Code for Simulating Rectangular Grain Bed

```
;fname: test1.dat
new
set random

def assemble
 width = 0.25 ;
 height = 0.25 ;
 depth = 0.02 ;
 tot_vol = width*height*depth
 oo=out(string(tot_vol))
 rlo=0.00275
 rhi=0.00375
 poros = 0.408
 r0 = 0.5 * (rlo + rhi)
 num = int((1.0 - poros) * tot_vol / (4.0/3.0*pi*r0^3))
 mult = 1.4
 rlo_0=rlo/mult
 rhi_0=rhi/mult
 command
 wall id=1 kn=1.8e7 ks=0.9e7 fric 0.3 face -0.125,-0.01,0   -0.125,-0.01,0.25  0.125,-0.01,0.25
0.125,-0.01,0
 wall id=2 kn=1.8e7 ks=0.9e7 fric 0.3 face 0.125,-0.01,0    0.125,-0.01,0.25   0.125,0.01,0.25
0.125,0.01,0
 wall id=3 kn=1.8e7 ks=0.9e7 fric 0.3 face 0.125,0.01,0  0.125,0.01,0.25   -0.125,0.01,0.25
-0.125,0.01,0
 wall id=4 kn=1.8e7 ks=0.9e7 fric 0.3 face -0.125,0.01,0 -0.125,0.01,0.25  -0.125,-0.01,0.25
-0.125,-0.01,0
 wall id=5 kn=1.8e7 ks=0.9e7 fric 0.3 face -0.125,-0.01,0.25       -0.125,0.01,0.25
0.125,0.01,0.25  0.125,-0.01,0.25
 wall id=6 kn=1.8e7 ks=0.9e7 fric 0.3 face -0.125,-0.01,0     0.125,-0.01,0     0.125,0.01,0
-0.125,0.01,0
 end_command

 command
   generate  id=1,num rad=rlo_0,rhi_0  x= -0.125, 0.125 y= -0.01, 0.01 z= 0, 0.25 tries 200000
   property density 1285 kn 4.0e6 ks 2.0e6 fric 0.47
 end_command
```

```
 ii=out(string(num)+' particles were created')
 sum = 0.0
 bp = ball_head
 loop while bp # null
   sum = sum + (4.0/3.0) * pi * b_rad(bp)^3
   bp = b_next(bp)
 end_loop
 pmeas = 1.0 - sum / tot_vol
 mult=((1.0 - poros) / (1.0 - pmeas))^(1.0/3.0)
 command
  ini rad mul mult
  set grav 0.0 0.0 -9.81
  cycle 3000
 end_command

 sum = 0.0
 bp = ball_head
 loop while bp # null
 sum = sum + (4.0/3.0) * pi * b_rad(bp)^3
 bp = b_next(bp)
 end_loop
 pmeas1 = 1.0 - sum / tot_vol
 mult = ((1.0 - poros)/ (1.0 - pmeas1))^(1.0/3.0)
end

macro zero'ini xvel 0 yvel 0 zvel 0 xspin 0 yspin 0 zspin'
 ; set damping
damp default local 0.0
damp default viscous normal 0.1 notens on
damp default viscous shear 0.1

assemble
print ball position
print measures ball
print pmeas
print pmeas1
solve

delete wall 1 2 3 4 5
 wall id=7 kn=1.8e7 ks=0.9e7 fric 0.3 face -0.125,-0.01,0 -0.125,-0.01,0.275
0.125,-0.01,0.275 0.125,-0.01,0
 wall id=8 kn=1.8e7 ks=0.9e7 fric 0.3 face 0.125,-0.01,0 0.125,-0.01,0.275 0.125,0.01,0.275
0.125,0.01,0
 wall id=9 kn=1.8e7 ks=0.9e7 fric 0.3 face 0.125,0.01,0 0.125,0.01,0.275 -0.125,0.01,0.275
```

-0.125,0.01,0
wall id=10 kn=1.8e7 ks=0.9e7 fric 0.3 face -0.125,0.01,0 -0.125,0.01,0.275 -0.125,-0.01,0.275 -0.125,-0.01,0
wall id=11 kn=1.8e7 ks=0.9e7 fric 0.3 face -0.125,-0.01,0.275 -0.125,0.01,0.275 0.125,0.01,0.275 0.125,-0.01,0.275

return

Appendix B. PFC^{3D} Code for Simulating Cylindrical Grain Bed

```
; fname: vib3d_assem.dat; part 1; "Soybean, size 0.25mX0.15m"
; vibrating simulation
; making assembly

set logfile vib3d_assem.log
set log on
new
set random

;----------
def set_prop
  kn_b   = 4.0e6
  ks_b   = 2.0e6
  kn_w   = 1.8e7   ;Plexiglass E=3034MPa,thin 6mm
  ks_w   = 0.9e7
  dens_b = 1285.0
  fric_b = 0.47
  fric_w = 0.3
end

set_prop

;------------
; make_walls
;------------
def make_walls
  k = 5.5      ;Thickness of sensor is 5.5 time of particle diameter
  extend = 0.0
  rbar = 0.5 * (rlo + rhi)
  height1=height+0.05
  _z0 = -extend
  _z13 = height1

command
    wall type cylinder id=1 kn=kn_w ks=ks_w fric fric_w end1 0.0 0.0 _z0 end2 0.0 0.0 _z13 &
    rad rad_cy rad_cy
```

```
end_command

  _x0 = -rad_cy*(1.0 + extend)
  _y0 = -rad_cy*(1.0 + extend)
  _z0 = 0.0
  _x1 =  rad_cy*(1.0 + extend)
  _y1 = -rad_cy*(1.0 + extend)
  _z1 = 0.0
  _x2 =  rad_cy*(1.0 + extend)
  _y2 =  rad_cy*(1.0 + extend)
  _z2 = 0.0
  _x3 = -rad_cy*(1.0 + extend)
  _y3 =  rad_cy*(1.0 + extend)
  _z3 = 0.0
  command
    wall id=16 kn=kn_w ks=ks_w fric fric_w face (_x0,_y0,_z0) (_x1,_y1,_z1) &
                       (_x2,_y2,_z2) (_x3,_y3,_z3)
  end_command

  _x0 = -rad_cy*(1.0 + extend)
  _y0 = -rad_cy*(1.0 + extend)
  _z0 = height1
  _x1 = -rad_cy*(1.0 + extend)
  _y1 =  rad_cy*(1.0 + extend)
  _z1 = height1
  _x2 =  rad_cy*(1.0 + extend)
  _y2 =  rad_cy*(1.0 + extend)
  _z2 = height1
  _x3 =  rad_cy*(1.0 + extend)
  _y3 = -rad_cy*(1.0 + extend)
  _z3 = height1
  command
    wall id=17 kn=kn_w ks=ks_w fric fric_w face (_x0,_y0,_z0) (_x1,_y1,_z1) &
                       (_x2,_y2,_z2) (_x3,_y3,_z3)
  end_command

 end
;-------------
; ff_cylinder
;-------------
def ff_cylinder
  ff_cylinder = 0
  _brad = fc_arg(0)
  _bx   = fc_arg(1)
```

```
  _by   = fc_arg(2)
  _bz   = fc_arg(3)
  _rad  = sqrt(_bx^2 + _by^2)
  if _rad + _brad > rad_cy then
    ff_cylinder = 1
  end_if
end
;----------
; assemble
;----------
def assemble
  rad_cy = 0.5*width
  _rad_cy = -rad_cy

  tot_vol = height * pi * rad_cy^2.0
  oo = out(string(tot_vol))
  rbar    = 0.5 * (rlo + rhi)
  num     = int((1.0 - poros) * tot_vol / (4.0/3.0*pi*rbar^3))

  mult    = 1.4
  rlo_0   = rlo / mult
  rhi_0   = rhi / mult
  make_walls
  command
    gen id=1,num rad=rlo_0,rhi_0 x=_rad_cy,rad_cy y=_rad_cy,rad_cy &
       z=0,height filter ff_cylinder tries 230000
    prop dens=dens_b kn=kn_b ks=ks_b fric fric_b
  end_command

 ii = out(string(num)+' particles were created')
  sum = 0.0 ; get actual porosity before multipling radius
  bp  = ball_head
  loop while bp # null
    sum = sum + pi * 4.0 / 3.0 * b_rad(bp)^3
    bp  = b_next(bp)
  end_loop
  pmeas = 1.0 - sum / tot_vol
  mult = ((1.0 - poros) / (1.0 - pmeas))^(1.0/3.0)
command
    ini rad mul mult
    cycle 3000
end_command
```

```
;
; get actual porosity after multipling radius
sum = 0.0 ; get actual porosity
  bp  = ball_head
  loop while bp # null
    sum = sum + pi * 4.0 / 3.0 * b_rad(bp)^3
    bp  = b_next(bp)
  end_loop
  pmeas1 = 1.0 - sum / tot_vol
  mult = ((1.0 - poros) / (1.0 - pmeas))^(1.0/3.0)
;
end

;------------
; plot_view1
;------------
def plot_view1
  command
    title 'Vibrating Simulation : PFC3D'
    plot create makingAssembly
    plot set title text 'Making Assembly'
    plot set rot 0 0 0
    ;plot set rot 20 0 0
    plot set caption size 30
    plot set background white
    plot add ax brown
    plot add wall wireframe on
    plot add ball yellow; id on
    plot add measure blue
    ;plot his 1
    plot show
  end_command
end
;--------------------------- MAIN ROUTINE ----------------------------
macro zero ini xvel 0 yvel 0 zvel 0 xspin 0 yspin 0 zspin 0
; set damping
damp default local 0.0
damp default viscous normal 0.1 notens on
damp default viscous shear 0.1
;
; set dimensions & condition to make
set height=0.275 width=0.154 rlo=0.00275 rhi=0.00375 poros=0.408
set grav 0.0 0.0 -9.81
;
```

```
assemble

plot_view1
plot show
print pmeas
print pmeas1
print measures ball

solve
save vib3d_assem.sav
set log off
return
```

Appendix C. PFC^{3D} Code for Simulating Vibration of Cylindrical Grain Bed

1. To make the assembly of grain bed before vibration

```
; fname: vib3d_assem.dat; part 1; "Soybean, size 0.25mX0.15m"
; vibrating simulation
; making assembly

set logfile vib3d_assem.log
set log on
new
set random

;----------
def set_prop
  kn_b   = 4.0e6
  ks_b   = 2.0e6
  kn_w   = 1.8e7   ;Plexiglass E=3034MPa,thin 6mm
  ks_w   = 0.9e7
  dens_b = 1285.0
  fric_b = 0.47
  fric_w = 0.3
end

set_prop

;------------
; make_walls
;------------
def make_walls
  k = 5.5      ;Thickness of sensor is 5.5 time of particle diameter
  extend = 0.0
  rbar = 0.5 * (rlo + rhi)
  height1=height+0.05
  _z0 = -extend
  _z13 = height1

command
    wall type cylinder id=1 kn=kn_w ks=ks_w fric fric_w end1 0.0 0.0 _z0 end2 0.0 0.0 _z13 &
    rad rad_cy rad_cy
```

```
end_command

  _x0 = -rad_cy*(1.0 + extend)
  _y0 = -rad_cy*(1.0 + extend)
  _z0 = 0.0
  _x1 =  rad_cy*(1.0 + extend)
  _y1 = -rad_cy*(1.0 + extend)
  _z1 = 0.0
  _x2 =  rad_cy*(1.0 + extend)
  _y2 =  rad_cy*(1.0 + extend)
  _z2 = 0.0
  _x3 = -rad_cy*(1.0 + extend)
  _y3 =  rad_cy*(1.0 + extend)
  _z3 = 0.0
  command
    wall id=16 kn=kn_w ks=ks_w fric fric_w face (_x0,_y0,_z0) (_x1,_y1,_z1) &
                       (_x2,_y2,_z2) (_x3,_y3,_z3)
  end_command

  _x0 = -rad_cy*(1.0 + extend)
  _y0 = -rad_cy*(1.0 + extend)
  _z0 = height1
  _x1 = -rad_cy*(1.0 + extend)
  _y1 =  rad_cy*(1.0 + extend)
  _z1 = height1
  _x2 =  rad_cy*(1.0 + extend)
  _y2 =  rad_cy*(1.0 + extend)
  _z2 = height1
  _x3 =  rad_cy*(1.0 + extend)
  _y3 = -rad_cy*(1.0 + extend)
  _z3 = height1
  command
    wall id=17 kn=kn_w ks=ks_w fric fric_w face (_x0,_y0,_z0) (_x1,_y1,_z1) &
                       (_x2,_y2,_z2) (_x3,_y3,_z3)
  end_command

end
;-------------
; ff_cylinder
;-------------
def ff_cylinder
  ff_cylinder = 0
```

```
  _brad = fc_arg(0)
  _bx   = fc_arg(1)
  _by   = fc_arg(2)
  _bz   = fc_arg(3)
  _rad  = sqrt(_bx^2 + _by^2)
  if _rad + _brad > rad_cy then
    ff_cylinder = 1
  end_if
end
;----------
; assemble
;----------
def assemble
  rad_cy = 0.5*width
  _rad_cy = -rad_cy

  tot_vol = height * pi * rad_cy^2.0
  oo = out(string(tot_vol))
  rbar    = 0.5 * (rlo + rhi)
  num     = int((1.0 - poros) * tot_vol / (4.0/3.0*pi*rbar^3))

  mult    = 1.5
  rlo_0   = rlo / mult
  rhi_0   = rhi / mult
  make_walls
  command
    gen id=1,num rad=rlo_0,rhi_0 x=_rad_cy,rad_cy y=_rad_cy,rad_cy &
       z=0,height filter ff_cylinder tries 230000
    prop dens=dens_b kn=kn_b ks=ks_b fric fric_b
  end_command

ii = out(string(num)+' particles were created')
  sum = 0.0 ; get actual porosity before multipling radius
  bp  = ball_head
  loop while bp # null
    sum = sum + pi * 4.0 / 3.0 * b_rad(bp)^3
    bp  = b_next(bp)
  end_loop
  pmeas = 1.0 - sum / tot_vol
  mult = ((1.0 - poros) / (1.0 - pmeas))^(1.0/3.0)
command
    ini rad mul mult
    cycle 2000
end_command
```

```
; get actual porosity after multipling radius
sum = 0.0 ; get actual porosity
  bp  = ball_head
  loop while bp # null
    sum = sum + pi * 4.0 / 3.0 * b_rad(bp)^3
    bp  = b_next(bp)
  end_loop
  pmeas1 = 1.0 - sum / tot_vol
  mult = ((1.0 - poros) / (1.0 - pmeas))^(1.0/3.0)
;
end


;--------------------------- MAIN ROUTINE ----------------------------
macro zero 'ini xvel 0 yvel 0 zvel 0 xspin 0 yspin 0 zspin 0'
; set damping
set damp local 0.0
set damp viscous normal 0.1
set damp viscous shear  0.1
set damp viscous not on
;
; set dimensions & condition to make
set height=0.25 width=0.15 rlo=0.00275 rhi=0.00375 poros=0.408
set grav 0.0 0.0 -9.81
;
assemble

print pmeas
print pmeas1

solve
save vib3d_assem.sav
set log off
return
```

2. To initial the state of grain bed before vibration

```
; fname: vib3d_init.dat; part2
; vibrating simulation
; creation initial stage
set logfile vib3d_init.log
set log on
```

```
new
restore vib3d_assem.SAV
;----------
; init_val
;----------
def init_val
  z0 = 0.0
end
init_val

;measure initial bulk particle height
; -------------------------------------------
def bulkheight
bht=0
bp = ball_head
loop while bp # null
_zb = b_z(bp)
_zbm = max(_zb,bht)
bht = _zbm
bp = b_next(bp)
end_loop
bhtf=bht+rbar
end
; -------------------------------------------
bulkheight

; ---------------------------------------------------------------
;get anytime porosity etc. at measurement sphere during vibration
; -------------------------------------------------
def make_measc

; setup measurement sphere at different height
meas_r = width/14.0
meas_x = 3.0/7.0*width
meas_y = 0.0*width
meas_z = 0.146
command
measure id=1 x = meas_x y = meas_y z = meas_z rad = meas_r
end_command
;
meas_r = width/14.0
meas_x = 3.0/7.0*width
meas_y = 0.0*width
meas_z = 0.130
```

```
command
measure id=2 x = meas_x y = meas_y z = meas_z rad = meas_r
end_command
;

meas_r = width/14.0
meas_x = 3.0/7.0*width
meas_y = 0.0*width
meas_z = 0.119
command
measure id=3 x = meas_x y = meas_y z = meas_z rad = meas_r
end_command
;

meas_r = width/14.0
meas_x = 3.0/7.0*width
meas_y = 0.0*width
meas_z = 0.129
command
measure id=4 x = meas_x y = meas_y z = meas_z rad = meas_r
end_command
;

meas_r = width/14.0
meas_x = 3.0/7.0*width
meas_y = 0.0*width
meas_z = 0.136
command
measure id=5 x = meas_x y = meas_y z = meas_z rad = meas_r
end_command
;

mp1 = find_meas(1)
mp2 = find_meas(2)
mp3 = find_meas(3)
mp4 = find_meas(4)
mp5 = find_meas(5)

;
end
; ---------------------------------------------------------------
make_measc
;
```

```
;--------------------------- MAIN ROUTINE ----------------------------
macro zero 'ini xvel 0 yvel 0 zvel 0 xspin 0 yspin 0 zspin 0'
prop kn kn_b ks ks_b dens dens_b fric fric_b
;set gw_cellmap on
wall prop kn kn_w ks ks_w fric fric_w

print measure 1
print measure 2
print measure 3
print measure 4
print measure 5


print bhtf


delete wall 17
save vib3d_init.sav
plot show
set log off
return
```

3. To vibrate the grain bed at certain vibrating frequency and amplitude

```
; fname: vib3d_vvibrate.dat; vertical vibrating; part 3
; vibrating simulation (3D)

set logfile vibration1mm15Hz.log
set log on
new
restore vib3d_init.sav
;-----------
; set_time
;-----------
def set_time
  time0 = time
end
;----------
; set_wvel
;----------
def set_wvel
  if chk_cnt < 100
    chk_cnt = chk_cnt + 1
```

```
    exit
  end_if
  chk_cnt = 0
  ttime = time - time0
  omega = 2*pi*f
  wvz = A*width*omega*cos(omega*ttime)    ;wall velocity in z direction
  wdz = A*width*sin(omega*ttime)          ;wall displacement in z direction


  ;give velocity for all wall in z direction
  wp = wall_head
  loop while wp # null
  if ttime<16
    w_zvel(wp) = wvz
    else
   w_zvel(wp) = 0.0
   endif
   wp = w_next(wp)
  end_loop
end


his measure porosity id=1          ;1
his measure porosity id=2          ;2
his measure porosity id=3          ;3
his measure porosity id=4          ;4
his measure porosity id=5          ;5


hist ttime    ;6

;----------
; run_time
;----------
def run_time
  total_time = 16 + time  ; until 1s
  command
    solve time total_time av 0.0 max 0.0
  end_command
end

;--------------------------- MAIN ROUTINE ----------------------------
set_time
set dt 3.3e-06
```

```
set chk_cnt = 0
set fishcall 0 set_wvel

;
;plot cur 1
plot set caption off
set hist_rep 200
plot_view2

set plot avi size 800 600
movie avi_open file vibration1mm15Hz.avi
movie step 5000 1 file vibration1mm15Hz.avi
run_time
movie avi_close file vibration1mm15Hz.avi
save vibration1mm15Hz.sav
; Write out contents of history 1 2 3.
hist write 6 1 2 3 4 5 file porosity.his
hist write 6 7 8 9 10 11 12 13 14 15 16 file zpos.his
hist write 6 17 18 19 20 21 22 23 24 25 26 file zvel.his
set log off
return
```

Appendix D. Matlab Algorithm For Calculating the Widest Airflow Path and Tortuosities

```
% seek the ID number of the lowest ball
n=1;
for n=1:5146
   distance(n,1)=ball(n,1);%% assign the ID number to the first column of 'dsitance' matrix
   if n==1
      ballZ=[];
       ballZ=ball(1,4);
       else if n>1
           ballZ=[ballZ;ball(n,4)];
       end
   end
   [Zmin,idZmin]=min(ballZ); %% seek the ID number of the lowest ball(idZmin)
end

%% calculate the distance from the idZmin to others
n=1;
for n=1:5146

distance(n,2)=(((ball(n,2)-ball(idZmin,2))^2+(ball(n,3)-ball(idZmin,3))^2+(ball(n,4)-ball(idZ
min,4))^2))^(0.5);%% assign the distance from the lowest to others to the second column of
"distance" matrix
   distancesorted=sortrows(distance,2);%% sort the distance
   n=n+1;
end



xtime=1;
distancesorted(1,:)=[];
datastore=[4825 4186 308] %%save three balls that are shorest to the lowest ball in the
"datastore" matrix.
ar=1
%B12=((ball(distancesorted(1,1),2)-ball(distancesorted(2,1),2))^2+(ball(distancesorted(1,1),3
)-ball(distancesorted(2,1),3))^2+(ball(distancesorted(1,1),4)-ball(distancesorted(2,1),4))^2)^(
0.5)
%B13=((ball(distancesorted(1,1),2)-ball(distancesorted(3,1),2))^2+(ball(distancesorted(1,1),3
)-ball(distancesorted(3,1),3))^2+(ball(distancesorted(1,1),4)-ball(distancesorted(3,1),4))^2)^(
0.5)
%B23=((ball(distancesorted(2,1),2)-ball(distancesorted(3,1),2))^2+(ball(distancesorted(2,1),3
```

```
)-ball(distancesorted(3,1),3))^2+(ball(distancesorted(2,1),4)-ball(distancesorted(3,1),4))^2)^(
0.5)

%% the iteration algorithm to calculate the fourth ball and the three balls
%% as the next base triangle


for mo=1:5
  DT1=[]
  %iddot=[];
   [r,c]=size(datastore); %% calculate the number of row and column of "datastore" matrix.
   if r==1
      xc=(ball(datastore(1,1),2)+ball(datastore(1,2),2)+ball(datastore(1,3),2))/3
      yc=(ball(datastore(1,1),3)+ball(datastore(1,2),3)+ball(datastore(1,3),3))/3
      zc=(ball(datastore(1,1),4)+ball(datastore(1,2),4)+ball(datastore(1,3),4))/3 %% calculating
the centroid of the first base triangle.
      %lave=(((ball(datastore(1,1),2)-ball(datastore(1,2),2))^2+(ball(datastore(1,1),3)-ball(data
store(1,2),3))^2+(ball(datastore(1,1),4)-ball(datastore(1,2),4))^2)^(0.5)+((ball(datastore(1,1),
2)-ball(datastore(1,3),2))^2+(ball(datastore(1,1),3)-ball(datastore(1,3),3))^2+(ball(datastore(1
,1),4)-ball(datastore(1,3),4))^2)^(0.5)+((ball(datastore(1,2),2)-ball(datastore(1,3),2))^2+(ball(
datastore(1,2),3)-ball(datastore(1,3),3))^2+(ball(datastore(1,2),4)-ball(datastore(1,3),4))^2)^(
0.5))/3;
   end
   if r>1
     xc=(ball(datastore(r,1),2)+ball(datastore(r,2),2)+ball(datastore(r,3),2))/3
     yc=(ball(datastore(r,1),3)+ball(datastore(r,2),3)+ball(datastore(r,3),3))/3
     zc=(ball(datastore(r,1),4)+ball(datastore(r,2),4)+ball(datastore(r,3),4))/3  %% calculating
the centroid of the next base triangle.
     %lave=(((ball(datastore(r,1),2)-ball(datastore(r,2),2))^2+(ball(datastore(r,1),3)-ball(datast
ore(r,2),3))^2+(ball(datastore(r,1),4)-ball(datastore(r,2),4))^2)^(0.5)+((ball(datastore(r,1),2)-b
all(datastore(r,3),2))^2+(ball(datastore(r,1),3)-ball(datastore(r,3),3))^2+(ball(datastore(r,1),4)-
ball(datastore(r,3),4))^2)^(0.5)+((ball(datastore(r,2),2)-ball(datastore(r,3),2))^2+(ball(datastor
e(r,2),3)-ball(datastore(r,3),3))^2+(ball(datastore(r,2),4)-ball(datastore(r,3),4))^2)^(0.5))/3;
   end
   m=1
   n=1;
   bz=0;
   for n=1:5146
        a=1;
        b=1;
        for a=1:r
           for b=1:3
               if ball(n,1)~=datastore(a,b) %% judge n equals the data in  "datastore" matrix. if it
has been saved, bz=bz+1;
```

```
                if ball(n,1)~=idZmin
                  bz=bz+1;
                end
              end
              b=b+1;
            end
            a=a+1;
         end

        %% judge it satisfy the condition to be as the fourth ball
         if bz==r*3 %% n has not been saved
           bz=0;
            if ball(n,4)> zc
                DT=((ball(n,2)-xc)^2+(ball(n,3)-yc)^2+(ball(n,4)-zc)^2)^(0.5)
                DT1(m,2)=[DT]
                DT1(m,1)=n
                %%iddot=iddot+1;
                m=m+1
                n=n+1
            end
         end
         if bz~=r*3
            bz=0;
         end
    end
    DTsorted=sortrows(DT1,2);
    mdt=DTsorted(1,1)

      %% seek all the possible triangles that may be the next base
      %% triangle.
     %%m=1
     E=[];
```

L11=((ball(mdt,2)-ball(datastore(r,1),2))^2+(ball(mdt,3)-ball(datastore(r,1),3))^2+(ball(mdt,4)-ball(datastore(r,1),4))^2)^(0.5);%% calculate the length of side composed by iddot(xtime) and n1.

L12=((ball(mdt,2)-ball(datastore(r,2),2))^2+(ball(mdt,3)-ball(datastore(r,2),3))^2+(ball(mdt,4)-ball(datastore(r,2),4))^2)^(0.5);%% calculate the length of side composed by iddot(xtime) and n2.

B12=((ball(datastore(r,1),2)-ball(datastore(r,2),2))^2+(ball(datastore(r,1),3)-ball(datastore(r,2),3))^2+(ball(datastore(r,1),4)-ball(datastore(r,2),4))^2)^(0.5);%% calculate the length of side composed by n1 and n2.

C1=L11+L12+B12

A112=acos((L11^2+L12^2-B12^2)/(2*L11*L12))
B112=acos((L11^2+B12^2-L12^2)/(2*L11*B12))
B121=acos((L12^2+B12^2-L11^2)/(2*L12*B12))

SA112=A112*(ball(mdt,5))^2*(1/2)
SB112=B112*(ball(datastore(r,1),5))^2*(1/2)
SB121=B121*(ball(datastore(r,2),5))^2*(1/2)

ai1=sqrt((C1/2)*(C1/2-L11)*(C1/2-L12)*(C1/2-B12))-SA112-SB112-SB121%% calculate the area that is composed by the three vertex iddot(xtime)、n1 and n2.

zc1=(ball(datastore(r,1),4)+ball(datastore(r,2),4)+ball(mdt,4))/3

%if sqrt((C1/2)*(C1/2-L11)*(C1/2-L12)*(C1/2-B12))<A0 || sqrt((C1/2)*(C1/2-L11)*(C1/2-L12)*(C1/2-B12))>Acr
%ai1=0
%end

L13=((ball(mdt,2)-ball(datastore(r,3),2))^2+(ball(mdt,3)-ball(datastore(r,3),3))^2+(ball(mdt,4)-ball(datastore(r,3),4))^2)^(0.5);%% calculate the length of side composed by iddot(xtime) and n3.

B13=((ball(datastore(r,1),2)-ball(datastore(r,3),2))^2+(ball(datastore(r,1),3)-ball(datastore(r,3),3))^2+(ball(datastore(r,1),4)-ball(datastore(r,3),4))^2)^(0.5);%% calculate the length of side composed by n1 and n3.

C2=L11+L13+B13;

A113=acos((L11^2+L13^2-B13^2)/(2*L11*L13))
B113=acos((L11^2+B13^2-L13^2)/(2*L11*B13))
B131=acos((L13^2+B13^2-L11^2)/(2*L13*B13))

SA113=A113*(ball(mdt,5))^2*(1/2)
SB113=B113*(ball(datastore(r,1),5))^2*(1/2)
SB131=B131*(ball(datastore(r,3),5))^2*(1/2)

ai2=sqrt((C2/2)*(C2/2-L11)*(C2/2-L13)*(C2/2-B13))-SA113-SB113-SB131%% calculate the area that is composed by the three vertex iddot(xtime)、n1 and n3.

zc2=(ball(datastore(r,1),4)+ball(datastore(r,3),4)+ball(mdt,4))/3

%if sqrt((C2/2)*(C2/2-L11)*(C2/2-L13)*(C2/2-B13))<A0 ||

```
sqrt((C2/2)*(C2/2-L11)*(C2/2-L13)*(C2/2-B13))>Acr
          %ai2=0
        %end


B23=((ball(datastore(r,2),2)-ball(datastore(r,3),2))^2+(ball(datastore(r,2),3)-ball(datastore(r,3
),3))^2+(ball(datastore(r,2),4)-ball(datastore(r,3),4))^2)^(0.5);%% calculate the length of side
composed by n2 and n3.
        C3=L12+L13+B23;

        A213=acos((L12^2+L13^2-B23^2)/(2*L12*L13))
        B123=acos((L12^2+B23^2-L13^2)/(2*L12*B23))
        B132=acos((L13^2+B23^2-L12^2)/(2*L13*B23))

        SA213=A213*(ball(mdt,5))^2*(1/2)
        SB123=B123*(ball(datastore(r,2),5))^2*(1/2)
        SB132=B132*(ball(datastore(r,3),5))^2*(1/2)

        ai3=sqrt((C3/2)*(C3/2-L12)*(C3/2-L13)*(C3/2-B23))-SA213-SB123-SB132%%
calculate the area that is composed bt the three vertex iddot(xtime)、n2 and n3.

        zc3=(ball(datastore(r,2),4)+ball(datastore(r,3),4)+ball(mdt,4))/3


       %if                sqrt((C3/2)*(C3/2-L12)*(C3/2-L13)*(C3/2-B23))<A0                ||
sqrt((C3/2)*(C3/2-L12)*(C3/2-L13)*(C3/2-B23))>Acr
          %ai3=0
        %end

B23=((ball(datastore(r,3),2)-ball(datastore(r,2),2))^2+(ball(datastore(r,3),3)-ball(datastore(r,2
),3))^2+(ball(datastore(r,3),4)-ball(datastore(r,2),4))^2)^(0.5);
         C4=B12+B13+B23
         B213=acos((B12^2+B13^2-B23^2)/(2*B12*B13))
         B123=acos((B12^2+B23^2-B13^2)/(2*B12*B23))
         B132=acos((B13^2+B23^2-B12^2)/(2*B13*B23))
         SB213=B213*(ball(datastore(r,1),5))^2*(1/2)
         SB123=B123*(ball(datastore(r,2),5))^2*(1/2)
         SB132=B132*(ball(datastore(r,3),5))^2*(1/2)
         ai4=sqrt((C4/2)*(C4/2-B12)*(C4/2-B13)*(C4/2-B23))-SB213-SB123-SB132

       if ai1<0 || ai2<0 || ai3<0
        mdt=DTsorted(2,1)

L11=((ball(mdt,2)-ball(datastore(r,1),2))^2+(ball(mdt,3)-ball(datastore(r,1),3))^2+(ball(mdt,4
```

)-ball(datastore(r,1),4))^2)^(0.5);%% calculate the length of side composed by iddot(xtime) and n1.

L12=((ball(mdt,2)-ball(datastore(r,2),2))^2+(ball(mdt,3)-ball(datastore(r,2),3))^2+(ball(mdt,4)-ball(datastore(r,2),4))^2)^(0.5);%% calculate the length of side composed by iddot(xtime) and n2.

B12=((ball(datastore(r,1),2)-ball(datastore(r,2),2))^2+(ball(datastore(r,1),3)-ball(datastore(r,2),3))^2+(ball(datastore(r,1),4)-ball(datastore(r,2),4))^2)^(0.5);%% calculate the length of side composed by n1 and n2.

C1=L11+L12+B12;

A112=acos((L11^2+L12^2-B12^2)/(2*L11*L12))
B112=acos((L11^2+B12^2-L12^2)/(2*L11*B12))
B121=acos((L12^2+B12^2-L11^2)/(2*L12*B12))

SA112=A112*(ball(mdt,5))^2*(1/2)
SB112=B112*(ball(datastore(r,1),5))^2*(1/2)
SB121=B121*(ball(datastore(r,2),5))^2*(1/2)

ai1=sqrt((C1/2)*(C1/2-L11)*(C1/2-L12)*(C1/2-B12))-SA112-SB112-SB121%% calculate the area that is composed by the three vertex iddot(xtime)、n1 and n2.

zc1=(ball(datastore(r,1),4)+ball(datastore(r,2),4)+ball(mdt,4))/3

%if sqrt((C1/2)*(C1/2-L11)*(C1/2-L12)*(C1/2-B12))<A0 || sqrt((C1/2)*(C1/2-L11)*(C1/2-L12)*(C1/2-B12))>Acr
%ai1=0
%end

L13=((ball(mdt,2)-ball(datastore(r,3),2))^2+(ball(mdt,3)-ball(datastore(r,3),3))^2+(ball(mdt,4)-ball(datastore(r,3),4))^2)^(0.5);%% calculate the length of side composed by iddot(xtime) and n3.

B13=((ball(datastore(r,1),2)-ball(datastore(r,3),2))^2+(ball(datastore(r,1),3)-ball(datastore(r,3),3))^2+(ball(datastore(r,1),4)-ball(datastore(r,3),4))^2)^(0.5);%% calculate the length of side composed by n1 and n3.

C2=L11+L13+B13;

A113=acos((L11^2+L13^2-B13^2)/(2*L11*L13))
B113=acos((L11^2+B13^2-L13^2)/(2*L11*B13))
B131=acos((L13^2+B13^2-L11^2)/(2*L13*B13))

SA113=A113*(ball(mdt,5))^2*(1/2)

```
SB113=B113*(ball(datastore(r,1),5))^2*(1/2)
SB131=B131*(ball(datastore(r,3),5))^2*(1/2)

ai2=sqrt((C2/2)*(C2/2-L11)*(C2/2-L13)*(C2/2-B13))-SA113-SB113-SB131%% calculate the area that is composed by the three vertex iddot(xtime)、n1 and n3.

zc2=(ball(datastore(r,1),4)+ball(datastore(r,3),4)+ball(mdt,4))/3

%if sqrt((C2/2)*(C2/2-L11)*(C2/2-L13)*(C2/2-B13))<A0 || sqrt((C2/2)*(C2/2-L11)*(C2/2-L13)*(C2/2-B13))>Acr
  %ai2=0
%end

B23=((ball(datastore(r,2),2)-ball(datastore(r,3),2))^2+(ball(datastore(r,2),3)-ball(datastore(r,3),3))^2+(ball(datastore(r,2),4)-ball(datastore(r,3),4))^2)^(0.5);%% calculate the length of side composed by n2 and n3.
C3=L12+L13+B23;

A213=acos((L12^2+L13^2-B23^2)/(2*L12*L13))
B123=acos((L12^2+B23^2-L13^2)/(2*L12*B23))
B132=acos((L13^2+B23^2-L12^2)/(2*L13*B23))

SA213=A213*(ball(mdt,5))^2*(1/2)
SB123=B123*(ball(datastore(r,2),5))^2*(1/2)
SB132=B132*(ball(datastore(r,3),5))^2*(1/2)

ai3=sqrt((C3/2)*(C3/2-L12)*(C3/2-L13)*(C3/2-B23))-SA213-SB123-SB132%% calculate the area that is composed bt the three vertex iddot(xtime)、n2 and n3.

zc3=(ball(datastore(r,2),4)+ball(datastore(r,3),4)+ball(mdt,4))/3

%if sqrt((C3/2)*(C3/2-L12)*(C3/2-L13)*(C3/2-B23))<A0 || sqrt((C3/2)*(C3/2-L12)*(C3/2-L13)*(C3/2-B23))>Acr
  %ai3=0
%end

B23=((ball(datastore(r,3),2)-ball(datastore(r,2),2))^2+(ball(datastore(r,3),3)-ball(datastore(r,2),3))^2+(ball(datastore(r,3),4)-ball(datastore(r,2),4))^2)^(0.5);
C4=B12+B13+B23
B213=acos((B12^2+B13^2-B23^2)/(2*B12*B13))
B123=acos((B12^2+B23^2-B13^2)/(2*B12*B23))
B132=acos((B13^2+B23^2-B12^2)/(2*B13*B23))
SB213=B213*(ball(datastore(r,1),5))^2*(1/2)
SB123=B123*(ball(datastore(r,2),5))^2*(1/2)
```

```
    SB132=B132*(ball(datastore(r,3),5))^2*(1/2)
    ai4=sqrt((C4/2)*(C4/2-B12)*(C4/2-B13)*(C4/2-B23))-SB213-SB123-SB132

  end
    ratio=(ai1+ai2+ai3)/ai4
    A=[ai1 ai2 ai3 ai4 ratio]
    if ar==1
      areastore=[A];
      else if ar>1
            areastore=[areastore;A];
      end
    end
    ar=ar+1;
   if zc1<zc|| zc1==zc
      ai1=0;
   end

   if zc2<zc|| zc2==zc
      ai2=0;
   end

   if zc3<zc|| zc3==zc
      ai3=0;
   end

   S=[ai1 ai2 ai3];

   %[H,L]=size(S); %% return the number of rows and columns of S matrix.

   %[rows2,cols2]=find(S==max(max(S))); %%seek the position of the biggest area of three side areas.

   [Y,I]=max(S,[],2)
   %if ratio>5
     %[Y,I]=max([zc1 zc2 zc3],[],2)
   %end

   S=[];
   if I==1   %% judge which area composed by iddot(xtime) and three base vertexes equals the maximum area.
     E=[datastore(r,1) datastore(r,2) mdt];
   end
   if I==2
     E=[datastore(r,1) datastore(r,3) mdt];
```

```
        end
        if I==3
          E=[datastore(r,2) datastore(r,3) mdt];
        end
        datastore=[datastore;E]  %%save the three vertexes in "datastore" matrix to renew it.
 mo=mo+1
end
%% calculating the centroid of each base triangle.
for i=1:r
    datastore(i,4)=(ball(datastore(i,1),2)+ball(datastore(i,2),2)+ball(datastore(i,3),2))/3;
    datastore(i,5)=(ball(datastore(i,1),3)+ball(datastore(i,2),3)+ball(datastore(i,3),3))/3;
    datastore(i,6)=(ball(datastore(i,1),4)+ball(datastore(i,2),4)+ball(datastore(i,3),4))/3;
    i=i+1;
end
for i=1:r
   x(i)=datastore(i,4);
   y(i)=datastore(i,5);
   z(i)=datastore(i,6);
   i=i+1;
end
plot3(x,y,z)
hold on
for i=1:5146
   u(i)=ball(i,2);
   v(i)=ball(i,3);
   w(i)=ball(i,4);
   i=i+1;
end
plot3(u,v,w,'g.')

%% cacaulate the tortuosity of airflow path.
for i=1:r-1
   De(i)=sqrt((x(i+1)-x(i))^2+(y(i+1)-y(i))^2+(z(i+1)-z(i))^2);
   Le=sum(De,2);
   i=i+1;
end
for i=1:r-1

   i= i+1;
end

%% caculate the totuosity
T=Le/(max(ballZ)-min(ballZ)+0.0065)
```

```
%% Smooth the path.

for i=2:r-1
   e(i-1)=sqrt((x(i-1)-x(i))^2+(y(i-1)-y(i))^2+(z(i-1)-z(i))^2);
   f(i-1)=sqrt((x(i+1)-x(i))^2+(y(i+1)-y(i))^2+(z(i+1)-z(i))^2);
   g(i-1)=sqrt((x(i+1)-x(i-1))^2+(y(i+1)-y(i-1))^2+(z(i+1)-z(i-1))^2);
   ww(i-1)=(((e(i-1))^2+(f(i-1))^2-(g(i-1))^2)/(2*(e(i-1))*(f(i-1))))*(180/3.14);
   if ww(i-1)<0
     ww(i-1)=180+ww(i-1);
   end
end

SHS=0;
for i=1:r-2
      wcor(i)=(exp(0.1*(ww(i)-90)))/(1+exp(0.1*(ww(i)-90)));
      HS(i)=(1/2)*(e(i)+f(i))*wcor(i);
      SHS=sum(HS,2);
end

Lecor=(1/2)*(e(1)+f(r-2))+SHS;
Tcor=Lecor/(max(ballZ)-min(ballZ)+0.0065)
```

Appendix E. Matlab Algorithm for Calculating the Narrowest Airflow Path and Tortuosities

```
% seek the ID number of the lowest ball
n=1;
for n=1:5146
   distance(n,1)=ball(n,1);%% assign the ID number to the first column of 'dsitance' matrix
   if n==1
     ballZ=[];
      ballZ=ball(1,4);
      else if n>1
          ballZ=[ballZ;ball(n,4)];
      end
   end
   [Zmin,idZmin]=min(ballZ); %% seek the ID number of the lowest ball(idZmin)
end

%% calculate the distance from the idZmin to others
n=1;
for n=1:5146

distance(n,2)=(((ball(n,2)-ball(idZmin,2))^2+(ball(n,3)-ball(idZmin,3))^2+(ball(n,4)-ball(idZ
min,4))^2))^(0.5);%% assign the distance from the lowest to others to the second column of
"distance" matrix
   distancesorted=sortrows(distance,2);%% sort the distance
   n=n+1;
end

xtime=1;
distancesorted(1,:)=[];
datastore=[1605 4105 3590] %%save three balls that are shorest to the lowest ball in the
"datastore" matrix.
ar=1
%B12=((ball(distancesorted(1,1),2)-ball(distancesorted(2,1),2))^2+(ball(distancesorted(1,1),3
)-ball(distancesorted(2,1),3))^2+(ball(distancesorted(1,1),4)-ball(distancesorted(2,1),4))^2)^(
0.5)
%B13=((ball(distancesorted(1,1),2)-ball(distancesorted(3,1),2))^2+(ball(distancesorted(1,1),3
)-ball(distancesorted(3,1),3))^2+(ball(distancesorted(1,1),4)-ball(distancesorted(3,1),4))^2)^(
0.5)
%B23=((ball(distancesorted(2,1),2)-ball(distancesorted(3,1),2))^2+(ball(distancesorted(2,1),3
)-ball(distancesorted(3,1),3))^2+(ball(distancesorted(2,1),4)-ball(distancesorted(3,1),4))^2)^(
```

```
0.5)

%% the iteration algorithm to calculate the fourth ball and the three balls
%% as the next base triangle

for mo=1:5
  DT1=[]
  %iddot=[];
   [r,c]=size(datastore); %% calculate the number of row and column of "datastore" matrix.
   if r==1
     xc=(ball(datastore(1,1),2)+ball(datastore(1,2),2)+ball(datastore(1,3),2))/3
     yc=(ball(datastore(1,1),3)+ball(datastore(1,2),3)+ball(datastore(1,3),3))/3
     zc=(ball(datastore(1,1),4)+ball(datastore(1,2),4)+ball(datastore(1,3),4))/3 %% calculating
the centroid of the first base triangle.
      %lave=(((ball(datastore(1,1),2)-ball(datastore(1,2),2))^2+(ball(datastore(1,1),3)-ball(data
store(1,2),3))^2+(ball(datastore(1,1),4)-ball(datastore(1,2),4))^2)^(0.5)+((ball(datastore(1,1),
2)-ball(datastore(1,3),2))^2+(ball(datastore(1,1),3)-ball(datastore(1,3),3))^2+(ball(datastore(1
,1),4)-ball(datastore(1,3),4))^2)^(0.5)+((ball(datastore(1,2),2)-ball(datastore(1,3),2))^2+(ball(
datastore(1,2),3)-ball(datastore(1,3),3))^2+(ball(datastore(1,2),4)-ball(datastore(1,3),4))^2)^(
0.5))/3;
   end
   if r>1
     xc=(ball(datastore(r,1),2)+ball(datastore(r,2),2)+ball(datastore(r,3),2))/3
     yc=(ball(datastore(r,1),3)+ball(datastore(r,2),3)+ball(datastore(r,3),3))/3
     zc=(ball(datastore(r,1),4)+ball(datastore(r,2),4)+ball(datastore(r,3),4))/3  %% calculating
the centroid of the next base triangle.
     %lave=(((ball(datastore(r,1),2)-ball(datastore(r,2),2))^2+(ball(datastore(r,1),3)-ball(datast
ore(r,2),3))^2+(ball(datastore(r,1),4)-ball(datastore(r,2),4))^2)^(0.5)+((ball(datastore(r,1),2)-b
all(datastore(r,3),2))^2+(ball(datastore(r,1),3)-ball(datastore(r,3),3))^2+(ball(datastore(r,1),4)-
ball(datastore(r,3),4))^2)^(0.5)+((ball(datastore(r,2),2)-ball(datastore(r,3),2))^2+(ball(datastor
e(r,2),3)-ball(datastore(r,3),3))^2+(ball(datastore(r,2),4)-ball(datastore(r,3),4))^2)^(0.5))/3;
   end
   m=1
   n=1;
   bz=0;
   for n=1:5146
        a=1;
        b=1;
        for a=1:r
           for b=1:3
               if ball(n,1)~=datastore(a,b) %% judge n equals the data in  "datastore" matrix. if it
has been saved, bz=bz+1;
                  if ball(n,1)~=idZmin
                    bz=bz+1;
```

```
            end
          end
          b=b+1;
        end
        a=a+1;
      end

     %% judge it satisfy the condition to be as the fourth ball
      if bz==r*3 %% n has not been saved
        bz=0;
        if ball(n,4)> zc
            DT=((ball(n,2)-xc)^2+(ball(n,3)-yc)^2+(ball(n,4)-zc)^2)^(0.5)
            DT1(m,2)=[DT]
            DT1(m,1)=n
            %%iddot=iddot+1;
            m=m+1
            n=n+1
        end
      end
      if bz~=r*3
         bz=0;
      end
  end
  DTsorted=sortrows(DT1,2);
  mdt=DTsorted(1,1)

   %% seek all the possible triangles that may be the next base
   %% triangle.
  %%m=1
  E=[];
```

L11=((ball(mdt,2)-ball(datastore(r,1),2))^2+(ball(mdt,3)-ball(datastore(r,1),3))^2+(ball(mdt,4)-ball(datastore(r,1),4))^2)^(0.5);%% calculate the length of side composed by iddot(xtime) and n1.

L12=((ball(mdt,2)-ball(datastore(r,2),2))^2+(ball(mdt,3)-ball(datastore(r,2),3))^2+(ball(mdt,4)-ball(datastore(r,2),4))^2)^(0.5);%% calculate the length of side composed by iddot(xtime) and n2.

B12=((ball(datastore(r,1),2)-ball(datastore(r,2),2))^2+(ball(datastore(r,1),3)-ball(datastore(r,2),3))^2+(ball(datastore(r,1),4)-ball(datastore(r,2),4))^2)^(0.5);%% calculate the length of side composed by n1 and n2.

```
      C1=L11+L12+B12
```

```
A112=acos((L11^2+L12^2-B12^2)/(2*L11*L12))
B112=acos((L11^2+B12^2-L12^2)/(2*L11*B12))
B121=acos((L12^2+B12^2-L11^2)/(2*L12*B12))

SA112=A112*(ball(mdt,5))^2*(1/2)
SB112=B112*(ball(datastore(r,1),5))^2*(1/2)
SB121=B121*(ball(datastore(r,2),5))^2*(1/2)

ai1=sqrt((C1/2)*(C1/2-L11)*(C1/2-L12)*(C1/2-B12))-SA112-SB112-SB121%% calculate the area that is composed by the three vertex iddot(xtime)、n1 and n2.

zc1=(ball(datastore(r,1),4)+ball(datastore(r,2),4)+ball(mdt,4))/3

%if sqrt((C1/2)*(C1/2-L11)*(C1/2-L12)*(C1/2-B12))<A0 || sqrt((C1/2)*(C1/2-L11)*(C1/2-L12)*(C1/2-B12))>Acr
  %ai1=0
%end

L13=((ball(mdt,2)-ball(datastore(r,3),2))^2+(ball(mdt,3)-ball(datastore(r,3),3))^2+(ball(mdt,4)-ball(datastore(r,3),4))^2)^(0.5);%% calculate the length of side composed by iddot(xtime) and n3.

B13=((ball(datastore(r,1),2)-ball(datastore(r,3),2))^2+(ball(datastore(r,1),3)-ball(datastore(r,3),3))^2+(ball(datastore(r,1),4)-ball(datastore(r,3),4))^2)^(0.5);%% calculate the length of side composed by n1 and n3.
C2=L11+L13+B13;

A113=acos((L11^2+L13^2-B13^2)/(2*L11*L13))
B113=acos((L11^2+B13^2-L13^2)/(2*L11*B13))
B131=acos((L13^2+B13^2-L11^2)/(2*L13*B13))

SA113=A113*(ball(mdt,5))^2*(1/2)
SB113=B113*(ball(datastore(r,1),5))^2*(1/2)
SB131=B131*(ball(datastore(r,3),5))^2*(1/2)

ai2=sqrt((C2/2)*(C2/2-L11)*(C2/2-L13)*(C2/2-B13))-SA113-SB113-SB131%% calculate the area that is composed by the three vertex iddot(xtime)、n1 and n3.

zc2=(ball(datastore(r,1),4)+ball(datastore(r,3),4)+ball(mdt,4))/3

%if sqrt((C2/2)*(C2/2-L11)*(C2/2-L13)*(C2/2-B13))<A0 || sqrt((C2/2)*(C2/2-L11)*(C2/2-L13)*(C2/2-B13))>Acr
  %ai2=0
%end
```

B23=((ball(datastore(r,2),2)-ball(datastore(r,3),2))^2+(ball(datastore(r,2),3)-ball(datastore(r,3),3))^2+(ball(datastore(r,2),4)-ball(datastore(r,3),4))^2)^(0.5);%% calculate the length of side composed by n2 and n3.

C3=L12+L13+B23;

A213=acos((L12^2+L13^2-B23^2)/(2*L12*L13))
B123=acos((L12^2+B23^2-L13^2)/(2*L12*B23))
B132=acos((L13^2+B23^2-L12^2)/(2*L13*B23))

SA213=A213*(ball(mdt,5))^2*(1/2)
SB123=B123*(ball(datastore(r,2),5))^2*(1/2)
SB132=B132*(ball(datastore(r,3),5))^2*(1/2)

ai3=sqrt((C3/2)*(C3/2-L12)*(C3/2-L13)*(C3/2-B23))-SA213-SB123-SB132%% calculate the area that is composed bt the three vertex iddot(xtime)、n2 and n3.

zc3=(ball(datastore(r,2),4)+ball(datastore(r,3),4)+ball(mdt,4))/3

%if sqrt((C3/2)*(C3/2-L12)*(C3/2-L13)*(C3/2-B23))<A0 || sqrt((C3/2)*(C3/2-L12)*(C3/2-L13)*(C3/2-B23))>Acr
%ai3=0
%end

B23=((ball(datastore(r,3),2)-ball(datastore(r,2),2))^2+(ball(datastore(r,3),3)-ball(datastore(r,2),3))^2+(ball(datastore(r,3),4)-ball(datastore(r,2),4))^2)^(0.5);
C4=B12+B13+B23
B213=acos((B12^2+B13^2-B23^2)/(2*B12*B13))
B123=acos((B12^2+B23^2-B13^2)/(2*B12*B23))
B132=acos((B13^2+B23^2-B12^2)/(2*B13*B23))
SB213=B213*(ball(datastore(r,1),5))^2*(1/2)
SB123=B123*(ball(datastore(r,2),5))^2*(1/2)
SB132=B132*(ball(datastore(r,3),5))^2*(1/2)
ai4=sqrt((C4/2)*(C4/2-B12)*(C4/2-B13)*(C4/2-B23))-SB213-SB123-SB132

if ai1<0 || ai2<0 || ai3<0
mdt=DTsorted(2,1)

L11=((ball(mdt,2)-ball(datastore(r,1),2))^2+(ball(mdt,3)-ball(datastore(r,1),3))^2+(ball(mdt,4)-ball(datastore(r,1),4))^2)^(0.5);%% calculate the length of side composed by iddot(xtime) and n1.

L12=((ball(mdt,2)-ball(datastore(r,2),2))^2+(ball(mdt,3)-ball(datastore(r,2),3))^2+(ball(mdt,4)-ball(datastore(r,2),4))^2)^(0.5);%% calculate the length of side composed by iddot(xtime)

and n2.

B12=((ball(datastore(r,1),2)-ball(datastore(r,2),2))^2+(ball(datastore(r,1),3)-ball(datastore(r,2),3))^2+(ball(datastore(r,1),4)-ball(datastore(r,2),4))^2)^(0.5);%% calculate the length of side composed by n1 and n2.

C1=L11+L12+B12;

A112=acos((L11^2+L12^2-B12^2)/(2*L11*L12))
B112=acos((L11^2+B12^2-L12^2)/(2*L11*B12))
B121=acos((L12^2+B12^2-L11^2)/(2*L12*B12))

SA112=A112*(ball(mdt,5))^2*(1/2)
SB112=B112*(ball(datastore(r,1),5))^2*(1/2)
SB121=B121*(ball(datastore(r,2),5))^2*(1/2)

ai1=sqrt((C1/2)*(C1/2-L11)*(C1/2-L12)*(C1/2-B12))-SA112-SB112-SB121%% calculate the area that is composed by the three vertex iddot(xtime)、n1 and n2.

zc1=(ball(datastore(r,1),4)+ball(datastore(r,2),4)+ball(mdt,4))/3

%if sqrt((C1/2)*(C1/2-L11)*(C1/2-L12)*(C1/2-B12))<A0 || sqrt((C1/2)*(C1/2-L11)*(C1/2-L12)*(C1/2-B12))>Acr
%ai1=0
%end

L13=((ball(mdt,2)-ball(datastore(r,3),2))^2+(ball(mdt,3)-ball(datastore(r,3),3))^2+(ball(mdt,4)-ball(datastore(r,3),4))^2)^(0.5);%% calculate the length of side composed by iddot(xtime) and n3.

B13=((ball(datastore(r,1),2)-ball(datastore(r,3),2))^2+(ball(datastore(r,1),3)-ball(datastore(r,3),3))^2+(ball(datastore(r,1),4)-ball(datastore(r,3),4))^2)^(0.5);%% calculate the length of side composed by n1 and n3.

C2=L11+L13+B13;

A113=acos((L11^2+L13^2-B13^2)/(2*L11*L13))
B113=acos((L11^2+B13^2-L13^2)/(2*L11*B13))
B131=acos((L13^2+B13^2-L11^2)/(2*L13*B13))

SA113=A113*(ball(mdt,5))^2*(1/2)
SB113=B113*(ball(datastore(r,1),5))^2*(1/2)
SB131=B131*(ball(datastore(r,3),5))^2*(1/2)

ai2=sqrt((C2/2)*(C2/2-L11)*(C2/2-L13)*(C2/2-B13))-SA113-SB113-SB131%% calculate the area that is composed by the three vertex iddot(xtime)、n1 and n3.

```
zc2=(ball(datastore(r,1),4)+ball(datastore(r,3),4)+ball(mdt,4))/3

%if sqrt((C2/2)*(C2/2-L11)*(C2/2-L13)*(C2/2-B13))<A0 ||
sqrt((C2/2)*(C2/2-L11)*(C2/2-L13)*(C2/2-B13))>Acr
  %ai2=0
%end

B23=((ball(datastore(r,2),2)-ball(datastore(r,3),2))^2+(ball(datastore(r,2),3)-ball(datastore(r,3
),3))^2+(ball(datastore(r,2),4)-ball(datastore(r,3),4))^2)^(0.5);%% calculate the length of side
composed by n2 and n3.
C3=L12+L13+B23;

A213=acos((L12^2+L13^2-B23^2)/(2*L12*L13))
B123=acos((L12^2+B23^2-L13^2)/(2*L12*B23))
B132=acos((L13^2+B23^2-L12^2)/(2*L13*B23))

SA213=A213*(ball(mdt,5))^2*(1/2)
SB123=B123*(ball(datastore(r,2),5))^2*(1/2)
SB132=B132*(ball(datastore(r,3),5))^2*(1/2)

ai3=sqrt((C3/2)*(C3/2-L12)*(C3/2-L13)*(C3/2-B23))-SA213-SB123-SB132%%
calculate the area that is composed bt the three vertex iddot(xtime)、n2 and n3.

zc3=(ball(datastore(r,2),4)+ball(datastore(r,3),4)+ball(mdt,4))/3

%if sqrt((C3/2)*(C3/2-L12)*(C3/2-L13)*(C3/2-B23))<A0 ||
sqrt((C3/2)*(C3/2-L12)*(C3/2-L13)*(C3/2-B23))>Acr
  %ai3=0
%end

B23=((ball(datastore(r,3),2)-ball(datastore(r,2),2))^2+(ball(datastore(r,3),3)-ball(datastore(r,2
),3))^2+(ball(datastore(r,3),4)-ball(datastore(r,2),4))^2)^(0.5);
C4=B12+B13+B23
B213=acos((B12^2+B13^2-B23^2)/(2*B12*B13))
B123=acos((B12^2+B23^2-B13^2)/(2*B12*B23))
B132=acos((B13^2+B23^2-B12^2)/(2*B13*B23))
SB213=B213*(ball(datastore(r,1),5))^2*(1/2)
SB123=B123*(ball(datastore(r,2),5))^2*(1/2)
SB132=B132*(ball(datastore(r,3),5))^2*(1/2)
ai4=sqrt((C4/2)*(C4/2-B12)*(C4/2-B13)*(C4/2-B23))-SB213-SB123-SB132

end
ratio=(ai1+ai2+ai3)/ai4
```

```
 A=[ai1 ai2 ai3 ai4 ratio]
 if ar==1
    areastore=[A];
    else if ar>1
          areastore=[areastore;A];
    end
 end
 ar=ar+1;
if zc1<zc|| zc1==zc
    ai1=0;
end

if zc2<zc|| zc2==zc
    ai2=0;
end

if zc3<zc|| zc3==zc
    ai3=0;
end

S=[ai1 ai2 ai3];

%[H,L]=size(S); %% return the number of rows and columns of S matrix.

%[rows2,cols2]=find(S==max(max(S))); %%seek the position of the biggest area of three side areas.

[Y,I]=min(S,[],2)
%if ratio>5
  %[Y,I]=max([zc1 zc2 zc3],[],2)
%end

S=[];
if I==1   %% judge which area composed by iddot(xtime) and three base vertexes equals the maximum area.
   E=[datastore(r,1) datastore(r,2) mdt];
end
if I==2
   E=[datastore(r,1) datastore(r,3) mdt];
end
if I==3
   E=[datastore(r,2) datastore(r,3) mdt];
end
datastore=[datastore;E]  %%save the three vertexes in "datastore" matrix to renew it.
```

```
 mo=mo+1
end
%% calculating the centroid of each base triangle.
for i=1:r
    datastore(i,4)=(ball(datastore(i,1),2)+ball(datastore(i,2),2)+ball(datastore(i,3),2))/3;
    datastore(i,5)=(ball(datastore(i,1),3)+ball(datastore(i,2),3)+ball(datastore(i,3),3))/3;
    datastore(i,6)=(ball(datastore(i,1),4)+ball(datastore(i,2),4)+ball(datastore(i,3),4))/3;
    i=i+1;
end
for i=1:r
   x(i)=datastore(i,4);
   y(i)=datastore(i,5);
   z(i)=datastore(i,6);
   i=i+1;
end
plot3(x,y,z)
hold on
for i=1:5146
   u(i)=ball(i,2);
   v(i)=ball(i,3);
   w(i)=ball(i,4);
   i=i+1;
end
plot3(u,v,w,'g.')

%% cacaulate the tortuosity of airflow path.
for i=1:r-1
   De(i)=sqrt((x(i+1)-x(i))^2+(y(i+1)-y(i))^2+(z(i+1)-z(i))^2);
   Le=sum(De,2);
   i=i+1;
end
for i=1:r-1

   i= i+1;
end

%% caculate the totuosity
T=Le/(max(ballZ)-min(ballZ)+0.0065)

%% Smooth the path.

for i=2:r-1
   e(i-1)=sqrt((x(i-1)-x(i))^2+(y(i-1)-y(i))^2+(z(i-1)-z(i))^2);
   f(i-1)=sqrt((x(i+1)-x(i))^2+(y(i+1)-y(i))^2+(z(i+1)-z(i))^2);
```

```
   g(i-1)=sqrt((x(i+1)-x(i-1))^2+(y(i+1)-y(i-1))^2+(z(i+1)-z(i-1))^2);
   ww(i-1)=(((e(i-1))^2+(f(i-1))^2-(g(i-1))^2)/(2*(e(i-1))*(f(i-1))))*(180/3.14);
   if ww(i-1)<0
     ww(i-1)=180+ww(i-1);
   end
end

SHS=0;
for i=1:r-2
      wcor(i)=(exp(0.1*(ww(i)-90)))/(1+exp(0.1*(ww(i)-90)));
      HS(i)=(1/2)*(e(i)+f(i))*wcor(i);
      SHS=sum(HS,2);
end

Lecor=(1/2)*(e(1)+f(r-2))+SHS;
Tcor=Lecor/(max(ballZ)-min(ballZ)+0.0065)
```

Appendix F. Matlab Algorithm for Predicting Resistance to Airflow by Branched Model

```
xc=zeros(148,1);
yc=zeros(148,1);
zc=zeros(148,1);
xc1=zeros(148,1);
yc1=zeros(148,1);
zc1=zeros(148,1);
xc2=zeros(148,1);
yc2=zeros(148,1);
zc2=zeros(148,1);
xc3=zeros(148,1);
yc3=zeros(148,1);
zc3=zeros(148,1);
L0=zeros(148,1);
L1=zeros(148,1);
L2=zeros(148,1);
L3=zeros(148,1);
L11=zeros(148,1);
L12=zeros(148,1);
L13=zeros(148,1);
C1=zeros(148,1);
S1=zeros(148,1);
R1=zeros(148,1);
L21=zeros(148,1);
L22=zeros(148,1);
L23=zeros(148,1);
C2=zeros(148,1);
S2=zeros(148,1);
R2=zeros(148,1);
L31=zeros(148,1);
L32=zeros(148,1);
L33=zeros(148,1);
C3=zeros(148,1);
S3=zeros(148,1);
R3=zeros(148,1);
A1=zeros(148,1);
A2=zeros(148,1);
A3=zeros(148,1);
C0=zeros(148,1);
```

```
S0=zeros(148,1);
R0=zeros(148,1);
S=zeros(148,1);
for i=1:148
  xc(i)=(ball(datastore(i,1),2)+ball(datastore(i,2),2)+ball(datastore(i,3),2)+ball(datastore(i+1,3),2))/4;
  yc(i)=(ball(datastore(i,1),3)+ball(datastore(i,2),3)+ball(datastore(i,3),3)+ball(datastore(i+1,3),3))/4;
  zc(i)=(ball(datastore(i,1),4)+ball(datastore(i,2),4)+ball(datastore(i,3),4)+ball(datastore(i+1,3),4))/4;
  xc0(i)=(ball(datastore(i,1),2)+ball(datastore(i,2),2)+ball(datastore(i,3),2))/3;
  yc0(i)=(ball(datastore(i,1),3)+ball(datastore(i,2),3)+ball(datastore(i,3),3))/3;
  zc0(i)=(ball(datastore(i,1),4)+ball(datastore(i,2),4)+ball(datastore(i,3),4))/3;
  xc1(i)=(ball(datastore(i,1),2)+ball(datastore(i,2),2)+ball(datastore(i+1,3),2))/3;
  yc1(i)=(ball(datastore(i,1),3)+ball(datastore(i,2),3)+ball(datastore(i+1,3),3))/3;
  zc1(i)=(ball(datastore(i,1),4)+ball(datastore(i,2),4)+ball(datastore(i+1,3),4))/3;
  xc2(i)=(ball(datastore(i,1),2)+ball(datastore(i,3),2)+ball(datastore(i+1,3),2))/3;
  yc2(i)=(ball(datastore(i,1),3)+ball(datastore(i,3),3)+ball(datastore(i+1,3),3))/3;
  zc2(i)=(ball(datastore(i,1),4)+ball(datastore(i,3),4)+ball(datastore(i+1,3),4))/3;
  xc3(i)=(ball(datastore(i,2),2)+ball(datastore(i,3),2)+ball(datastore(i+1,3),2))/3;
  yc3(i)=(ball(datastore(i,2),3)+ball(datastore(i,3),3)+ball(datastore(i+1,3),3))/3;
  zc3(i)=(ball(datastore(i,2),4)+ball(datastore(i,3),4)+ball(datastore(i+1,3),4))/3;
  L0(i)=((xc0(i)-xc(i))^2+(yc0(i)-yc(i))^2+(zc0(i)-zc(i))^2)^(0.5);
  L1(i)=((xc1(i)-xc(i))^2+(yc1(i)-yc(i))^2+(zc1(i)-zc(i))^2)^(0.5);
  L2(i)=((xc2(i)-xc(i))^2+(yc2(i)-yc(i))^2+(zc2(i)-zc(i))^2)^(0.5);
  L3(i)=((xc3(i)-xc(i))^2+(yc3(i)-yc(i))^2+(zc3(i)-zc(i))^2)^(0.5);

L11(i)=((ball(datastore(i,1),2)-ball(datastore(i+1,3),2))^2+(ball(datastore(i,1),3)-ball(datastore(i+1,3),3))^2
+(ball(datastore(i,1),4)-ball(datastore(i+1,3),4))^2)^(0.5);

L12(i)=((ball(datastore(i,2),2)-ball(datastore(i+1,3),2))^2+(ball(datastore(i,2),3)-ball(datastore(i+1,3),3))^2
+(ball(datastore(i,2),4)-ball(datastore(i+1,3),4))^2)^(0.5);

L13(i)=((ball(datastore(i,1),2)-ball(datastore(i,2),2))^2+(ball(datastore(i,1),3)-ball(datastore(i,2),3))^2+(bal
l(datastore(i,1),4)-ball(datastore(i,2),4))^2)^(0.5);
  C1(i)=L11(i)+L12(i)+L13(i);
  S1(i)=sqrt((C1(i)/2)*(C1(i)/2-L11(i))*(C1(i)/2-L12(i))*(C1(i)/2-L13(i)));
  R1(i)=sqrt(S1(i)/3.14);

A1(i)=180/3.14*acos(((xc(i)-xc0(i))*(xc1(i)-xc(i))+(yc(i)-yc0(i))*(yc1(i)-yc(i))+(zc(i)-zc0(i))*(zc1(i)-zc(i)
))/(sqrt((xc(i)-xc0(i))^2+(yc(i)-yc0(i))^2+(zc(i)-zc0(i))^2)*sqrt((xc1(i)-xc(i))^2+(yc1(i)-yc(i))^2)+(zc1(i)-z
c(i))^2));

L21(i)=((ball(datastore(i,1),2)-ball(datastore(i+1,3),2))^2+(ball(datastore(i,1),3)-ball(datastore(i+1,3),3))^2
+(ball(datastore(i,1),4)-ball(datastore(i+1,3),4))^2)^(0.5);

L22(i)=((ball(datastore(i,3),2)-ball(datastore(i+1,3),2))^2+(ball(datastore(i,3),3)-ball(datastore(i+1,3),3))^2
```

```
+(ball(datastore(i,3),4)-ball(datastore(i+1,3),4))^2)^(0.5);

L23(i)=((ball(datastore(i,1),2)-ball(datastore(i,3),2))^2+(ball(datastore(i,1),3)-ball(datastore(i,3),3))^2+(bal
l(datastore(i,1),4)-ball(datastore(i,3),4))^2)^(0.5);
  C2(i)=L21(i)+L22(i)+L23(i);
  S2(i)=sqrt((C2(i)/2)*(C2(i)/2-L21(i))*(C2(i)/2-L22(i))*(C2(i)/2-L23(i)));
  R2(i)=sqrt(S2(i)/3.14);

A2(i)=180/3.14*acos(((xc(i)-xc0(i))*(xc2(i)-xc(i))+(yc(i)-yc0(i))*(yc2(i)-yc(i))+(zc(i)-zc0(i))*(zc2(i)-zc(i)
))/(sqrt((xc(i)-xc0(i))^2+(yc(i)-yc0(i))^2+(zc(i)-zc0(i))^2)*sqrt((xc2(i)-xc(i))^2+(yc2(i)-yc(i))^2)+(zc2(i)-z
c(i))^2));

L31(i)=((ball(datastore(i,2),2)-ball(datastore(i+1,3),2))^2+(ball(datastore(i,2),3)-ball(datastore(i+1,3),3))^2
+(ball(datastore(i,2),4)-ball(datastore(i+1,3),4))^2)^(0.5);

L32(i)=((ball(datastore(i,3),2)-ball(datastore(i+1,3),2))^2+(ball(datastore(i,3),3)-ball(datastore(i+1,3),3))^2
+(ball(datastore(i,3),4)-ball(datastore(i+1,3),4))^2)^(0.5);

L33(i)=((ball(datastore(i,2),2)-ball(datastore(i,3),2))^2+(ball(datastore(i,2),3)-ball(datastore(i,3),3))^2+(bal
l(datastore(i,2),4)-ball(datastore(i,3),4))^2)^(0.5);
  C3(i)=L31(i)+L32(i)+L33(i);
  S3(i)=sqrt((C3(i)/2)*(C3(i)/2-L31(i))*(C3(i)/2-L32(i))*(C3(i)/2-L33(i)));
  R3(i)=sqrt(S3(i)/3.14);

A3(i)=180/3.14*acos(((xc(i)-xc0(i))*(xc3(i)-xc(i))+(yc(i)-yc0(i))*(yc3(i)-yc(i))+(zc(i)-zc0(i))*(zc3(i)-zc(i)
))/(sqrt((xc(i)-xc0(i))^2+(yc(i)-yc0(i))^2+(zc(i)-zc0(i))^2)*sqrt((xc3(i)-xc(i))^2+(yc3(i)-yc(i))^2)+(zc3(i)-z
c(i))^2));
  C0(i)=L13(i)+L23(i)+L33(i);
  S0(i)=sqrt((C0(i)/2)*(C0(i)/2-L13(i))*(C0(i)/2-L23(i))*(C0(i)/2-L33(i)));
  R0(i)=sqrt(S0(i)/3.14);
  S(i)=S1(i)+S2(i)+S3(i);
  i=i+1

end



S0=17.6130*0.000001
P=zeros(148,1);
P1=zeros(148,1);
PT=0;
PT1=0;

for i=1:148
   Ps(i)=(128*1.932*0.00001*0.05*S0*L0(i))/(3.14*(R0(i)*2)^4);
```

```
Pb1(i)=(4200*(3-2*cos(A1(i)*3.14/180))*1.932*0.00001*0.05*S0*(S1(i)/S(i))*L1(i))/(3.14*((R1(i)*2)^4
));

Pb11(i)=(4200*(2-cos(A1(i)*3.14/180))*1.932*0.00001*0.05*S0*(S1(i)/S(i))*L1(i))/(3.14*((R1(i)*2)^4))
;

Pb2(i)=(4200*(3-2*cos(A2(i)*3.14/180))*1.932*0.00001*0.05*S0*(S2(i)/S(i))*L2(i))/(3.14*((R2(i)*2)^4
));

Pb22(i)=(4200*(2-cos(A2(i)*3.14/180))*1.932*0.00001*0.05*S0*(S2(i)/S(i))*L2(i))/(3.14*((R2(i)*2)^4))
;

Pb3(i)=(4200*(3-2*cos(A3(i)*3.14/180))*1.932*0.00001*0.05*S0*(S3(i)/S(i))*L3(i))/(3.14*((R3(i)*2)^4
));

Pb33(i)=(4200*(2-cos(A3(i)*3.14/180))*1.932*0.00001*0.05*S0*(S3(i)/S(i))*L3(i))/(3.14*((R3(i)*2)^4))
;
   P(i)=Ps(i)+Pb1(i)+Pb2(i)+Pb3(i)
   P1(i)=Ps(i)+Pb11(i)+Pb22(i)+Pb33(i)
   i=i+1
end
for i=1:148
   PT=PT+P(i);
   PT1=PT1+P1(i);
   i=i+1
end
```

Appendix G. Matlab Algorithm for Predicting Resistance To Airflow by Network Model

1. Calculating the fluid conductivity term

```
% import the location coordinates and radius of spheres
x=grains(:,1);
y=grains(:,2);
z=grains(:,3);
r=grains(:,4);

DT=delaunayTriangulation(x,y,z);
tetrahedrons=DT;
% DT will give the vertex id's for the tetrahedrons.

%tetramesh(DT); this will draw the triangulation.

N = neighbors(DT);
neighbours=N;
%To get the neighboring tetrahedrons

% To determine the geometry connectivity
uair=1.932*10^-5;
%uair is the viscosity of the air.

m=119309;
%m=1;
%m is the number of tetrahedrons unit.
s=1;
row=0;
k=zeros(1,4);
l=zeros(1,4);
g=zeros(119309,4);
Qstar=zeros(119309,4);
test=1;
count=47981;

%neighbours=xlsread('neighbours.xlsx');
neighbours(find(isnan(neighbours))) = 0;
%To convert all the NaN values to zero.a

%tetrahedrons=xlsread('tetrahedrons.xlsx');
```

```
%coordinates=xlsread('grains.xlsx');
coordinates=grains;

a=coordinates(:,1);
%a= x coordinates column.

b=coordinates(:,2);
%b= y coordinates column.

c=coordinates(:,3);
%c=z coordinates column.

r=coordinates(:,4);
%r=radius of the spheres.

avgr= 0.003217;
%avarage radius of the grains

b3=[];
b3(1:6,1:3)=1;
b3(7:8,1:3)=48;
b3(9,1:3)=49;
b3(10,1:3)=48;

b4=[];
b4(1,1:4)=1;
b4(2,1)=0;
b4(2,2:4)=1;
b4(3,1:4)=1;
b4(4,1:4)=1;
b4(5,1)=48;
b4(6,1)=48;
b4(5,2:4)=1;
b4(6,2:4)=1;
b4(7,1:4)=48;
b4(8,1:4)=48;
b4(9,1:4)=49;
b4(10,1:4)=48;

b5=[];
b5(1,1:5)=1;
b5(2,1:2)=0;
b5(2,3:5)=1;
```

```
b5(3,1:5)=1;
b5(4,1:5)=1;
b5(5,1:2)=48;
b5(5,3:5)=1;
b5(6,1:2)=48;
b5(6,3:5)=1;
b5(7,1:5)=48;
b5(8,1:5)=48;
b5(9,1:5)=49;
b5(10,1:5)=48;

b6=[];
b6(1,1:6)=1;
b6(2,1:3)=0;
b6(2,4:6)=1;
b6(3,1:6)=1;
b6(4,1:6)=1;
b6(5,1:3)=48;
b6(5,4:6)=1;
b6(6,1:3)=48;
b6(6,4:6)=1;
b6(7,1:6)=48;
b6(8,1:6)=48;
b6(9,1:6)=49;
b6(10,1:6)=48;

B=[1;1;1;1;1;1;48;48;49;48];
b7=[b6 B];
b8=[b7 B];

%b is the boundary conditions matrix. the dimension of boundary condition
%matrix will depend n the number of edges in the geometry. Each column in
%boundary condition matrix define the B.C.'s for one edge.

ns=[];
ns(1,1)= 67;
ns(1,2)= 67;
ns(1,3)= 67;
ns(1,4)= 80;
ns(2,1)= 49;
ns(2,4)= 49;
ns(2,2)= 50;
ns(2,3)= 51;
%creating the ns matrix to deifne the char P1,C1,C2,C3;
```

```
%   sf = charstr('P1-C1-C2-C3');
    %creating character array sf.

gd=[];
%gd is the geometry metrix, which has the number of column same as number
%of elements in the geometry. for our case gd has 4 column, 3 for spheres
%of the face and 1 for the triangle formed by joining the centers of the
%spheres.

gd(1,1)=1;
gd(1,2)=1;
gd(1,3)=1;
% first row- 1 for circle.

gd(1,4)=2;
%first row - 2 for polygon.

gd(2,4)=3;
%no of lines in polygon. in our case triangle=3

for i=47982:m
        row=row+1;
        tetra = neighbours(i,:);
        %tetra = neighbours(m,:);
        % tetra is the matrix (1*4) containing the tetrahedrons id's of the
        % 4 neighbouring tetrahedons.

        vertices= tetrahedrons(i,:);
        %vertices= tetrahedrons(m,:);
        %vertices is the matrix(1*4) containing vertex id's of the father
        %tetrahedron

        for j=1:4
           if tetra(1,j)==0;
           else
              verticesn=tetrahedrons(tetra(1,j),:);
              %verticesn is the matrix(1*4) containing vertex id's of the one of
              %the neighbouring tetrahedrins.
              face= intersect(vertices,verticesn);
              %face matrix is the matrix(1*3) containing the vertex id's of the
              %common face between the neighbouring tetrahedrons.

              x1= coordinates(face(1,1),1);
```

```
y1= coordinates(face(1,1),2);
z1= coordinates(face(1,1),3);
r1= coordinates(face(1,1),4);

x2= coordinates(face(1,2),1);
y2= coordinates(face(1,2),2);
z2= coordinates(face(1,2),3);
r2= coordinates(face(1,2),4);

x3= coordinates(face(1,3),1);
y3= coordinates(face(1,3),2);
z3= coordinates(face(1,3),3);
r3= coordinates(face(1,3),4);

l12=sqrt((x1-x2)^2+(y1-y2)^2+(z1-z2)^2);
l13=sqrt((x1-x3)^2+(y1-y3)^2+(z1-z3)^2);
l23=sqrt((x2-x3)^2+(y2-y3)^2+(z2-z3)^2);

syms u v
[u,v]=solve(sqrt(u^2+v^2)==l13, sqrt((u-l12)^2+v^2)==l23, u,v);
%Transforming the data to 2D. the coordinates in 2D will
%be-(0,0),(l12,0),(u,v)

gd(2,1)= 0;
gd(2,2)= l12/r1;
gd(2,3)= u(1,1)/r1;
gd(3,1)= 0;
gd(3,2)= 0;
gd(3,3)= v(1,1)/r1;
gd(4,1)= r1/r1;
gd(4,2)= r2/r1;
gd(4,3)= r3/r1;
gd(3,4)= 0;
gd(4,4)= l12/r1;
gd(5,4)= u(1,1)/r1;
gd(6,4)= 0;
gd(7,4)= 0;
gd(8,4)= v(1,1)/r1;
%assigning the values to the geometry matrix.
%i
%j
d1=decsg(gd,sf,ns);
%Creating decomposed geometry matrix.
```

```
%pdegplot(d1);
%axis equal

test=test+1;

[p,e,t] = initmesh(d1, 'MesherVersion', 'R2013a');
%[p,e,t]=initmesh(d1);
%this create the initial mesh
%to improve the solution we can use either refine mesh or adapt
%mesh
%[p,e,t]=adaptmesh(d1);
%[p,e,t]=refinemesh(d1);

c=1;
a=0;
f=1;
%c,a,f are the coefficients of the PDE.
n=size(d1,2);
%n is the number of columns in d1 matrix=no. of edges

if n==3
   un=assempde(b3,p,e,t,c,a,f);
else if n==5
   un=assempde(b5,p,e,t,c,a,f);
else if n==4
   un=assempde(b4,p,e,t,c,a,f);
else if n==6
   un=assempde(b6,p,e,t,c,a,f);
else if n==7
   un=assempde(b7,p,e,t,c,a,f);
else if n==8
   un=assempde(b8,p,e,t,c,a,f);
   end
   end
   end
   end
   end
end
pdesurf(p,t,un);
%un is the value of u at each node point.

[ar]=pdetrg(p,t);
%ar is the area of each triangular mesh.
```

```
ut=pdeintrp(p,t,un);
%ut is the value of u at mid-point of each triangle.
q=1;
integeral=0;

while q<(size(ut,2)+1)
%size(ut,2)is the number of volume of ut or the number of triangular mesh.
%q should be smaller than the number of triangular mesh.
multiplication=ut(1,q)*ar(1,q);
%multiplication is the flow rate for each triangular mesh.
integeral=integeral+multiplication;
%integeral is the total flow rate for the total area of each face.
q=q+1;
end

Q= integeral;
k(1,s)=i;
l(1,s)=neighbours(i,j);
L=2*(r1+r2+r3)/3
g(row,s)=Q*(r1^4)/(uair*L);

Qstar(row,s)=Q;
s=s+1;

  end

end
s=1;
count=count+1;
end
```

2. Constructing the linear matrix equation to solve the pressure in each tetrahedron unit

%Add the number of spheres as the first colum of matrix “grains” (119309×5)

```
%select the interior tetrahedrons
i=1;
j=1;
m=1;
for i=1:119309

zc01=(grains(tetrahedrons(i,1),4)+grains(tetrahedrons(i,2),4)+grains(tetrahedrons(i,3),4))/3;
```

```
zc02=(grains(tetrahedrons(i,1),4)+grains(tetrahedrons(i,2),4)+grains(tetrahedrons(i,4),4))/3;

zc03=(grains(tetrahedrons(i,1),4)+grains(tetrahedrons(i,3),4)+grains(tetrahedrons(i,4),4))/3;

zc04=(grains(tetrahedrons(i,2),4)+grains(tetrahedrons(i,3),4)+grains(tetrahedrons(i,4),4))/3;
    zcm=max(zc01,zc02);
    zcm=max(zcm,zc03);
    zcm=max(zcm,zc04);
    zci=min(zc01,zc02);
    zci=min(zci,zc03);
    zci=min(zci,zc04);

xc01=(grains(tetrahedrons(i,1),2)+grains(tetrahedrons(i,2),2)+grains(tetrahedrons(i,3),2))/3;

xc02=(grains(tetrahedrons(i,1),2)+grains(tetrahedrons(i,2),2)+grains(tetrahedrons(i,4),2))/3;

xc03=(grains(tetrahedrons(i,1),2)+grains(tetrahedrons(i,3),2)+grains(tetrahedrons(i,4),2))/3;

xc04=(grains(tetrahedrons(i,2),2)+grains(tetrahedrons(i,3),2)+grains(tetrahedrons(i,4),2))/3;
    xci=min(xc01,xc02);
    xci=min(xci,xc03);
    xci=min(xci,xc04);
    xcm=max(xc01,xc02);
    xcm=max(xcm,xc03);
    xcm=max(xcm,xc04);

yc01=(grains(tetrahedrons(i,1),3)+grains(tetrahedrons(i,2),3)+grains(tetrahedrons(i,3),3))/3;

yc02=(grains(tetrahedrons(i,1),3)+grains(tetrahedrons(i,2),3)+grains(tetrahedrons(i,4),3))/3;

yc03=(grains(tetrahedrons(i,1),3)+grains(tetrahedrons(i,3),3)+grains(tetrahedrons(i,4),3))/3;

yc04=(grains(tetrahedrons(i,2),3)+grains(tetrahedrons(i,3),3)+grains(tetrahedrons(i,4),3))/3;
    yci=min(yc01,yc02);
    yci=min(yci,yc03);
    yci=min(yci,yc04);
    ycm=max(yc01,yc02);
    ycm=max(ycm,yc03);
    ycm=max(ycm,yc04);
    if zcm<0.026 || zci>0.224 || xcm<-0.051 || xci>0.051 || ycm<-0.051  || yci>0.051
      tetraedge(m,1)=i;
      m=m+1;
    end
 i=i+1;
```

```
end

i=1;
j=1;
m=1;
for i=1:119309

zc01=(grains(tetrahedrons(i,1),4)+grains(tetrahedrons(i,2),4)+grains(tetrahedrons(i,3),4))/3;

zc02=(grains(tetrahedrons(i,1),4)+grains(tetrahedrons(i,2),4)+grains(tetrahedrons(i,4),4))/3;

zc03=(grains(tetrahedrons(i,1),4)+grains(tetrahedrons(i,3),4)+grains(tetrahedrons(i,4),4))/3;

zc04=(grains(tetrahedrons(i,2),4)+grains(tetrahedrons(i,3),4)+grains(tetrahedrons(i,4),4))/3;
    zci=min(zc01,zc02);
    zci=min(zci,zc03);
    zci=min(zci,zc04);
    if zci>0.224
      tetraedgein(m,1)=i;
      m=m+1;
    end
 i=i+1;
end

i=1;
j=1;
m=1;
for i=1:119309

xc01=(grains(tetrahedrons(i,1),2)+grains(tetrahedrons(i,2),2)+grains(tetrahedrons(i,3),2))/3;

xc02=(grains(tetrahedrons(i,1),2)+grains(tetrahedrons(i,2),2)+grains(tetrahedrons(i,4),2))/3;

xc03=(grains(tetrahedrons(i,1),2)+grains(tetrahedrons(i,3),2)+grains(tetrahedrons(i,4),2))/3;

xc04=(grains(tetrahedrons(i,2),2)+grains(tetrahedrons(i,3),2)+grains(tetrahedrons(i,4),2))/3;
    xci=min(xc01,xc02);
    xci=min(xci,xc03);
    xci=min(xci,xc04);
    xcm=max(xc01,xc02);
    xcm=max(xcm,xc03);
    xcm=max(xcm,xc04);
    if xcm<-0.051  || xci>0.051
      tetraedgeleft(m,1)=i;
```

```
        m=m+1;
    end
  i=i+1;
end

i=1;
j=1;
m=1;
for i=1:119309

zc01=(grains(tetrahedrons(i,1),4)+grains(tetrahedrons(i,2),4)+grains(tetrahedrons(i,3),4))/3;

zc02=(grains(tetrahedrons(i,1),4)+grains(tetrahedrons(i,2),4)+grains(tetrahedrons(i,4),4))/3;

zc03=(grains(tetrahedrons(i,1),4)+grains(tetrahedrons(i,3),4)+grains(tetrahedrons(i,4),4))/3;

zc04=(grains(tetrahedrons(i,2),4)+grains(tetrahedrons(i,3),4)+grains(tetrahedrons(i,4),4))/3;
    zcm=max(zc01,zc02);
    zcm=max(zcm,zc03);
    zcm=max(zcm,zc04);
    zci=min(zc01,zc02);
    zci=min(zci,zc03);
    zci=min(zci,zc04);

xc01=(grains(tetrahedrons(i,1),2)+grains(tetrahedrons(i,2),2)+grains(tetrahedrons(i,3),2))/3;

xc02=(grains(tetrahedrons(i,1),2)+grains(tetrahedrons(i,2),2)+grains(tetrahedrons(i,4),2))/3;

xc03=(grains(tetrahedrons(i,1),2)+grains(tetrahedrons(i,3),2)+grains(tetrahedrons(i,4),2))/3;

xc04=(grains(tetrahedrons(i,2),2)+grains(tetrahedrons(i,3),2)+grains(tetrahedrons(i,4),2))/3;
    xci=min(xc01,xc02);
    xci=min(xci,xc03);
    xci=min(xci,xc04);
    xcm=max(xc01,xc02);
    xcm=max(xcm,xc03);
    xcm=max(xcm,xc04);

yc01=(grains(tetrahedrons(i,1),3)+grains(tetrahedrons(i,2),3)+grains(tetrahedrons(i,3),3))/3;

yc02=(grains(tetrahedrons(i,1),3)+grains(tetrahedrons(i,2),3)+grains(tetrahedrons(i,4),3))/3;

yc03=(grains(tetrahedrons(i,1),3)+grains(tetrahedrons(i,3),3)+grains(tetrahedrons(i,4),3))/3;
```

```
yc04=(grains(tetrahedrons(i,2),3)+grains(tetrahedrons(i,3),3)+grains(tetrahedrons(i,4),3))/3;
    yci=min(yc01,yc02);
    yci=min(yci,yc03);
    yci=min(yci,yc04);
    ycm=max(yc01,yc02);
    ycm=max(ycm,yc03);
    ycm=max(ycm,yc04);
    if zci>0.026 & zcm<0.224 & xci>-0.051 & xcm<0.051 & yci>-0.051  & ycm<0.051
      tetrainterior(m,1)=i;
      m=m+1;
    end
 i=i+1;
end

 for i=1:51170
   for j=1:4
      tetrainterior(i,j+1)=tetrahedrons(tetrainterior(i),j);
      j=j+1;
   end
   i=i+1;
 end

 i=1;
 m=1;
for i=1:51170
      tetraneighbours(m,:)=neighbours(tetrainterior(i,1),:);
      m=m+1;
      i=i+1;
end

%find the tetrahedrons connected with inlet and outlet
 i=1;
 m=1;
 n=1;
for i=1:51170
   zc01=(grains(tetrainterior(i,2),4)+grains(tetrainterior(i,3),4)+grains(tetrainterior(i,4),4))/3;
   zc02=(grains(tetrainterior(i,2),4)+grains(tetrainterior(i,3),4)+grains(tetrainterior(i,5),4))/3;
   zc03=(grains(tetrainterior(i,2),4)+grains(tetrainterior(i,4),4)+grains(tetrainterior(i,5),4))/3;
   zc04=(grains(tetrainterior(i,3),4)+grains(tetrainterior(i,4),4)+grains(tetrainterior(i,5),4))/3;
   zcm=max(zc01,zc02);
   zcm=max(zcm,zc03);
   zcm=max(zcm,zc04);
   zci=min(zc01,zc02);
   zci=min(zci,zc03);
```

```
    zci=min(zci,zc04);
    if zcm<0.0335
      tetrainteriorin(m,1)=tetrainterior(i,1);
      m=m+1;
    end
    if zcm>0.2185
      tetrainteriorout(n,1)=tetrainterior(i,1);
      n=n+1;
    end
    i=i+1;
end

%generate coefficient matrix A (g)
A=sparse(51170,51170);
for i= 1:51170

D(1,i)=-(g(tetrainterior(i,1),1)+g(tetrainterior(i,1),2)+g(tetrainterior(i,1),3)+g(tetrainterior(i,1)
,4));
    A(i,i)= D(1,i);
    i=i+1;
end

for i=1:51170
    for j=1:4
        [m,n] = find(tetrainterior == neighbours(tetrainterior(i,1),j));
         A(i,m)=g(tetrainterior(i,1),j);
         j=j+1;
    end
   i=i+1;
end

%generate b
b=zeros(51170,1);

%add the constraining equation
A(51171,51171)=0;
for i=1:1348

zc01=(grains(tetrahedrons(tetrainteriorin(i,1),1),4)+grains(tetrahedrons(tetrainteriorin(i,1),2),
4)+grains(tetrahedrons(tetrainteriorin(i,1),3),4))/3;

zc02=(grains(tetrahedrons(tetrainteriorin(i,1),1),4)+grains(tetrahedrons(tetrainteriorin(i,1),2),
4)+grains(tetrahedrons(tetrainteriorin(i,1),4),4))/3;
```

```
zc03=(grains(tetrahedrons(tetrainteriorin(i,1),1),4)+grains(tetrahedrons(tetrainteriorin(i,1),3),
4)+grains(tetrahedrons(tetrainteriorin(i,1),4),4))/3;

zc04=(grains(tetrahedrons(tetrainteriorin(i,1),2),4)+grains(tetrahedrons(tetrainteriorin(i,1),3),
4)+grains(tetrahedrons(tetrainteriorin(i,1),4),4))/3;
   zci=min(zc01,zc02);
   zci=min(zci,zc03);
   zci=min(zci,zc04);
   if zci==zc01
     cf=[tetrahedrons(tetrainteriorin(i,1),1), tetrahedrons(tetrainteriorin(i,1),2),
tetrahedrons(tetrainteriorin(i,1),3)];
     for j=1:4
        neif=tetrahedrons(neighbours(tetrainteriorin(i,1),j),:);
        Lia=ismember(cf,neif);
        if Lia==[1 1 1]
          k=j;
        end
        j=j+1;
     end

   elseif zci==zc02
     cf=[tetrahedrons(tetrainteriorin(i,1),1), tetrahedrons(tetrainteriorin(i,1),2),
tetrahedrons(tetrainteriorin(i,1),4)];
     for j=1:4
        neif=tetrahedrons(neighbours(tetrainteriorin(i,1),j),:);
        Lia=ismember(cf,neif);
        if Lia==[1 1 1]
          k=j;
        end
        j=j+1;
     end
   elseif zci==zc03
     cf=[tetrahedrons(tetrainteriorin(i,1),1), tetrahedrons(tetrainteriorin(i,1),3),
tetrahedrons(tetrainteriorin(i,1),4)];
      for j=1:4
        neif=tetrahedrons(neighbours(tetrainteriorin(i,1),j),:);
        Lia=ismember(cf,neif);
        if Lia==[1 1 1]
          k=j;
        end
        j=j+1;
      end
   else zci==zc04
     cf=[tetrahedrons(tetrainteriorin(i,1),2), tetrahedrons(tetrainteriorin(i,1),3),
```

```
tetrahedrons(tetrainteriorin(i,1),4)];
      for j=1:4
        neif=tetrahedrons(neighbours(tetrainteriorin(i,1,1),j),:);
        Lia=ismember(cf,neif);
        if Lia==[1 1 1]
          k=j;
        end
        j=j+1;
      end
   end

   [m,n] = find(tetrainterior == tetrainteriorin(i,1));
   A(51171,m)=-g(tetrainteriorin(i,1),k);
   A(51171,51171)=A(51171,51171)+g(tetrainteriorin(i,1),k);
   i=i+1;
end

b(51171,1)=2.5e-04;

%solve Ax=b using Over-Relaxation Method
w=1;
max_it=200;
tol=1e-10;
x=zeros(51171,1);
for i=1:1348
   [m,n] = find(tetrainterior == tetrainteriorin(i,1));
   x(m,1)=2.507;
   i=i+1;
end
x1=sor(A, x, b, w, max_it, tol)
```

3. Calculate the total pressure drps for two widest airflow paths through the cutted grain bed(interior tetrahedron units)

```
% import the data of two airflow paths tetrahedon units p1, p2 predicted from widest airflow path calculation

m1=1;
sum1=0;
sp1=size(p1,1);
for i=1:sp1
   for j=1:51170
      if x(j,1)==p1(i,1);
        sum1=sum1+x(j,2);
```

```
        tetrap1(m1,1)=p1(i,1);
        m1=m1+1;
      end
      j=j+1;
   end
 i=i+1;
end

m2=1;
sum2=0;
sp2=size(p1,1);
for i=1:sp2
   for j=1:51170
      if x(j,1)==p2(i,1);
        sum2=sum2+x(j,2);
        tetrap2(m2,1)=p2(i,1);
        m2=m2+1;
      end
      j=j+1;
   end
 i=i+1;
end
```